ISCIU10

- The 10th International Student Conference at Ibaraki University -

Diversity

November 15 - 16, 2014

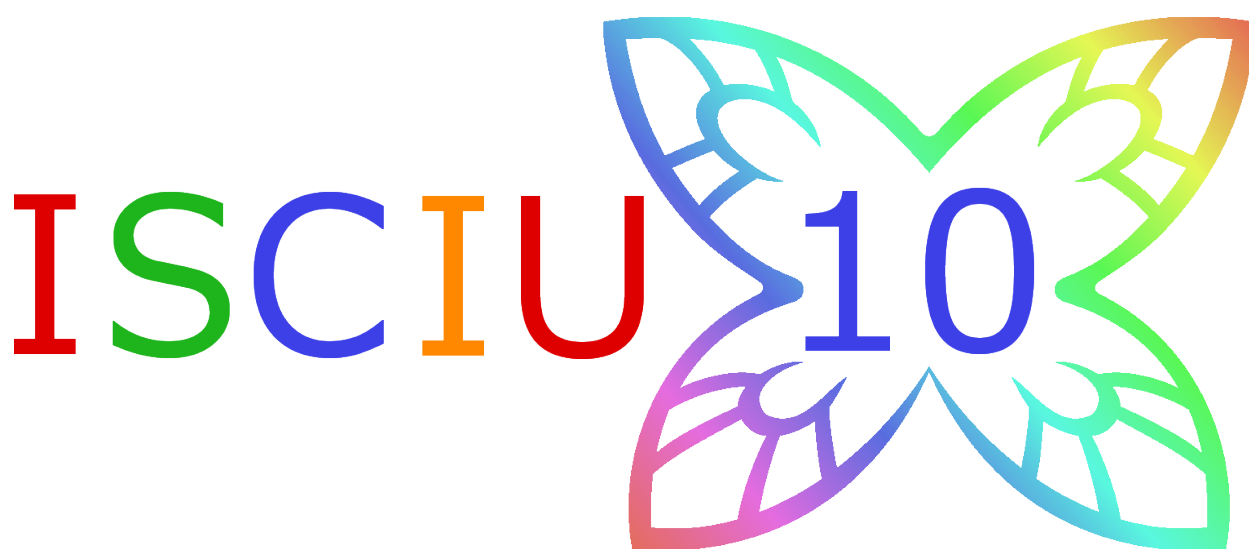Mito Campus

Ibaraki University

ISCIU 10

茨城大学
Ibaraki University

Proceedings of
The 10th International Student Conference at Ibaraki University
- ISCIU10 -

Organizer
Ibaraki University

Diversity

November 15th – 16th, 2014

Mito Campus, Ibaraki University

PREFACE

This Conference Proceeding volume contains 36 papers selected for presentation in the 10th International Students Conference at Ibaraki University (ISCIU10). The 10th edition of ISCIU took place in Mito, Ibaraki, Japan for November 15 - 16, 2014. The conference is organized under the auspices of graduates from Ibaraki University and in close supervision and support of professors committee.

ISCIU10 features oral and poster sessions on diverse range of topics within the field of Science and Engineering, Agriculture, Health, Culture and Society. The aim of this conference is to provide a platform where representatives from domestic and international universities can discuss and promote their research ideas.

We have decided the theme for this year's conference to be "Diversity". Various ideas, methods and different ways to approach problems have undoubtedly contributed to change and improve the quality of our social life. Diversity can give rise to curiosity which eventually brings prosperity and therefore science depends on it. If scientists were all the same, contrasting ideas and controversies in science would be rare, but so would be scientific progress. That's why it is important to promote diversity, not only to create a realistic way of thinking but also to encourage people to grow outside their boundaries and learn something new with which they may not be familiar. Thereby despite the diversity, all of the individual scientists are part of the same scientific community and provide valuable contribution to the scientific world.

In addition, regarding the concept of diversity, the unique property of this conference is that each session includes presentations from rather different fields of study and fruitful discussions for two consecutive days. We hope that every participant finds some new inspiration and gets acquainted to each other. Herewith, the organizing committee would like to express sincere gratitude to the authors who offered their latest research products and discoveries to contribute in ISCIU10.

We are looking forward to hosting the 11th International Student Conference at Ibaraki University (ISCIU11) with much vigor in autumn 2015 at Ibaraki University. We hope that it will be as productive and enjoyable as the ones organized in the past. Thank you for your continued support and cooperation.
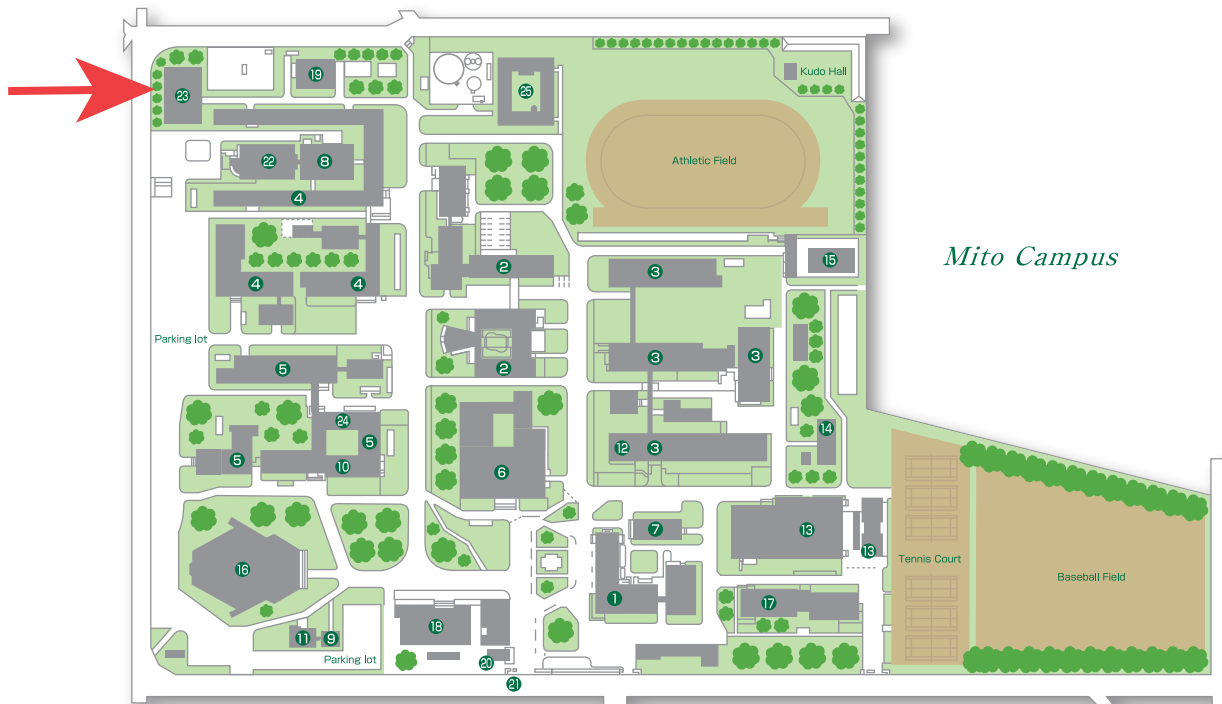
Anjeza ALAJ

Committee Chairperson ISCIU 10

Map

①"Ibadai-Mae"
②Affiliated Junior High School
③School for the blind
④Junior high school
　High school
⑤Gas station
⑥Ibaraki Prefectural Museum of History
⑦Art Tower Mito
⑧Kodokan
⑨Affiliated Elementary School
　Affiliated Kindergarten
⑩Kairakuen station
⑪Mito station
⑫Hitachiaoyagi station
⑬Mito station bus terminal

Mito Campus　2-1-1 Bunkyo, Mito, Ibaraki 310-8512, Japan
Take the Ibaraki-Kotsu bus bound for Ibadai (via Sakae-cho) from JR Mito Sta.
(North Gate) Bus Terminal 7, and get off at "Ibadai-Mae" (about 30 min.)

Mito Campus

①Administration Bureau（Admission Center）
②College of Humanities
③College of Education
④College of Science
⑤Common Education Building
⑥University Library
⑦University Health Center
⑧Center for Information Technology
　Building for the College of Scicnce
⑨Center for Education and Research in Lifelong Learning
⑩University Education Center
　International Student Center

⑪Institute of Integrated Regional Researches
⑫Center for General Educational Practice
⑬Gymnasium・Judo and Kendo Hall
⑭Overnight Accommodation for Athletes
⑮Swimming Pool
⑯Lecture Hall
⑰Shien Hall
⑱University Cafeteria and Store
⑲Center for Instrumental Analysis
⑳Security Gate
㉑Main Gate
㉒Integrated Research Building

㉓Environment Research Laboratory
　Institute for Global Change Adaptation Science
　The University of the Air Ibaraki study center
㉔Job Placement Support Center
㉕Facilities for Extra-Curricular Activities

The 10th International Student Conference at Ibaraki University -ISCIU10-

■ Theme
"Diversity"

■ Topics
- ◆ Agriculture
- ◆ Engineering and Science
- ◆ Health
- ◆ Culture and Society
- ◆ Other

■ Venue
Mito Campus of Ibaraki University (2-1-1, Bunkyo, Mito.)

■ Schedule

ISCIU10 1st Day (November 15th, 2014)

10:00 10:30	**Opening Ceremony**

Speaker of each poster will give a very short flush talk for 60 seconds without any visual aids in the opening ceremony.

10:30 11:30	**Poster Session**

Speakers give short talks on the posters of the A1 size followed by discussions with participants.

11:30 13:00	**Lunch Time**

	Oral Session A
13:00	**A01** **Stabilizing Sliding Mode Control Design and Application for a DC Motor : Speed Control** ○M. Meryl Rino
13:20	**A02** **RF Design of Wideband Fast Switching Device of High Power Millimeter Wave** ○Koji Nagashima, Keita Takii, Kenji Sekiguchi, Mikio Saigusa, Yasuhisa Oda and Keishi Sakamoto
13:40	**A03** **A Proposal of CAPTCHA Using Rotating Prismatic Objects** ○Yuki Kimura and Yasuhiro Ohtaki
14:00	**A04** **Compressive Strength of High Fluidity Concrete Using Fine Powder of Melt-Solidified Slag From Municipal Waste as an Admixture** ○Tohru Kimura, Tatsuya Numao and Kimio Fukuzawa
14:20 14:40	**Short Break**
	Oral Session B
14:40	**B01** **Ohmic Loss Estimation of a High Power Millimeter Wave Fast Switching Device by Numerical Calculation** ○K. Takii, T. Yamaguch, K. Nagashima, K. Sekiguchi, M. Saigusa, Y.Oda and K. Sakamoto
15:00	**B02** **Research and Development of a Portable Underwater Sensing System Using Electrolocation** ○Sayaka Endo, Kango Tsuyuki, Kyousuke Yamagata, Kenta Suzuki, Naoyuki Horie and Mikio Saigusa
15:20	**B03** **Interactive Animation Authoring Platform Based on State-Transition Diagrams that Runs on Android Devices** ○Erjing Zhou, Michitoshi Niibori, Shusuke Okamoto, Masaru Kamada and Tatsuhiro Yonekura
15:40	**B04** **Effects of Strain Rate on Tensile Properties of Tungsten at Elevated Temperature** ○Nobuatsu Tanou, Junya Kobayashi, Goroh Itoh, Akira Kurumada and Shingo Mukae

ISCIU10 2nd Day (November 16th, 2014)

	Oral Session C
9:00	**C01** **Research and Development of a High Power Millimeter Wave Wideband Polarizer** ○Fumiaki Matsubara, Keita Takii, Takuma Sai, Yoshitaka Ishida and Mikio Saigusa
9:20	**C02** **Practical Dynamic SSE with Forward Privacy** ○Hirotoki Sato and Yasuhiro Ohtaki
9:40	**C03** **Development of Virtual File Manager for Organizing Files** ○Yoshihiro Ito and Masaru Kamada
10:00	**C04** **Development of Cost Effective WSN System for Accurate Land Displacement Disaster Prevention** ○G.Anne Nisha and Atsushi Minato
10:20 10:40	**Short Break**
	Oral Session D
10:40	**D01** **The Relationship Between the Thrombogenicity and the Generated Flow around 3-Dimentional Micro Geometrical Structures on the Bio-material - Investigation of Micro Flow -** ○Akiko Ota-Ishigaki, Toru Masuzawa and Takayuki Shibata
11:00	**D02** **Turbidity Monitoring of Water Bodies Using Color Measurement System** ○S.H.P.K. Lakesh, D.D.G.L. Dahanayaka, Jiazhenzhen and Atsushi Minato
11:20	**D03** **Proposal of Android Application for Waiters to Enable Service Like Fancy Restaurant** ○Yuji Fujishima and Masaru Kamada
11:40	**D04** **Evaluation of Band-to-Band Position Gaps in ASTER Thermal Infrared Bands** ○Atsushi Kato and Hideyuki Tonooka

12:00 13:00	**Lunch Time**

	Oral Session E
13:00	**E01** **Diversity of the ABO Blood Group Genes in the Human Population** ○Masaya Itou and Takashi Kitano
13:20	**E02** **Social Consciousness Study Concerning Rational Use of Energy in the City Districts Based on the Research in the Area of Kashima City** ○Kazuki Tanabe and Toshiaki Kin
13:40	**E03** **Optimum Utilization of Fly Ash for Achieving Properties of High Performance Concrete** ○Anjeza Alaj and Tatsuya Numao
14:00	**E04** **Comparative Analysis of Different Atmospheric Sources Input to the ASTER/TIR Standard Atmospheric Correction** ○Takahiro Uehara and Hideyuki Tonooka
14:20 14:40	**Short Break**
	Oral Session F
14:40	**F01** **A Coloring System for Monochrome Images with Human Faces** ○Chisato Nagayama and Nobuyuki Umezu
15:00	**F02** **Cardio Vascular Circulation Simulator to Evaluate Ventricular Assist Effect** ○Wataru Kurosaki and Toru Masuzawa
15:20	**F03** **Extending Infinite Series Representation of Napier's Constant** ○ Kunimitsu Takahashi
15:40	**F04** **Determination of Distribution of Heavy Metals from Motor Vehicle Include a Complex Mixture of Metal from Tires, Brake Wear and Resuspended Road Dust** ○S.P.I.P. Kumara
16:00 16:30	**Closing Ceremony**

ISCIU10 1st Day (November 15th, 2014)

Poster Session Program

P01   **Mobile Radiation Monitoring with GPS Module**

○Nguyen Cao Thang, Nalin Warnajith and Atsushi Minato

P02   **Synthesis of Gd-DTPA Immobilized SiO2 Nanoparticles and Their Imaging Ability**

○Yuta Shindo and Yoshio Kobayashi

P03   **Fabrication of Alumina Thin Films Crystallized at Low Temperature**

○Katsumi Yamamura and Yoshio Kobayashi

P04   **Development of Techniques for Fabricating of Platinum-Immobilized Titania Particles by Electroless Plating Process**

○Masataka Sakai and Yoshio Kobayashi

P05   **Water Color Monitoring System Using Bluetooth**

○Jia Zhenzhen, S.H.P.K. Lakesh and Atsushi Minato

P06   **Investigation of the Diffusion Behavior of Hydrogen in a Ferritic Steel by Means of Hydrogen Microprint Technique**

○Sugawara Atsushi and Itoh Goroh

P07   **Inclination Measurement Using Camera and Bubble Tube**

○Gu Zhenghe, Anne Nisha and Atsushi Minato

P08   **Development of Efficient Algorithm for Ion-Mobility Spectrometry**

○Ryodai Suzuki and Masaru Kamada

P09   **Study on Grinding Characteristics of Grinding   Wheel Containing Conductive Rubber Balls**

○Shimon Hagiwara, Nobuhide Itoh, Takashi Matsuzawa, Hitoshi Ohmori, Teruko Kato, Hiroshi Kasuga, Takeshi Yoshimiya, Yuji Hasegawa and Naoki Maebayashi

P10   **A Refugee Prediction about University at the Catastrophes on the Basis of the Actual Refuge Situation on the East Japan Great Earthquake - A Case Study of the Ibaraki University -**

○Jing Ning and Toshiaki Kin

P11   **Visualization of Hydrogen in Electrolytically Charged Cold-rolled Austenitic Stainless Steels**

○Yukimasa Ichimura and Goroh Itoh

P12   **Development of ELID Grinding Wheel by PELID and 3D-printer**

○Daiki Yamamoto, Nobuhide Itoh, Nozomu Yamada, Hitoshi Ohmori, Teruko Kato and Shinjiro Umezu

A01

STABILIZING SLIDING MODE CONTROL DESIGN AND APPLICATION FOR A DC MOTOR: SPEED CONTROL

M.MERYL RINO

DEPT OF ELECTRONICS AND INSTRUMENTATION ENGINEERING.ST.JOSEPH'S COLLEGE OF ENGINEERING,CHENNAI

E-Mail: meryl_rino@yahoo.in
Keywords: Sliding mode control, Lyapunov stability, PID controller, DC motor.

ABSTRACT
The regulation by sliding mode control (SMC) is recognized for its qualities of robustness and dynamic response. This article will briefly talk about the regulation principles by sliding mode as well as the application of this approach to the adjustment of a speed control DC motor bench using the TY36A/EV unit. This unit, from Electronica Veneta products, uses a PID controller to control the speed and position of the DC motor. Our purpose is to improve the set time answer and the robustness of the system when disturbances take place. The experimental results show very good performances of the proposed approach relatively to the PID.

1. INTRODUCTION
The electrical servomechanisms for DC motors are nowadays, widely used in several robotic applications and electrical engineeringThis device is composed by two elements: the module G36A/EV and the mechanical process TY36A/EV. The training of experimental programs enables the development of exercises concerning the:
• Study of electrical servomechanisms for
 DC motors
• The speed and position control of a DC motor
• Study of DC motors

2. THE SYSTEM DESCRIPTION
The process TY36A/EV based on a DC Motor is controlled by the electronic device mod.G36A/EV from Electronica Veneta products (Figure 1). The main circuit blocks of the board mod.G36A/EV are:
• Set-point;
• Error Amplifier;
• PID controller;
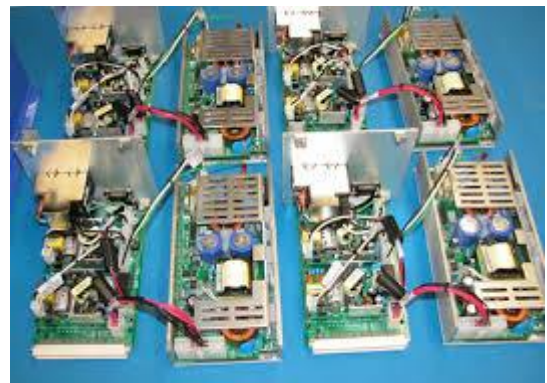• Signal conditioners for transducers.

Figure 1 The electromechanical process

3. PROCESS MODELLING
The system based on the DC motor is considered as a benchmark for the study and analysis of speed and position problems.This mechanical process TY36A/EV is composed of:
· DC permanent magnet motor;
· Optoelectronic transmission sensor;
·Transparent and opaque disk for fork optoelectronic transducer;

In this example, we consider that $k_1 = k_2 = k$.

$$\Omega(s) = \frac{k}{Rf + k.k + (RJ + LF)s + LJs.s}U(s) - \frac{R + Ls}{Rf + k.k + (RJ + LF)S + LJs.s}c_r(s)$$

In this work we consider that f and c_r are null, from where we conclude (5).

$$\begin{bmatrix} di/dt \\ dw/dt \end{bmatrix} = \begin{bmatrix} -R/L & K/L \\ K/J & 0 \end{bmatrix} \begin{bmatrix} i \\ w \end{bmatrix} + \begin{bmatrix} 1/L \\ 0 \end{bmatrix} u$$

$$W = \begin{bmatrix} 0 & 1 \end{bmatrix} \begin{bmatrix} i \\ w \end{bmatrix} + [0]u$$
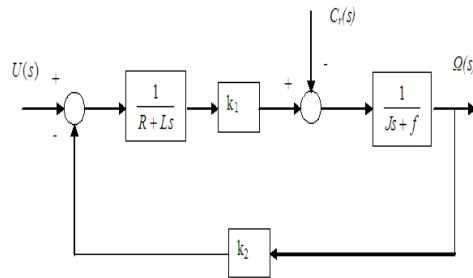
A01

Figure:Bloc diagram of a DC motor regulation

4. THE SLIDING MODE CONTROL

4.1 The sliding mode approach

In this kind of regulation (SMC), the system state defines the position control unit. The idea is to divide the state space by a sliding surface, which delimit two spaces corresponding in two possible states control unit. This principle of commutation law consists on the use of a discontinuous control having
as function the state maintain on the sliding surface and the disturbances rejection.

4.2 A sliding mode control synthesis

For this type of study, we consider the case of commutation on the control unit with addition of the equivalent control. Other ways, we present the electronic design of this sliding surface that may be implemented to control the process in the testing phase .
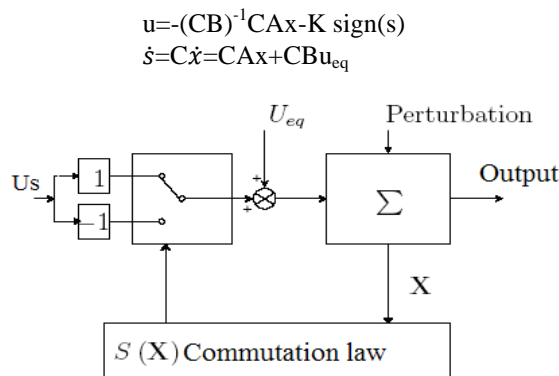
$$u=-(CB)^{-1}CAx-K \, sign(s)$$
$$\dot{s}=C\dot{x}=CAx+CBu_{eq}$$

Figure : Control unit with addition of the equivalent control

5. EXPERIMENTAL RESULTS

In the beginning, we start by fixing the set point (1V≈ 660 RPM).This controller allowed us to reach the desired DC motor speed but with late response. Also, the PID controller showed a non robustness to disturbances.The control level and commutation frequency are also lower. Other way, the perturbation that exists in the sliding surface is due to the abrupt injection of the friction force f. we

conclude that the sliding mode control is more robust and present more speed response that gives the desired evolution of the system output.
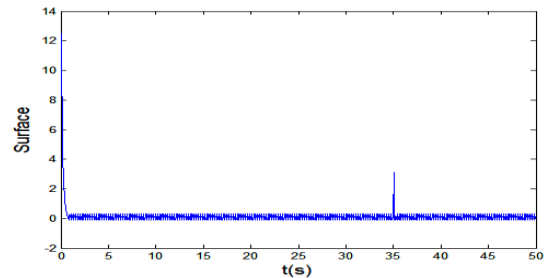
Figure : Sliding surface evolution

6. CONCLUSION

In this work, we approached the synthesis method of a stabilizing control law by sliding mode using a nonlinear sliding surface. We start by designing the sliding surface and representing the implementation of the electronic card that may be connected to the TY36A/EV unit. Then, multiple tests were done to control the process and to show differences between the old controller used, PID, and our new proposition that gives better results in lack and in the presence of disturbances. We conclude that the sliding mode control is more robust and gives quick reply to the system.

REFERENCES

[1] A.Sellami, R.Andoulsi, R.Mhiri, and M.Ksouri, "Sliding Mode Control Approch for MPPT of a Photovoltaic Generator Coupledto a DC Water Pump", JTEA, Sousse, 2002.
[2] B.Singh and V.Rajagopal, "Decoupled Solid State Controller for Asynchronous Generator in Pico-hydro Power Generation", IETE Journal of Research, pp. 139-15, Vol. 56, 2010.
[3] B.Singh and G.Kasal,"An improved electronic load controller for an isolated asynchronous enerator feeding 3-phase 4-wire loads", IETE Journal of Research, pp 244-254, Vol. 54, 2008.

A02

RF design of wideband fast switching device of high power millimeter wave

○Koji Nagashima*, Keita Takii*, Kenji Sekiguchi*, Mikio Saigusa*,
Yasuhisa Oda**, Keishi Sakamoto**
* College of Engineering, Ibaraki University, ** Japan Atomic Energy Agency
E-Mail: 13nm618n@hcs.ibaraki.ac.jp
Keywords: diplexer, NTM, ECCD, fast switching device

1. Introduction

Neo-classical tearing modes (NTMs) deteriorate energy confinement of fusion plasma in tokamaks [1]. Electron cyclotron current drive (ECCD) using high power millimeter wave could suppress NTMs [2]. It is useful that local current drive into O-point of a magnetic island of NTM for stabilization. Recently, for improving the stabilizing efficiency of NTM, the diplexer like a fast switching device has been developed [3]. It makes the duty of ECCD system to 100% by fast switching beam direction for tracking the rotating O-point of a magnetic island of NTM. For a frequency tunable ECCD system, the new wide band diplexer as a fast switching device was proposed [4,5]. The switching operation of a wideband diplexer was confirmed by numerical simulations, low power tests and high power tests. In this paper, simulation results of the high-frequency characteristics of the ring resonator and the T-shaped switching device are reported.

2. Principle of diplexer

The proposed diplexer consists of two cross circular corrugated waveguides, two miter bends and two half mirrors as shown in Fig. 1.

A propagation mode is the HE_{11} mode of which transmission loss is very low. Input power is divided into the reflected power to P2 and the transmitted power to ring resonator by a half mirror1. The transmitted electromagnetic wave is entered in a ring resonator. When the frequency of the electromagnetic waves is the resonance frequency of the ring resonator, rf power is accumulated in a ring resonator and the output power from P4 increases. On the other hand, when the frequency is not the resonance frequency of the ring resonator, the output power from P4 increase. So, output power can be switched by shifting a frequency.

The output powers from P2 and P4 can be shown in Eqs.(1) and (2), respectively [6], where "a" is power reflection coefficient of half mirror, L is resonant ring length, λ is wavelength of an incident wave, K is loss coefficient including mode conversion loss and Ohmic loss of single pass from port 1 to port 4, δ is loss coefficient including mode conversion loss and ohmic loss of the one turn pass in a ring resonator, and φ is phase shift of passing through a half mirror.

$$P_2 = \frac{a\left|1 + \{(1-a)\exp(i2\phi) - a\}\sqrt{\delta}\exp(i2\pi L/\lambda)\right|^2}{1 + a^2\delta - 2a\sqrt{\delta}\cos(2\pi L/\lambda)} \quad (1)$$

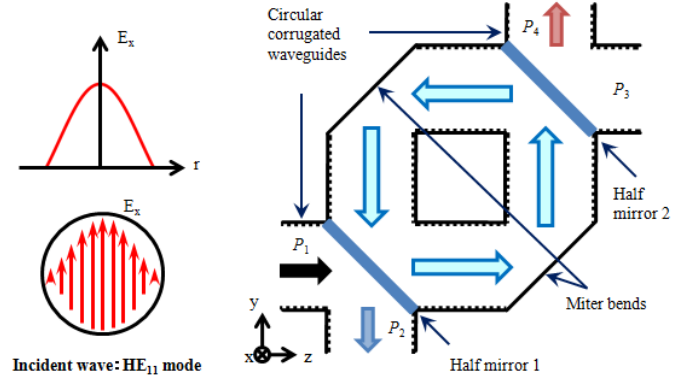$$P_4 = \frac{(1-a)^2 K}{1 + a^2\delta - 2a\sqrt{\delta}\cos(2\pi L/\lambda)} \quad (2)$$

Fig. 1. Principle of fast switching using a diplexer by shifting the frequency.

a=0.75, K=1, δ=0.9536, L=0.650 m

(a)

$$P_{4,max} = (1-a)^2 K / (1 - a\sqrt{\delta})^2$$
a: Power reflection coefficient of half mirror

$$P_{4,min} = (1-a)^2 K / (1 + a\sqrt{\delta})^2$$
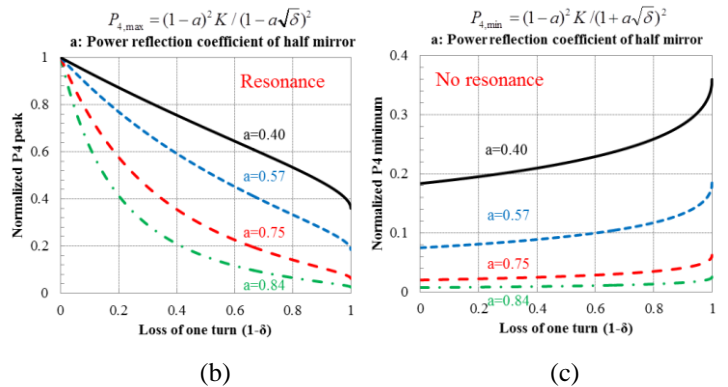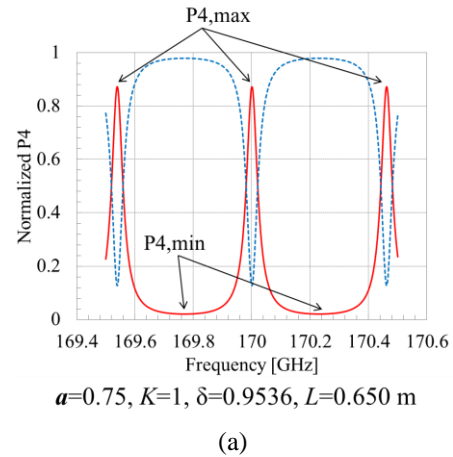a: Power reflection coefficient of half mirror

(b)   (c)

Fig.2. The output powers from the port 4 normalized by input power into the port 1. (a) Frequency dependence of P2 and P4 output powers, (b) dependence of P4 maximum output power on the loss of one turn, (c) dependence of P4 minimum output power on the loss of one turn.

A02

3. Numerical simulations

Constraints from the operation band gyrotron, it is necessary to increase the Q value of the resonance. Therefore, it is considered to increase the resonant ring length L.

The P4 can be written by Eq. (3) from Eq. (2), where K and δ are assumed to be one. Figure 3 shows the theoretical prediction with Eq. (3). The switching is sharp when the resonant ring length L is 1000 mm.

$$P_4 = \frac{(1-a)^2}{1+a^2 - 2a\cos t} \qquad (3)$$

$$t = 2\pi\delta f / \Delta f \qquad (4)$$

$$\Delta f = c / L \qquad (5)$$
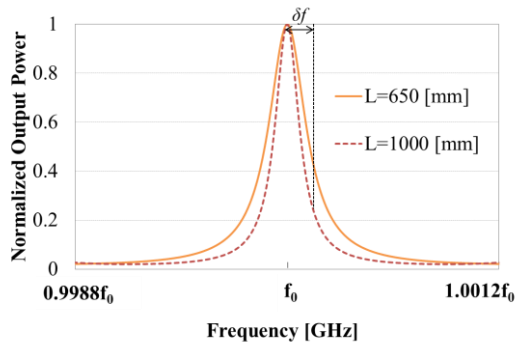
Fig. 3. Frequency dependence of the output power from P4 at the resonant ring length L of 1000 mm and 650 mm, respectively.
(Theoretical prediction with Eq. (3).)

The electromagnetic field in the fast switching device with diamond mirrors has been simulated using FDTD method.

The longer the resonant ring length L of the ring resonator is, the sharpener frequency dependence of the fast switching device output power is. This is useful to optimize the design of the diplexer due to the frequency modulation of the gyrotron.

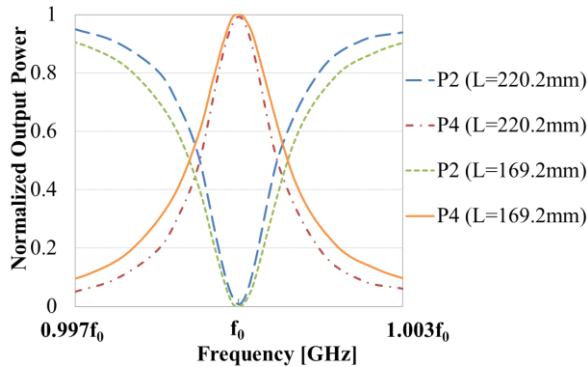Figure 4 shows the numerical simulation result.

Fig. 4. Frequency dependence of the output powers from P2 and P4 at the resonant ring length L of 220.2 mm and 169.2 mm, respectively.
(Numerical simulation with FDTD method)

4. T-shaped switching device

A simple the T-shaped switching device is proposed. Figure 5 shows a conceptual view of a T-shaped switching device. T-shaped switching device has a structure in which a corrugated waveguide T-shaped, put two mirrors spaced a gap of $\lambda / 2$ or less. By adjusting the gap length between the mirrors, the electromagnetic wave that is reflected by the first mirror, the electromagnetic wave is reflected by the second mirror is canceled and it is possible to switch the output of the P3 and P2. To confirm this principle, the electromagnetic field in the T-shaped switching device with sapphire mirrors has been simulated using FDTD method. It was confirmed that it can be switched, as shown in Fig. 6.
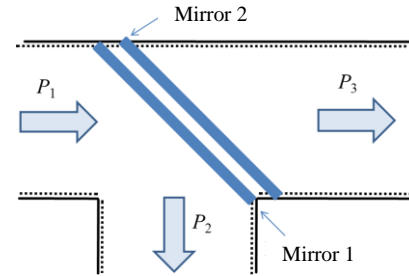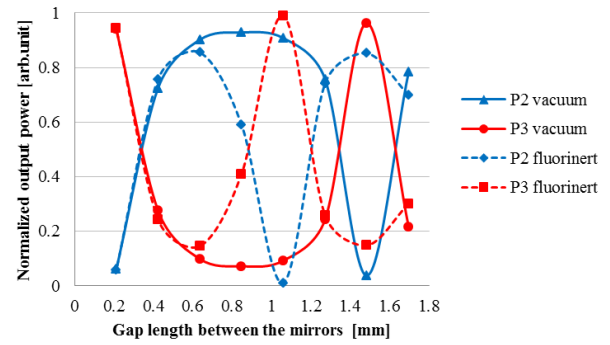

Fig. 5. Conceptual view of a T-shaped switching device

Fig. 6. Dependence of output powers from P2 and P3 ports on the gap length between the two mirrors.

5. Summary

To improve the confinement of fusion plasma in tokamaks, new fast switching device of millimeter wave is proposed and improved. From result of numerical simulation with FDTD method and theoretical prediction, the design of the resonant ring length L was examined. This paper proposes a T-shaped switching device on the new principle. It was performed to confirm the principle by Numerical simulation with FDTD method. In the future, the principles of T-shaped switching device will be confirmed by low-power test .

References
[1]. Z. Chang, et al., Phys. Rev. Letters 74 (1995) 4663.
[2]. H. Zohm, Phys. Plasmas 4 (1997) 3433.
[3]. W. Kasparek et al., Fusion Eng. Des. 84 (2009) 1002.
[4]. M. Saigusa, et al., Proc. of 13th AMPERE Toulouse (2011) 285.
[5]. M. Saigusa, et al., Fusion Eng. Des. 88 (2012) 964.
[6]. M. Saigusa, et al., Proc. of 20th Topical Conference 1580 (2013) 564.

A03

A Proposal of CAPTCHA using Rotating Prismatic Objects

○Yuki Kimura*, Yasuhiro Ohtaki**
Major in Computer and Information Sciences, Graduate School of Science and Engineering, Ibaraki University
**Center for Information Technology, Ibaraki University*
E-Mail: *y.kimura1226@gmail.com, **y.ohtaki@mx.ibaraki.ac.jp
Keywords: CAPTCHA, 3D Objects

1. Introduction

Today, we can find many web-based services with input forms. These web services are suffering from mass access using automated form submission programs. For example, attackers try to acquire many dummy mail addresses by submitting random names and passwords using such a program to a user registration form. Another attack is to mess up victim's blog site by submitting hundreds of SPAM messages.

To prevent these mass submissions by an automated program, CAPTCHA has been developed to distinguish between a human and a computer program. CAPTCHA is an acronym of "Completely Automated Public Turing test to tell Computers and Humans Apart". Typically, CAPTCHA adds a question and an input field to the input form. A good CAPTCHA should satisfy two requirements. One is the ability to generate a large number of questions with variation automatically. The second is that it must be hard to create a program that can solve the question.

A well-known classic CAPTCHA called 'Gimpy' shows an image of distorted words to a user. The user is supposed to type in the word in the answer field. Gimpy worked fine in 1997, because OCR technology in those days couldn't recognize distorted letters. However, recent OCRs have become smart enough to recognize these distorted letters. As a countermeasure, the distortion in the question image becomes stronger and more noises are added to the background. As a result, even human are not able to read the word.
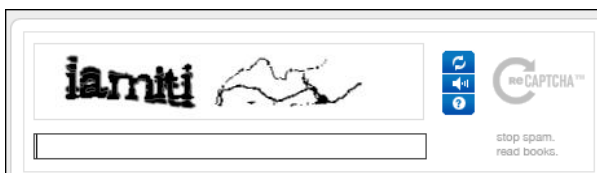

Fig. 1. CAPTCHA image by Gimpy

As a successor of Gimpy, many different kind of CAPTCHA have been proposed. "Pix" is to answer an object which appears in every image. "Bongo" is to find a characteristic that divides two groups of object images. "Sound" uses audio output as a question.

In late years, CAPTCHAs using rendered image of 3D objects have been studied [2,3]. These methods assume that it is easy for human to imagine the original 3D object from the rendered image, but is a difficult task for a program. These 3D object based CAPTCHAs have some weakness according to the answering style. In this paper, we propose a new CAPTCHA using rotating 3D prismatic objects, which can overcome the weakness.

2. Related Research

In this section, we describe some CAPTCHAs based on 3D objects.

Fujita *et al.* proposed a CAPTCHA based on "strangeness of merged objects" [2]. This method generates an image of many 3D objects. Every object is separately placed on a single plane, but only one object is placed on a same location with another object. This results as a weird "merged object". Such merged objects deviates from common sense of human, so human can easily recognize and tell which object is the merged one. This is a hard task for a computer. A user is supposed to answer the question by clicking the "merged object" in the image.
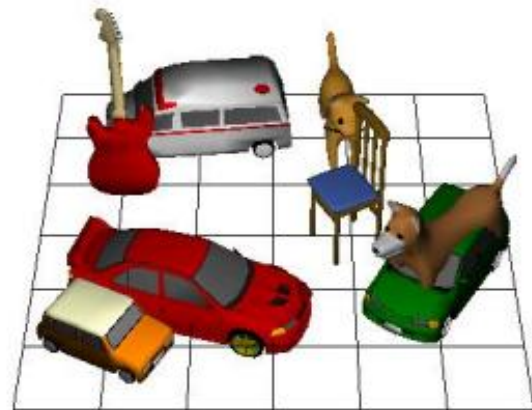

Fig. 2. CAPTCHA image using "merged objects"

Ikeya *et al.* proposed a CAPTCHA based on "mental rotation" [3]. Mental rotation is one of the human ability. When looking at two images of same 3D object from a different point of view, human can tell how to rotate the object from one image to obtain the other image. The CAPTCHA shows two image of an object from different direction. The object in the images may be the same, or different object that have a common structure (*e.g. a* horse and a cat). In one image, a marker is shown on the object (*e.g.* right ear). A user is supposed to click the same corresponding point on the object in the other image. A human can find the corresponding point easily by using "mental rotation". He/she can answer even if the corresponding point sneaks around to the back. But this is a hard task for a computer.
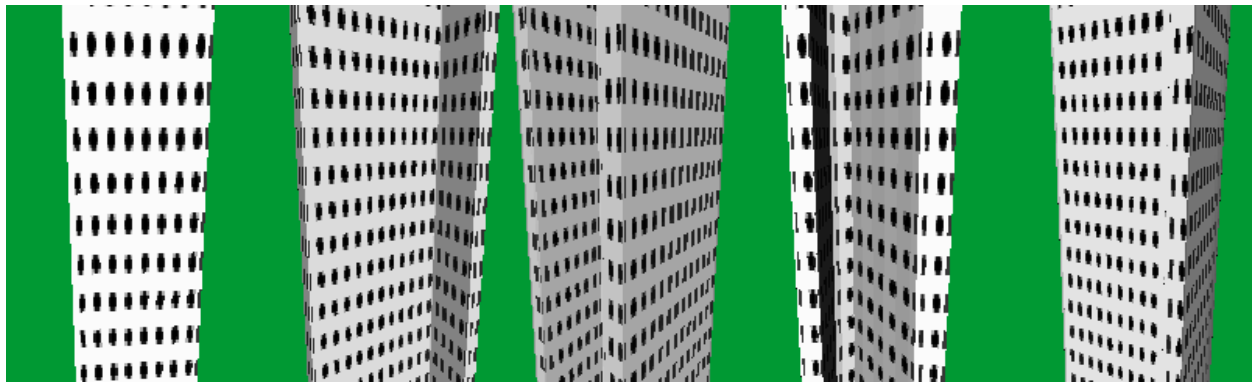

Fig.3. CAPTCHA image using "mental rotation"

Fig.5. A snapshot of CAPTCHA movie by the proposed method.

3. Security against random guess attack

In this section, we show that previous CAPTCHAs have a common weakness.

In both methods, a user answers the problem by clicking inside the image. By simply returning a random location, we can "break" these CAPTCHA with the probability of s/S. Here, s is the area of correct answer and S is the area of the whole image. Since the system has to allow some redundancy, the area treated as a correct answer becomes large. If the area of the correct answer is 10x10 pixels and that of whole image is 200x200 pixels, then the probability becomes 1/400. To the contrary, the probability to break Gimpy with 5 letters by random guess attack is $1/26^5$. Thus these 3D CAPTCHAs are terribly weak against random guess attack. To achieve the same security as Gimpy in these 3D CAPTCHAs, The size of whole image must be larger than 4000x3000 pixels.

4. Proposed method

In this section, we propose a new CAPCHA using 3D object. We designed the CAPTCHA to use the same answering method with Gimpy: the user answers a sequence of letters. The task is to answer the shape of cross section of a prismatic object, which should be recognized as a letter. If we can see the whole image of a prismatic object, it is easy to tell the shape of cross section from the view of ends. Thus we clipped the image with a viewport so that both ends are located outside of the image (Fig.4).
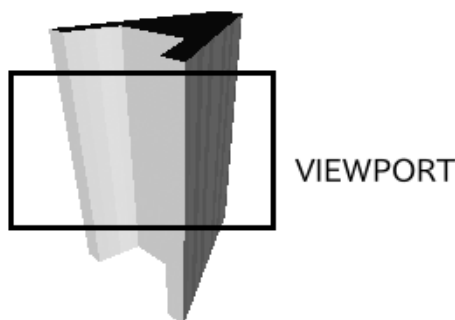

Fig. 4. Prismatic object of letter 'A' and the viewport.

Without both ends, the only information the user can use is the slant of side planes, which are recognized by the luminance. In order to emphasize the slant, a rough texture image is mapped on every side plane. To show all side planes, the prismatic object rotates slowly, i.e., the image is shown as a movie. The shapes of the rotating prism are chose from upper case alphabets. The letters "M", "N", "W" and "Z" are excluded, because it is hard to distinguish between "M" and "W", or "N" and "Z". We display five objects at random as shown in Fig.5. Movies of 5 letters are combined as a single movie file to prevent guessing each letter by the characteristic of each 5 separated movies.

The probability of guessing the correct answer by a random guessing attack becomes $1/22^5$, which is quite close to Gimpy.

To *solve* the problem with a computer, we have to reconstruct the original shape of each prism from the movie, using the illumination differences obtained from each frame. This is considered to be a hard problem in the field of computer vision [4].

5. Conclusion

In this paper, we proposed a new CAPTCHA method using 3D objects. The task is to answer the shape of cross section of 5 rotating prismatic objects. The cross section of each object is chosen from 22 capital letters. The method has enough security against random guess attack.

References

[1]L.von Ahn, Manuel Blum, John Langford, "Telling humans and computers apart (automatically)", CMU Tech Report CMUCS-02-117, 2002.

[2]Masahiro Fujita, Yuki Ikeya, Junya Kani, Masakatsu Nishigaki, "A Proposal of CAPTCHA using Strangeness in Merged Objects", Proc. of 31st Symposium on Cryptography and Information Security, 2014.

[3]Yuki Ikeya, Masahiro Fujita, Junya Kani, Yuta Yoneyama, Masakatsu Nishigaki, "An Image-based CAPTCHA Using Sophisticated Mental Rotation", HCI(24), pp.57-68, 2014.

[4]Carlos Hernandez, George Vogiatzis, Roberto Cipolla, "Multi-view Photometric Stereo", IEEE Transactions on Pattern Analysis and Machine Intelligence, Vol.30, Issue 3, pp.548-554, 2008.

A04

Compressive strength of high fluidity concrete using fine powder of melt-solidified slag from municipal waste as an admixture

○Tohru Kimura*, Tatsuya Numao**, Kimio Fukuzawa***
*ᐟ**ᐟ*** *Dept. of Urban and Civil Engineering, Ibaraki University*
E-Mail: *kimura@mx.ibaraki.ac.jp, **numao@ mx.ibaraki.ac.jp, *** fukuzawa@ss.iij4u.or.jp
Keywords: melt-solidified slag made from municipal waste, latent hydraulicity, high fluidity concrete

1. INTRODUCTION

In Japan, part of municipal waste is fused at a high temperature more than 1,200℃ to adapt the upper limit of dioxins in the residual material, in accordance with the "Law concerning special measures against dioxins" enforced on January 2000. Production volume of melt-solidified slag made from municipal waste is about 850,000,000kg every year. Some of the melt-solidified slag made from municipal waste is effectively utilized as the fine aggregate of concrete. The usage as fine aggregate has increased after registration of JIS A 5031 "Melt-solidified slag aggregate for concrete derived from municipal solid waste and sewage sludge" in 2006. The melt-solidified slag made from municipal waste has the latent hydraulicity because it is made through quenching process.[1] [2] The research on slag utilization as fine aggregate for concrete has been conducted by many researchers. [3]

Considering that a large amount of energy is used to produce the slag, a higher price material should be replaced by the slag.

This paper describes the compressive strength of high fluidity concrete containing fine powder of melt-solidified slag utilizing the latent hydraulicity as an admixture.

Table.1 Materials

Content	Density (g/cm³)	Fineness modulus	Specific surface area (cm²/g)
Ordinary portland cement	3.15	-----	3280
Type B portland blast-furnace slag cement	3.04	-----	3820
Fine aggregate	2.62	2.92	-----
Coarse aggregate	2.96	6.50	-----
High-range water-reducing admixture	1.04~1.08	-----	-----
Air-entraining admixture	1.04~1.08	-----	-----

Table.2 Manufacturing method and location of melt-solidified slag

	Melt-solidified method			Location	Density (g/cm³)	Specific surface area (cm²/g)
Manufacturing method	Melting furnace method	Middle classification	Classification			
A	Gasification melting furnace	Integration type	Shaft furnace type gasification melting furnace	a	2.81	4560
				b	2.81	4550
B	Ash melting furnace	Electric resistance type	Electric resistance type ash melting furnace	c	2.76	5780
C			Plasma type ash melting furnace	d	2.78	4590
C(4500)				e	2.79	4460
C(6000)				e	2.79	6070

Table.3 Mixture proportion of high fluidity concrete

Mix	Slump flow (mm)	Air (%)	W/C (%)	s/a (%)	Water (kg/m³)	Cement (kg/m³)	Melt-solidified slag (kg/m³)	Fine aggregate (kg/m³)	Coarse aggregate (kg/m³)	High-range water-reducing admixture (kg/m³)	Air-entraining admixture (kg/m³)
Base*			28.3	46.0	170	600**	---	755	888	3.4	0.009
A-a			27.8	45.9	167	300***	300	752	885	3.9	0.012
A-b			27.8	45.9	167	300***	300	752	885	3.6	0.009
B-c	680 ±50	4.5 ±1.0	30.0	46.0	180	300***	300	734	861	4.8	0.006
C-d			27.8	46.0	167	300***	300	752	882	3.6	0.009
C-e(4500)-40			28.3	46.0	170	360***	240	752	882	4.2	0.009
C-e(4500)-50			28.3	45.9	170	300***	300	747	879	4.2	0.009
Ce(6000)			28.3	45.9	170	300***	300	747	879	4.2	0.009

*"Base" means a high fluidity concrete used portland blast-furnace slag cement, **Type B portland blast-furnace slag cement, ***Ordinary portland Cement

A04

2. EXPERIMENTAL PROCEDURES

Table.1 shows the materials used in the experiments. Table.2 shows the melt-solidified slag made from municipal waste used in this study. Manufacturing method of the melt-solidified slag written in the table is based on JIS A 5031. Table.3 shows the mixture proportion of high fluidity concrete. The base mix is a high fluidity concrete using Type B portland blast-furnace slag cement at a content of $600kg/m^3$. Ordinary portland cement was used for mixes except the base mix. And total amount of portland cement and melt-solidified slag was $600kg/m^3$. The sign of mix expresses manufacturing method and location of the melt-solidified slag. All concrete was steam cured and its compressive strength was measured at the age of 1, 7, 14, 28 and 56 days.

3. RESULTS

3.1. Slump flow, air content and density in over-dry condition

Table.4 shows the results of slump flow, air content and density of high fluidity concrete used in this study. All High fluidity concrete showed good flowability. Mix C-e expanded after forming as shown in Figure.1. The expansion seems to be caused by the chemical reaction between the metallic aluminum in slag C-e and $Ca(OH)_2$ produced through hydration. [4]

3.2. Compressive strength of concrete

Figure.2 shows the relation between compressive strength and age. The compressive strength of mix A-a which is used a slag manufactured by shaft furnace type gasification melting furnace was nearly equal to that of base mix which was used portland blast-furnace slag cement. The compressive strength of concrete made from other slag was lower than that of mix A-a and base mix. The compressive strength of concrete used slag C-e was markedly low.

Figure.3 shows the relation between compressive strength and density at the age of 28 days. It is shown that the compressive strength of concrete increases with the increase of density.

4. CONCLUSIONS

1. High fluidity concrete used a kind of melt-solidified slag manufactured by the shaft furnace type gasification melting furnace can obtain the same strength as high fluidity concrete made from portland blast-furnace slag cement.

2. Compressive strength of high fluidity concrete used melt-solidified slag as admixture increases with the increase of density in over-dry condition.

References

[1]. Kimio Fukuzawa *et al.* (2007). " Strength of mortar and concrete using fine powder of molten slag made from municipal waste as a cementitious material" *Sustainable Construction Techno.,* pp. 333-337.(in Japanese)
[2]. Kazuyuki Torii *et al.*(2003). "Physical-chemical properties and alkali-silica reactivity of molten slags" *Proceedings of the Japan Concrete Institute Vol.25,No.1.,* pp. 623-628.(in Japanese)
[3]. Masafumi Kitatsuji *et al.*(2002)."Utilization of the gasification-Melting slag from municipal solid waste as fine aggregate for concrete" *Concrete research and technology Vol.13(2).,* pp.89-98, (in Japanese)
[4]. Masafumi Kitatsuji (2013). "Influence of expanding concrete by Free-CaO and metallic aluminum" *Environment Solution Technology.,* pp.35-42.(in Japanese)

Table.4 Slump flow, air content and density in over-dry condition

Type	Slump flow (mm)	Air ontent (%)	Density (g/cm^3)
base	725	3.5	2.42
A-a	725	4.2	2.46
A-b	635	3.9	2.32
B-c	735	5.0	2.38
C-d	630	4.2	2.41
C-e(4500)-40	660	4.5	2.28
C-e(4500)-50	650	4.5	2.27
C-e(6000)	660	4.0	2.30

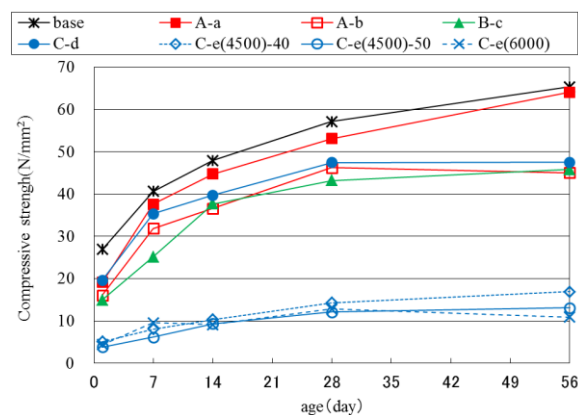**Figure.1 Concrete used C-2 after forming**

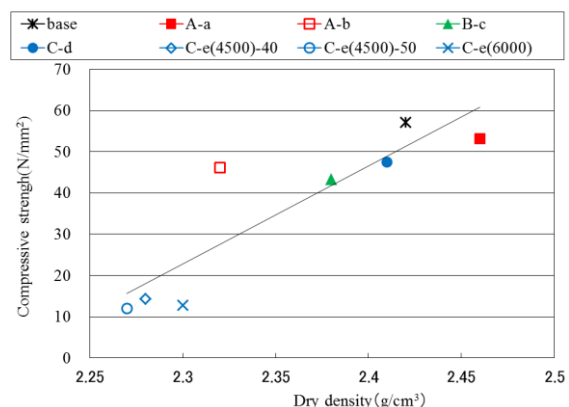**Figure.2 Relation between compressive strength and age**

Figure.3 Relation between compressive strength and density

B01

Ohmic loss estimation of a high power millimeter wave fast switching device by numerical calculation

○K. Takii*,T. Yamaguch*,K. Nagashima*,K. Sekiguchi*,M. Saigusa*,Y.Oda**,K. Sakamoto**
*Ibaraki Univ., **JAEA*
E-Mail: * 13nm616a@hcs.ibaraki.ac.jp

Keywords: fusion, tokamak, millimeter wave, Ohmic loss, FDTD method

1. Introduction

The Tokamak-type nuclear fusion reactor is one method that can solve an energy problem. However, there are many disabilities in realization. Above all, Neo-classical tearing modes (NTMs) are known as one of the problems. NTMs with rotate at 5-10 kHz deteriorate energy confinement of fusion plasma in tokamaks [1] as shown in Fig. 1. Electron cyclotron current drive (ECCD) using high power millimeter wave could suppress NTMs [2]. Local current drive into O-point of a magnetic island of NTM is useful for NTM stabilization. Especially, a fast directional switch makes the duty of ECCD system to 100% by switching beam direction for tracking the rotating O-point of a magnetic island of NTM [3]. For a frequency tunable ECCD system, the new wide band diplexer as a fast switching device was proposed [4]. The switching operation of a wideband diplexer was confirmed by numerical simulations and by low power tests [5, 6].

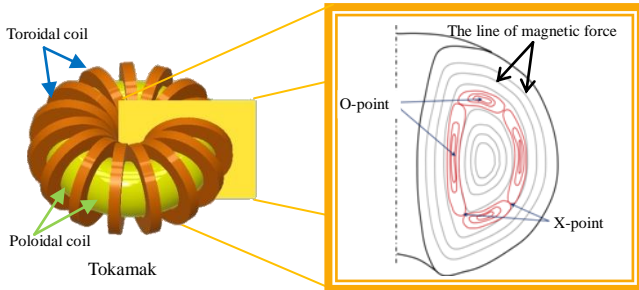In this paper, the results of numerical simulations of Ohmic loss of diplexer.

Fig. 1   O-points and X-points of NTM in the tokamak plasma

2. Current drive system

The ECCD system in tokamak is shown in Fig. 2. A Gaussian beam of high-power millimeter wave generated by a gyrotron is transformed to HE_{11} mode that is a transmission mode by MOU. This millimeter wave propagated in a circular corrugated wavegaide and it is switched by our fast switching device into each output.
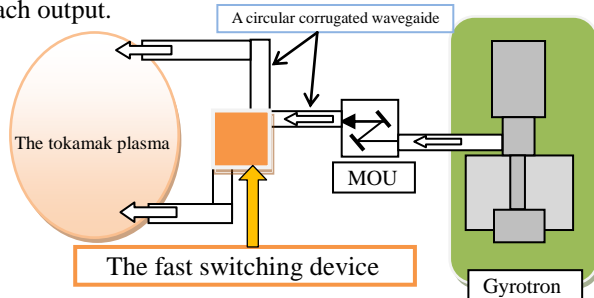

Fig. 2   Conceptual view of ECCD system

3. Principle of Diplexer

The proposed diplexer consists of a circular corrugated wavegaides, two miterbends and two half mirrors as shown in Fig. 3. These two pieces of half mirror is made of the Oxygen Free High Conductivity Copper (OFHC) with many slim slots. The incident wave is divided into the reflected wave and the transmitted wave by the half mirror 1. The transmitted millimeter wave is entered in a ring resonator. If it is a resonance frequency of a ring resonator, rf power are accumulated in a resonant ring and the output power from P_4 increases. On the other hand, in the case of no resonance, most power goes to P_2. So, the output power can be switched by shifting a frequency.
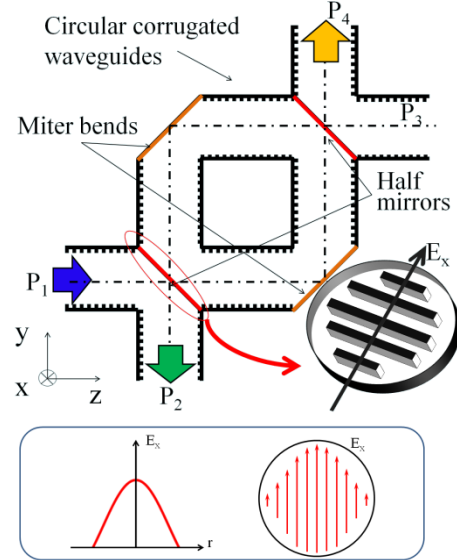

Fig. 3   Structure of the resonator and HE_{11} mode

The output powers from P_2 and P_4 can be shown in Eqs.(1) and (2), respectively [7], where "a" is power reflection coefficient of half mirror, L is resonant ring length, λ is wavelength of an incident wave, K is loss coefficient including mode conversion loss and Ohmic loss of single pass from port 1 to port 4, δ is loss coefficient including mode conversion loss and Ohmic loss of the one turn pass in a ring resonator, and φ is phase shift of passing through a half mirror.

$$P_2 = \frac{a\left|1+\{(1-a)\exp(i2\phi)-a\}\sqrt{\delta}\exp(i2\pi L/\lambda)\right|^2}{1+a^2\delta-2a\sqrt{\delta}\cos(2\pi L/\lambda)} \quad (1)$$

$$P_4 = \frac{(1-a)^2 K}{1+a^2\delta-2a\sqrt{\delta}\cos(2\pi L/\lambda)} \quad (2)$$

4. Numerical Simulations

4.1. A principle and parameter

The electromagnetic field in the diplexer has been simulated with our developed code using FDTD

B01

method as shown in Fig. 4. The FDTD method performs numerical analysis by building a part in Yee cell. The slotted metal plates are used as the half mirrors installed in the ring resonator. Long slotted metal half mirror made of OFHC is assumed in this simulation. The slot period is 1.5 mm (Air: Metal = 0.6 mm: 0.9 mm) as shown in Fig. 5, which is smaller than a wavelength: 1.76 mm at an input frequency of 170 GHz. The used cell size is smaller than one tenth of a wavelength of an incident wave. The circular corrugated wavegaides inner diameter is assumed to be φ21 mm which was 1/3 of full scale from a limit of the memory (18GB) of the computer. The main analysis parameters are shown in table 1.
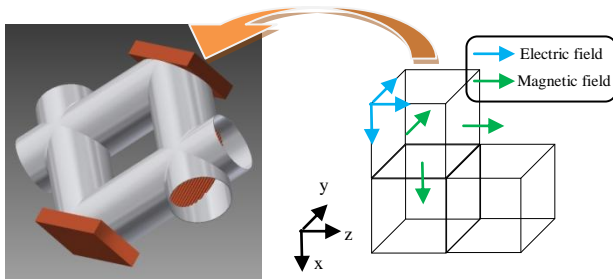
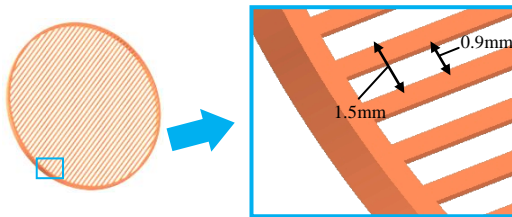

Fig. 4   Structure of the Yee cell

Fig. 5   Slot structure of the half mirror

Table 1   Main analysis parameters

Cell size [mm]	$0.15 \times 0.15 \times 0.15$
Number of the total cells	$182 \times 462 \times 462$
Time steps [s]	2.86×10^{-13}
Frequency [GHz]	170
Slot period [mm]	1.5
Slot thickness [mm]	1.69
Electrical conductivity of half mirror [S/m]	$\sigma = 5.76 \times 10^7$

4.2.   Result of simulation

The simulation results at the resonant frequency are shown in Fig. 6. This figure shows Pointing vector and relations of the time. The output from P_4 increases and the output from P_2 decreases. This result shows that the output is replaced by P_4 from P_2 output at the time of the non-resonance of the diplexer. When a diplexer performs resonance, the biggest Ohmic loss occurs to components. Ohmic loss is a thing by the metal minute resistance caused by the electric current which is generated by a high-power millimeter wave being the metal surface. Rs is a rf sheet resistance when an electric current flows through the metal surface by skin effect. H_t is a tangential magnetic field on the metal surfaces.

$$P = \frac{1}{2} R_s \cdot |\mathbf{H_t}|^2 [\mathrm{W/m^2}] \qquad (3)$$
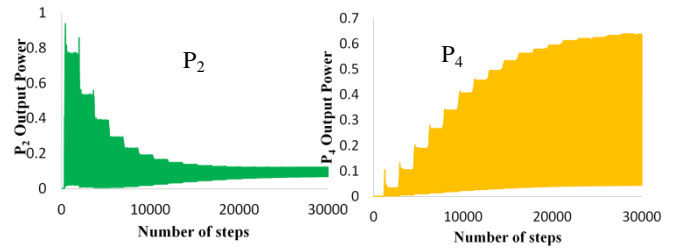

Fig. 6   Output of P_2 and P4 at the resonance

Ohmic loss profiles of the four mirrors are shown in Fig. 7. It is clear that all components have a large Ohmic loss of the center from these figures.
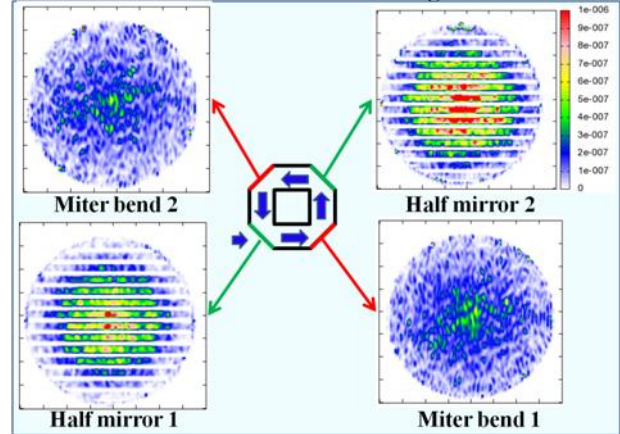

Fig. 7   Profiles on the mirrorsss Ohmic loss

Table 2 shows the Ohmic loss of each component normalized by input power in the case of resonance and the non-resonance, respectively.

Table 2   Ohmic loss of each component

	Half mirror 1		
	Incident side	Slot inside	Output side
Resonance	0.0868 %	0.571 %	0.32 %
Non-resonance	0.14 %	0.193 %	0.0164 %
	Half mirror 2		
	Incident side	Slot inside	Output side
Resonance	0.0778 %	0.698 %	0.495 %
Non-resonance	0.00271 %	0.0186 %	0.014 %
	Miterbend 1		Miterbend 2
Resonance	0.291 %		0.264 %
Non-resonance	0.0177 %		0.0161 %

Because the electricity is not accumulated to the resonator at the time of the non-resonance, the internal losses decrease. The loss of slot inside is particularly higher than other components at the time of the resonance.

5.   Summary

Ohmic loss of the metal half mirror of a high power millimeter wave fast switching device was evaluated. The Ohmic loss of all components is estimated to be about 2.8% of incident power at resonance conditions.

References

[1] Z. Chang et al. , Phys. Rev. Let. 74, 4663 (1995).
[2] H. Zohm, Phys. Plasmas 4, 3433(1997).
[3] W. Kasparek et al. , Fusion Eng. Des. 84, 1002 (2009).
[4] M. Saigusa et al. , Proc. of 13th AMPERE Toulouse (2011).
[5] K. Atsumi et al. , "Research and Development of High Power Wideband Diplexer for ECCD System" Plasma Conference 2011, Kanazawa, 23P099-P.
[6] M. Saigusa et al. , Plasma Fusion Res. 7, 2405099 (2012).
[7] M. Saigusa, et al., Proc. of 20th Topical Conference. 1580 (2013) 562.

B02

Research and development of a portable underwater sensing system using electrolocation

○Sayaka ENDO, Kango TSUYUKI, Kyousuke YAMAGATA, Kenta SUZUKI, Naoyuki HORIE, Mikio SAIGUSA
College Engineering Ibaraki University
E-Mail: 13nm604y@hcs.ibaraki.ac.jp
Keywords: underwater sensor, electrolocation, weakly electric fish

1. Introduction

Fish called weakly electric fish living in Africa and South America, has an electric organ in the body, it can be a discharge of a few milli-volt. They form a electric field around by this discharge, distortion occurs in the electric field when the biological object or different electrical characteristics and the surrounding water is present in an electric field. There are countless institutions sensitive to the body surface of the weak electric fish, by sensing the electric field distortion, it is possible to grasp the situation of the surroundings. This sensing method is called electrolocation, and it is considered to be the ability to wearing in order to survive in water turbid weakly electric fish is whiteout [1].

The principle of electrolocation is shown in Fig. 1. In this horizontal section through a simplified electric fish, the black bar indicates the location of the electric organ. This organ is discharged at a regular rate under the command of the pacemaker nucleus in the fish's hindbrain (not shown). Electroreceptors are found in pores of the body surface, and their density is highest in the rostral region. The interior of the body is of relatively low resistance, while the occupied by electroreceptors. Internal shunting of current is prevented by insulating tissue that wraps the electric organ and surrounds it tightly within the narrow tail filament. An object with an impedance different from that of the surrounding water will alter the pattern of transepidermal voltage, and this alteration represents the electric image of the object[2].

In this study, it is an aim to develop underwater sensing systems engineering applications electrolocation. A proposal of the sensor, a trial product, experiment, and production of the instrument are reported.
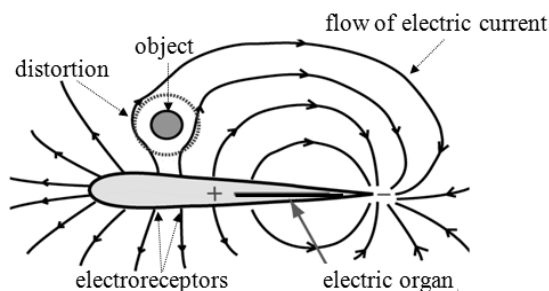

Fig. 1. The principle of electrolocation.

2. Experiments of electrolocation
2.1. Electrolocation sensor

A new sensor of electrolocation has been developed as shown in Fig. 2. Oscillating electrodes, which work like an electric organ of weakly electric fish, have a coaxial structure. Oscillating electrodes are fixed concentrically so that the electric field is distributed evenly. This oscillating electrode was made of copper.

Electrode rods for measuring electric field are located in a circle between two oscillating electrodes. The measuring electrode was made of silver. Each electrode is fixed by the jig acrylic.
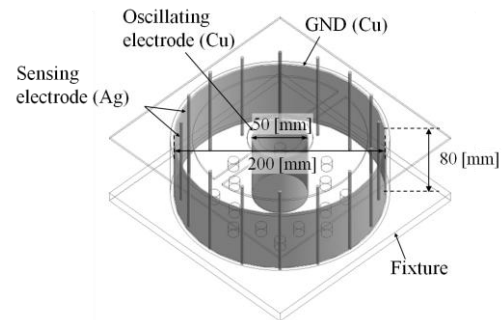

Fig. 2. Electrolocation sensor.

2.2. Experiments of electrolocation

Position detection experiment and characteristic detection experiment of the measurement object were done by a measuring apparatus utilizing the principle of electrolocation,

First, apparatus of position detection experiment is shown in Fig. 3. Electrolocation sensor is installed in the center of the tank containing the tap water. The signals are oscillated the center of the electrode which has a coaxial structure from the function generator, and an electric field is formed within the sensor. Put the measuring object in the electric field, and moves by 10 degrees counterclockwise while maintaining a fixed distance from the center electrode. A potential change of each channel by the position of the object is measured using oscilloscope and handmade lock-in amplifier by the differential. In addition, the 40 mm cube made of aluminum was used as the object to be measured.
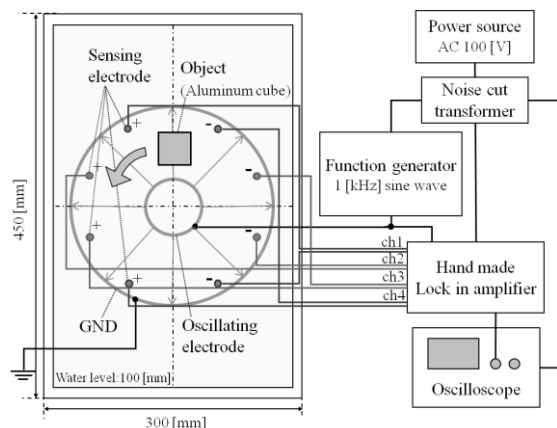

Fig. 3. Position detection experimental apparatus conceptual diagram..

B02

Next, experimental apparatus of characteristic detection experiment is shown in Fig. 4. Like the position detection experiment established the sensor in the center of the tank containing tap water, and an electric field is formed from the center of the cylindrical electrode. The measured object is moved by 10 degrees, the potential change is measured in the sensor. As the object to be measured, a total of six kinds of cube were used. (copper, aluminum, brass, iron, acrylic, synthetic rubber)
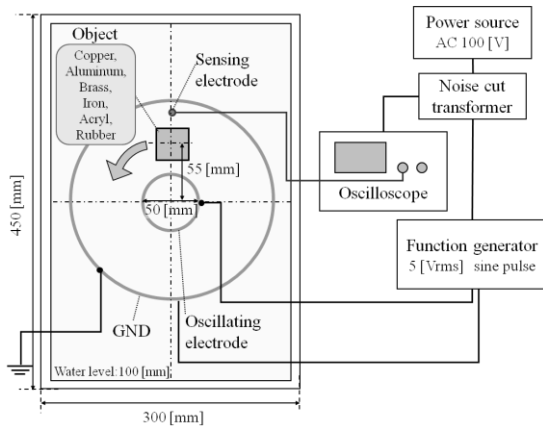

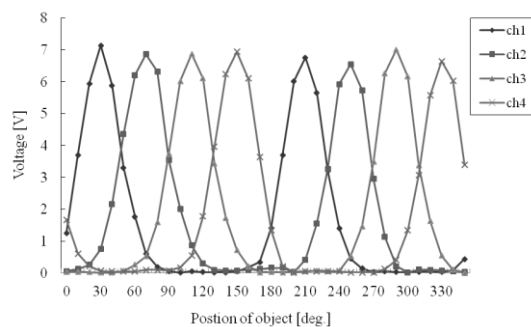**Fig. 4. Characteristic detection experiment conceptual diagram.**

2.3. Experimental results

Measurement results of position detection experiment and characteristic detection experiment were shown in Figs. 5(a) and 5(b),

From Fig. 5(a), it is shown that potential has a peak value when the object is closest to the electrodes in each channel. Also, there is a change in the potential from when an object came to a position away about 40 degrees from the electrode.

From Fig. 5(b), it is shown that potential is higher than the state there is no object in the conductor, the potential is low in the insulator.

In addition, in the measurement of this time, the potential change due to a difference in some of the electrical conductivity of the conductor to each other was not gotten.

(a) Measurement result of position detection
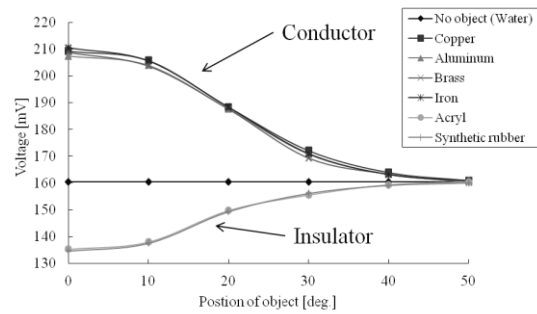
(b) measurement results of characteristic detection
Fig. 5. Measurement result.

3. Visualization of sensing results

In previous experiments, it has been detected the position and characteristics of the object by representing the measurement results the graph. However, the output in real time is needed practically. Therefore, the display is added to handmade lock-in amplifier. The display is ten levels LED meter. Moreover, the experimental results were transferred to the PC via the A/D converter board and then it will be displayed on monitor.
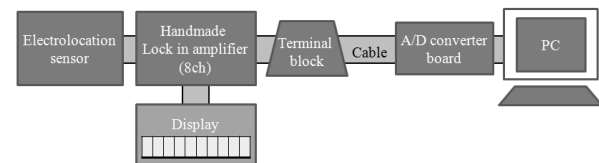

Fig. 6. Measurement system conceptual diagram.

4. Summary

The position detection experiment of the measurement object, it was found that the voltage difference is higher object approaches the electrode in any channel. However, differences were observed in the amount of change and the peak value of the voltage by the channel. The cause is the distortion of the electrode.

In characteristic detection experiments, it was able to distinguish between the conductors and insulators, but the distinction of the electrical conductivity between the conductors could not. This is because the electrical conductivity of the conductor is very high compared to that of tap water.

Future, to real-time visualization of the measurement results, as well as proceed with the construction of a system capable of object detection at the same time as the measurement, is working on improving the sensor based on the results of this time.

References

[1]. Kowatari Yoichi. "Technological Research about Sensing System of Weakly Electric Fish" *Master's thesis Iibaraki University*, pp. 1-3. (2010).

[2]. Walter F. Heiligenberg. "Neural Nets in Electric Fish" *A Bradford Book*. (1991).

B03

Interactive Animation Authoring Platform Based on
State-Transition Diagrams that Runs on Android Devices

○Erjing Zhou*, Michitoshi Niibori*, Shusuke Okamoto**, Masaru Kamada***, Tatsuhiro Yonekura***
*Graduate School of Science and Engineering, Ibaraki University,
**Faculty of Science and Technology, Seikei University,
***Department of Computer and Information Sciences, Ibaraki University
E-Mail: *zj13924@gmail.com, **okam@st.seikei.ac.jp, ***m.kamada@mx.ibaraki.ac.jp

Keywords: Android, interactive animation, state-transition diagram, Islay

1. Introduction

An interactive animation is a presentation of moving pictures that behave dynamically according to the input from users. It can be composed of animation characters modeled as finite-state machines. Based on this, an interactive animation authoring tool called Islay has been developed[1][2]. Islay allows users to create interactive animation simply by drawing state-transition diagrams on a GUI-based editor. Figure 1 shows the editor of Islay and the player which is used to play the animation created by Islay. Up to now Islay basically runs on PC, and we cannot use it on the portable devices that have become popular recently. Therefore, in this research, we developed a new version of Islay that takes advantage of the multi-touch features on Android[3] devices on the basis of the previous version.
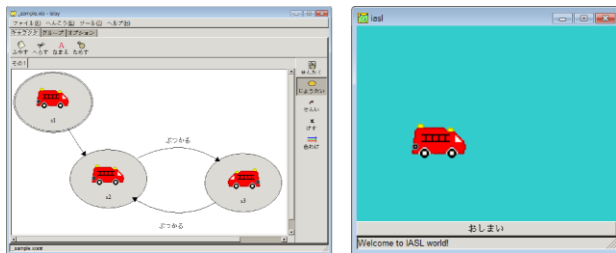

Fig. 1: Islay editor and Islay player

2. Islay for Android

The system is implemented as an Android application made up of an editor for creating animations and a player for executing animations. It extends the basic features of the previous version of Islay that runs on PC and is designed to support various types of touch gestures which can be performed on tablet devices.

3. Implementation
3.1. Editor

The editor runs on Android platforms where operations performed by using mouse are not available. Therefore, the operating method as well as the user interface had to be redesigned in order to make the editor as usable as the version that runs on PC or even more usable. Figure 2 shows the interface of the editor which is currently in the process of its development.

The selection of states which requires a left-click on mouse can be simply replaced by a single tap on screen. The property specification dialog which appears after a right-click in the PC version was replaced by the property specification bar on the bottom of the screen.

Compared with the mouse pointer used for selecting transitions in the PC version, touch gestures on the screen is hard to point accurately a small target like the arrows

representing transitions. On the other hand, Android accepts multi-touch gestures. So selection of a transition by mouse pointing was changed to selection of the two states being source and destination of the transition by a 2-point touch gesture.
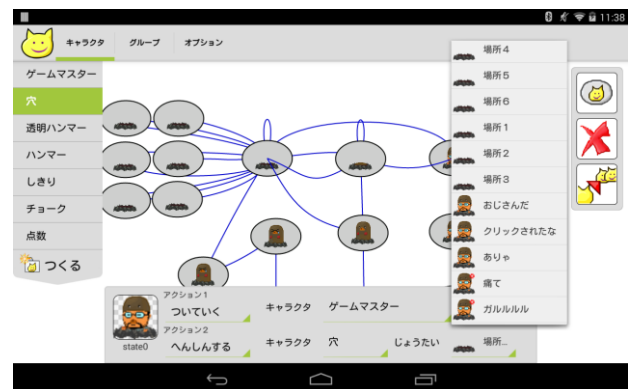

Fig. 2: User interface of Islay editor for Android

3.2. Player

The player reads the animation definition file created by the editor, and then interprets the content of that file. After extracting the components of the animation, the player starts to execute the animation. During the execution of the animation, the operations from the user are being obtained as external events, and the player checks the events whenever the transition happens. Figure 3 shows a sample of animation being played on an Android device.
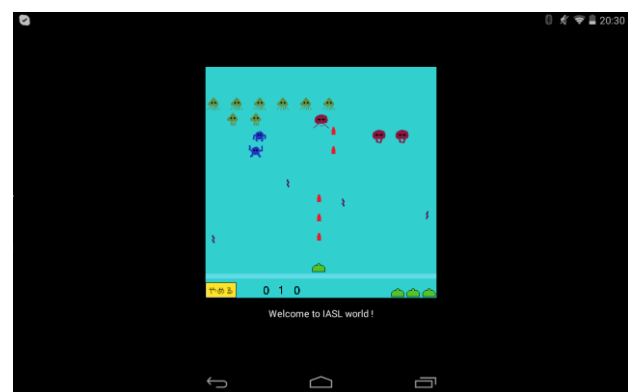
Fig. 3: Sample of animation played on Android device

3.2.1. Realization of the parser

In this research, the classes in Java platform[4] which deal with the processing of regular expressions are used for the interpreting of animation definition file. Matches between the file content and the previously composed patterns of regular expression are performed on two levels. The first level performs an overall match throughout the file, and additional matches which focus on each

B03

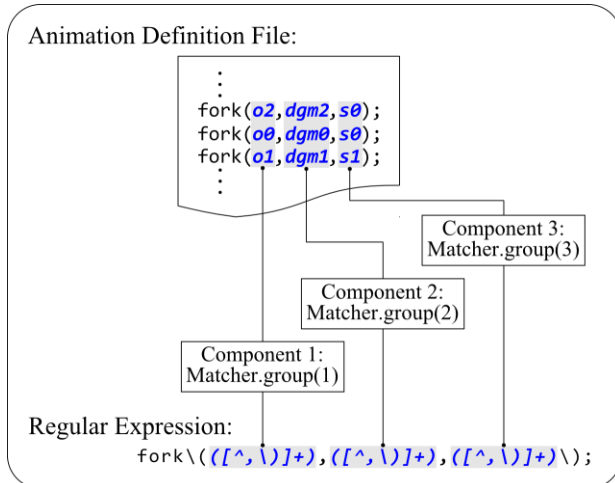component will be performed later on the second level.

Fig. 4: Sample of animation component extraction by using regular expression

The components of animation definition file which match the pattern of regular expressions are divided into different groups, and the *group* method of the *Matcher* instance is then called in order to extract the content of each group[5]. Figure 4 shows an example of animation component extraction on the second level by means of pattern matching. The animation components extracted by pattern matching are instantiated as the instances of the player class which will be mentioned later.

3.2.2. Details of the player

The player was designed on the basis of object-oriented model. Figure 5 shows the structure of each player class. The inclusions shown on the figure are to illustrate the relation that the instances of the classes inside can be referred to by the classes outside. Each class is instantiated separately and was independent from others.
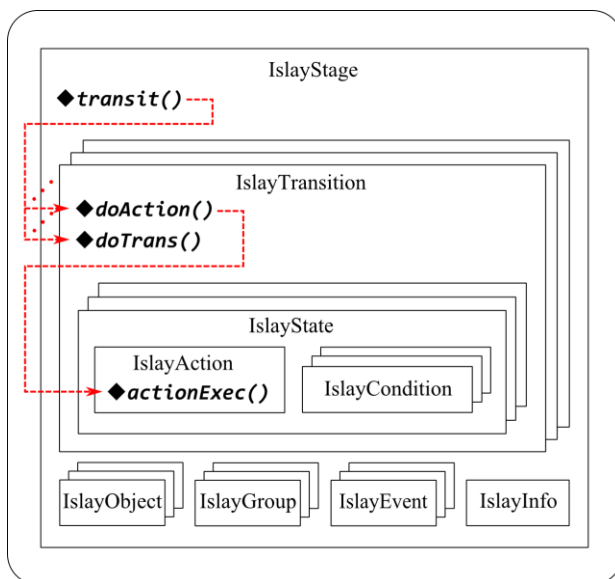

Fig. 5: Structure of player classes

IslayStage class is the foundation of the player. Instances of any other class can be referred to within it. The classes other than *IslayStage* correspond to the sections of the animation definition file. Instances of each class are created as their constructors are called by the

parser with the extracted animation components as parameters. The parser passes the name and content of images in the section of image data and image specifications to an instance of the *IslayObject* class that manages the images appears on the animation. A state-transition diagram in the section of states and transitions is passed to an instance of the *IslayTransition* class. Within the *IslayTransition* class, there are usually several instances of the *IslayState* class which further include instances of the *IslayAction* and *IslayCondition* classes. A group in the section of group specification is passed to an instance of the *IslayStage* class. The system parameters are set to the *IslayInfo* class. *HashMap* class of Java is used on the data fields of each player class when it is necessary to hold more than one instance of the same class.

The characters that appear on the animation are presented by instances of the *IslayTransition* class. During the main loop, the *transit* method in *IslayTransition* class is called periodically. The *transit* method then goes through all the character instances held in the data field of *IslayStage* class, and calls *doAction* method as well as *doTrans* method for each of them. Furthermore, the *actExec* method will be called by the *doAction* method, in which the current state will be updated after the check of transition conditions. By means of the procedure above, the implementation of a finite-state machine is realized.

4. Conclusion

In this research, an interactive animation authoring platform based on state-transition diagrams was designed for the portable Android devices. The user interface was adapted to be usable on the devices with smaller screens and with multi-touch operations.

References

[1]. Shusuke Okamoto, Masaru Kamada and Takashi Nakao, Proposal of an interactive animation authoring tool based on state transition diagram, IPSJ Trans. On programming, Vol.46, No.SIG1, pp.19-27, Jan. 2005.

[2]. Masayuki Nakagawa, Shusuke Okamoto, Masaru Kamada and Tatsuhiro Yonekura: Flash movie authoring environment based on state diagram, Proceedings of the Fifth Workshop on Network and System Support for Games 2006, (NetGames 2006), Singapore (Oct. 2006.)

[3]. Android, http://www.android.com/ (Accessed on Aug 29, 2014)

[4]. java.util.regex, http://docs.oracle.com/javase/7/docs/api/java/util/regex/package-summary.html (Accessed on Aug 29, 2014)

[5]. Matcher, http://docs.oracle.com/javase/7/docs/api/java/util/regex/Matcher.html (Accessed on Aug 29, 2014)

B04

Effects of strain rate on tensile properties of tungsten at elevated temperature

○Nobuatsu Tanou*, Junya Kobayashi**, Goroh Itoh***, Akira Kurumada****, Shingo Mukae*****
Graduate student, Graduate School of Science and Engineering, Ibaraki University, Japan,
,*,****Department of mechanical Engineering, Ibaraki University, Japan, *****Nippon Tungsten Co. , Ltd.,*
E-Mail: *14nm431x@vc.ibaraki.ac.jp,**jkoba@mx.ibarki.ac.jp, ***gitoh@mx.ibaraki.ac.jp,
****kurumada@mx.ibaraki.ac.jp, *****mukae@nittan.co.jp.
Keywords: tungsten, strain rate, elevated temperature, tensile properties.

1. Introduction

Tungsten has very higher melting point than other metal and a large electrical resistance. Therefore, tungsten is applied to the filament and the electrode for resistance welding. The electrode for resistance welding of tungsten are mainly used for fusing joining so that it has high heat resistance and be hard to alloy with work pieces. However, the cracks on electrode surface are occurred by welding any times.

Iijima et al. [1] reported about elevated temperature tensile properties of unrecrystallized and recrystallized tungsten. Results from tensile tests, the tensile stress of unrecrystallized tungsten reached a maximum stress at an early stage in stress–strain curve. The recrystallized tungsten had a lower yield stress than the unrecrystallized tungsten. At the testing temperature below 300°C, the recrystallized tungsten fractured before reaching the maximum stress. On the other hand, above 400°C, the test piece showed large local elongation. In this report, tensile test (strain rate 1.4×10^{-3} s^{-1}) was conducted at a temperature range between 200°C and 600°C in the two different microstructures (The unrecrystallized tungsten are hot rolling after sintering. The recrystallized tungsten are annealing at 1800°C after hot rolling.) of tungsten.

Although the high temperature characteristics of tungsten were investigated as a mentioned above, there is not the report about the effect of the strain rate on a tensile properties of tungsten at elevated temperature. In this study, to investigate the effect of strain rate on the high temperature deformation characteristics of tungsten, tensile tests were carried out with varying strain rate at high testing temperatures. Then, the relationship between the microstructure and the deformation as well as process of fracture was discussed.

2. Specimens and Experimental Procedures

2.1. Specimens

Tungsten powder was sintered and hot rolled, and formed plate of thickness 2mm. Part of this plate was recrystallized by annealing at 1800°C in a hydrogen atmosphere. Tensile test pieces were cut by wire electric discharge machine from the plate, as shown in Fig. 1. Two type microstructures are shown in Fig. 2.

2.2. Experimental Procedures

Tensile test was carried out at strain rate 1.4×10^{-2} s^{-1} and a temperature range (every 100°C) between 300°C and 600°C. The test piece fixes the shoulder region of both ends in a jig. In order to accurately measure testing temperature, thermocouples (K type) were used. The tensile testing equipment used all-around model tensile testing equipment (AG-G autograph, Shimadzu Co.). The

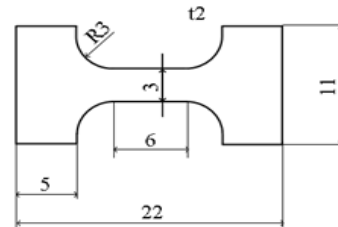high temperature tensile testing was started after holding 15 minutes after reaching a predetermined temperature.

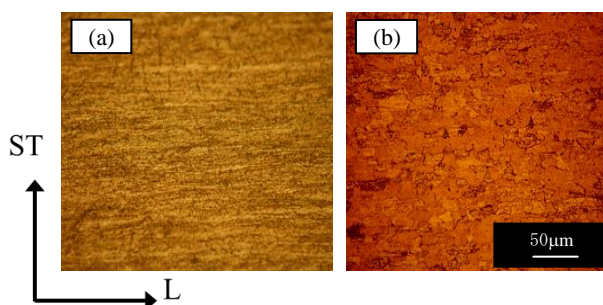Fig. 1 Dimension in mm and morphology of tensile test piece.

Fig. 2 Optical microstructures of the two specimens
(a) unrecrystallized, (b)recrystallized.

3. Results and Discussion

Stress–strain curves at each temperature of recrystallized and unrecrystallized tungsten are shown in Fig. 3 and Fig. 4. As shown in Fig. 3, the recrystallized tungsten fractured before reaching maximum stress at testing temperature 300°C. On the other hand, at the testing temperature above 400°C, the recrystallized tungsten had large elongation. In the unrecrystallized tungsten, a 0.2% proof stress was higher than that of recrystallized tungsten. In addition, it shows the maximum stress at a low strain in comparison with recrystallized tungsten. Unrecrystallized tungsten is a material obtained by rolling after sintering tungsten powder. Therefore, the microstructure had already been work-hardened by rolling. Thus, it is considered that the unrecrystallized tungsten was hardly work-hardened during tensile test. On the contrary, a large elongation of recrystallized tungsten is caused by the microstructure of recrystallized tungsten consisted of microstructure without strain by recrystallization.

The 0.2% proof stress, tensile strength and total elongation of recrystallized and unrecrystallized tungsten as a function of testing temperature are shown in Fig. 5 and Fig. 6, respectively. Fig. 7 shows the tensile strength and 0.2% proof stress of recrystallized tungsten, comparing with the data of Iijima et al [1]. As shown in Fig. 5, the recrystallized tungsten tested at 300°C had less than 10% of total elongation. On the other hand, at testing temperature above 400°C, the total elongation of recrystallized tungsten was over 60%. The tensile

B04

strength and 0.2% proof stress decreased with increasing testing temperature. The sharply increase of total elongation at testing temperature above 400°C was comported with a result of Bechtold [2] that a reduction of area in tungsten changed rapidly between 400°C from 300°C. In Fig. 6, the tensile strength and 0.2% proof stress of unrecrystallized tungsten decrease with increasing testing temperature, being similar to recrystallized tungsten. This can be explained from the fact that the deformation resistance of the metal decreases at the high temperature in general [3]. From Fig. 7, at the testing temperature above 400°C, the tensile strength of recrystallized tungsten in the present study was slightly higher than the data of Iijima et al [1]. This may be caused by higher deformation resistance due to high strain rate [4]. At high strain rate, the increase of deformation resistance in recrystallized tungsten may overcome softening by recovery during tensile test at elevated temperature.

4. Conclusion

Tungsten which had two kinds of different microstructure of recrystallized and unrecrystallized microstructure were examined at strain rate 1.4×10^{-2} s^{-1} and testing temperature between 300°C and 600°C, comparing with the report of Iijima et al. [1] that is result of strain rate 1.4×10^{-3} s^{-1}. Main results are followings.

1) The recrystallized tungsten fractured before reaching maximum stress at testing temperature of 300°C. On the other hand, at the testing temperature above 400°C, the recrystallized tungsten had large elongation. The 0.2% proof stress of unrecrystallized tungsten was higher than that of recrystallized tungsten.

2) The tensile strength of recrystallized tungsten at testing temperature above 400°C was slightly increased by increasing strain rate.

3) It is considered that the increase of tensile strength is caused by higher work-hardening due to increase in strain rate.

References

[1]. Iijima *et al.* (2014). " Tensile Properties of Tungsten at Elevated Temperature" *JSTP*, pp. 285-286.
[2]. F. H. Bechtold, (1955). " Tensile properties of annealed tantalum at low temperatures" *Acta Met*, pp. 249-254.
[3]. Ohga *et al*, (2004)." Kiso Sosei Kakoh Kogaku" *Morikita publisher*.
[4]. Yumoto *et al.* (1980). " Kihon Kikai Kousaku (I)" *The Nikkan kogyo shinbun*.
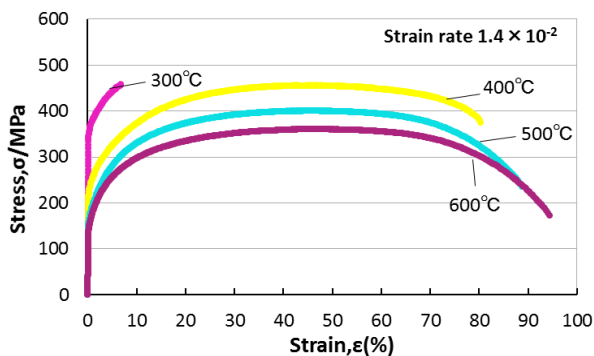
Fig. 3 Stress-strain curves of the specimens with recrystallized microstructure at various temperatures.
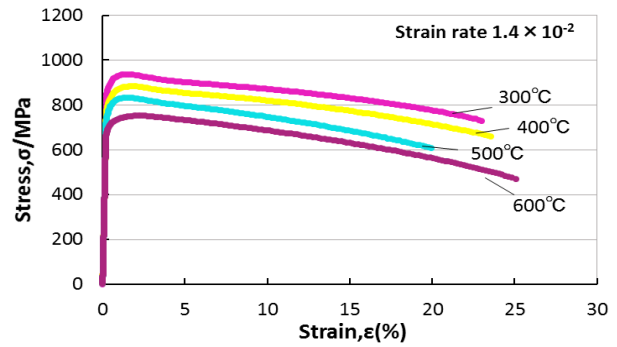
Fig. 4 Stress-strain curves of the specimens with unrecrystallized microstructure at various temperatures.

Fig. 5 Temperature dependence of the tensile properties of the specimens with recrystallized microstructure.

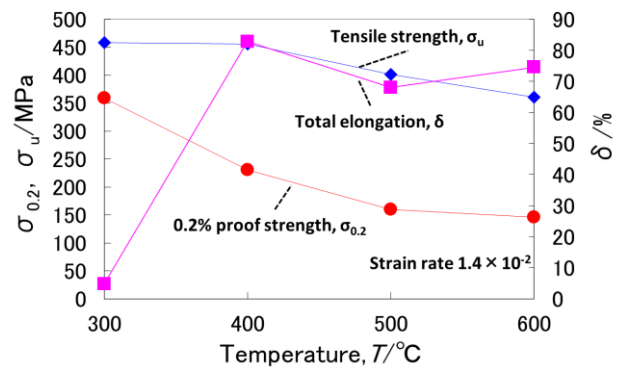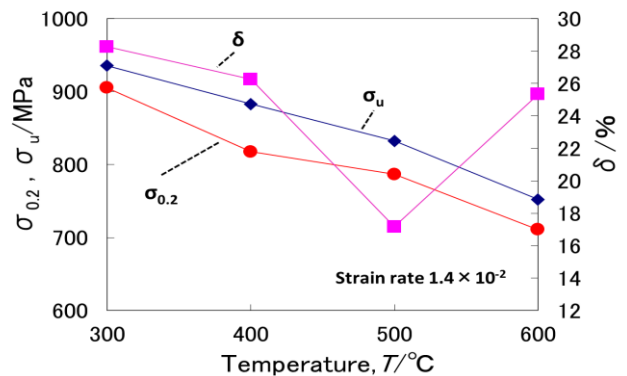Fig. 6 Temperature dependence of the tensile properties of the specimens with unrecrystallized microstructure.
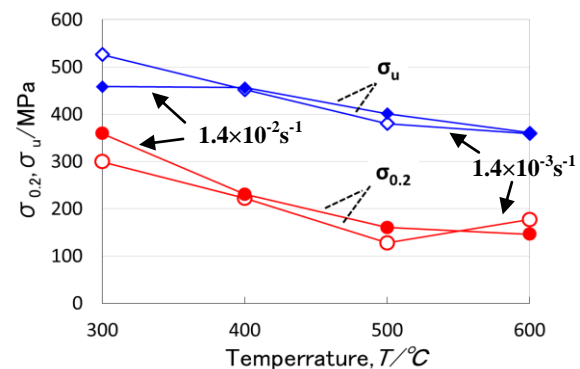

Fig. 7 Temperature dependence of the strengths of the specimens with recrystallized microstructure at two strain rates.

C01

Research and development of a high power millimeter wave wideband polarizer

○Fumiaki Matsubara*, Keita Takii*, Takuma Sai*, Yoshitaka Ishida, Mikio Saigusa*,
Takayuki Kobayashi**, Shinichi Moriyama**
*College Engineering, Ibaraki University, Hitachi, Ibaraki 316-8511, Japan,
**Japan Atomic Energy Agency, Naka, Ibaraki 311-0193, Japan
E-Mail: 13nm623n@hcs.ibaraki.ac.jp

1. Introduction

An Electron Cyclotron Current Drive (ECCD) is one of the additional heating and current drive methods of fusion plasma. High efficient operations for this method need the obliquely propagating electromagnetic wave with the specified elliptical polarization [1]. Polarizer is used to convert the elliptically polarization from linearly polarization. Up to now, the high power all metal polarizer has been used for narrow frequency band. In recent years, the dual-frequency gyrotron developed by JAEA would be possible to change the frequency (110 GHz / 138 GHz). If a wide band polarizer can be developed and installed in a transmission line, this system can be simplified.

In this paper, the development of a wide band polarizer with the development of dual-frequency gyrotron for JT-60SA, is reported (Fig.1.). Thermal stress analysis of the polarizer has been performed using the Finite Element Method. Determining the material of the polarizer from the analysis result, high power test was performed for evaluating Ohmic Loss.
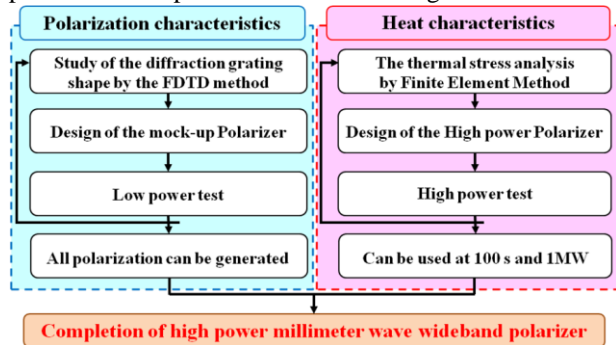

Fig.1. Research flow.

2. The principle of polarizer

The principle of polarizer is the application of the phase difference between a fast polarization and slow polarization in metal grooved mirrors. The high power all metal polarizer is composed of the two rotatable grooved mirrors installed in miter-bends in a transmission line (Fig.2.).
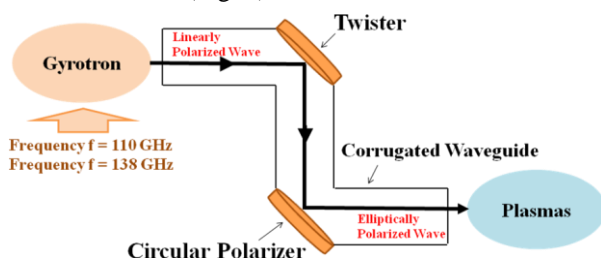

Fig. 2. Schematic view of Polarizer.

Linearly polarized Electromagnetic waves from gyrotron are converted by two rotatable grooved mirrors (Twister / Circular Polarizer) to specified elliptically polarized wave.

The linearly polarized wave, which is injected at a specified incident angle to a grooved mirror, can be divided into the two polarizations. One is the fast polarization: FP and the other is the slow polarization: SP, where the z component of magnetic field of FP and the z component of electric field of SP must be zero. The former is reflected on the top of the groove, the latter is reflected at a bottom of it as shown in Fig. 3.

In order to suppress high order diffraction waves, the period a must be given by

$$a < \frac{\lambda}{1 + \sin\psi\cos\phi} \qquad (2.1)$$

where ψ is a incident angle, φ is a rotation one in Fig. 3, and λ is a wavelength [2].
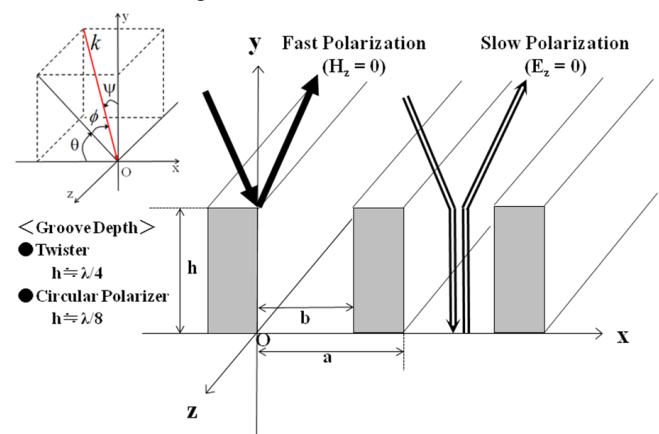
Fig. 3. Schematic view of grooved mirror.

A universal polarizer generally consists of a pair of grooved mirrors. The groove depth of the one mirror is about quarter wavelength, so that the phase difference between two reflected polarization waves is about π radians. The groove depth of the other one is about 1/8 of the wavelength, and the phase difference between two reflected polarization waves is about $\pi/2$ radians. Arbitrary elliptical polarized wave can be generated by rotating these two grooved mirrors.

3. Thermal stress analysis
3.1. Analysis model

To determine the material of the polarizer, the thermal stress analysis must be needed. Candidate of the material is Oxygen Free Copper, Chromium Copper (SH-1), and Oxide dispersion strengthened cupper (Glidcop, AL-15). Analysis model of which sizes are the same of actual polarizer is shown in Fig.4. Calorific values which are calculated by Eq. (2.2) are given to the grooved mirror surface. Furthermore, the constraints as shown in Fig.5 are assumed.

C01

Fig.4. Analysis model.

Fig. 5. Restraint condition.

$$\text{Ohmic Loss} = \frac{R_s}{Z_0} \times 4 \times 1.5 \times \frac{1.17 + 0.85 \times 2}{1.17} \qquad (2.2)$$
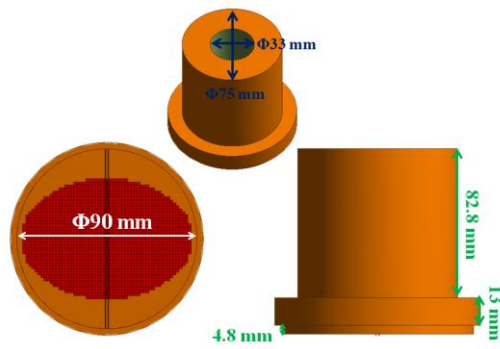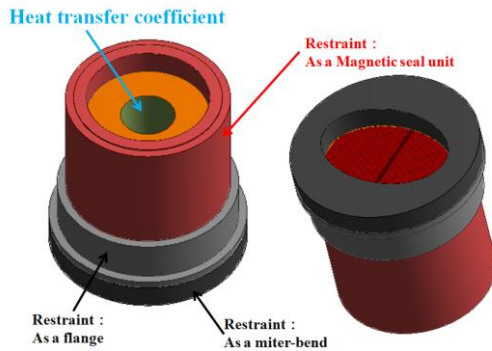
Where R_s is a Resistance and Z_0 is a characteristic impedance.

3.2. Analysis results

In determining the material of the polarizer, there are following two conditions :

①Stress does not exceed the yield stress

②Side temperature of polarizer is less than 80℃

The analysis results show the cooling (Flow rate) of the order to satisfy this condition (Table.1.). From the analysis result, the material of the polarizer was decided to Chromium-copper.

Table.1. Analysis results.

	①		②	
	h	Q	h	Q
Oxygen-Free-Copper	7,000	4.62	2,000	1.32
Chromium-Copper	5,000	3.30	3,000	1.98
Glidcop (AL-15)			2,000	1.32

Where h [W/m²/K] is a heat transfer coefficient and Q [L/min] is a flow rate.

4. High power test

4.1. High power test stand

High power test was performed in order to evaluate the Ohmic loss of the polarizer. Here, the twister which generates a large amount of heat is used. Electromagnetic wave from the gyrotron is propagated in the HE_{11} mode to the polarizer via MOU and the directional coupler as shown Fig.6. Then, it of RF wave is converted polarization by the polarizer, and the RF power is absorbed by the dummy load at the end.
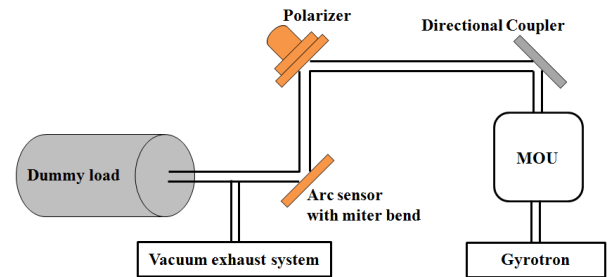

Fig. 6. High power test stand.

4.2. High power test results

Result of high power test is shown in Table 2. Ohmic Losses of the Polarizer agree with theoretical predictions. However, Ohmic Loss of Arc sensor with miter-bend was larger than the prediction. This is because the diffraction loss is included in the experimental results.

Table.2. High power test results.

	Polarizer			Miter bend		
A [deg.]	0	45	90	0	45	90
B [%]	0.45	0.63	1.1	0.23	0.28	0.23
	→			⤹	⤴	⤶
Theory		Iincrease		2 times		2 times
Test result		1.4 times	2.4 times	1.2 times		1.2 times

Where "A" is a rotation angle of the diffraction grating and "B" is a Ohmic loss.

4.3. Comparison of Analysis and Test

Comparison of Thermal analysis and High power test is shown in Fig.7. In theory, h=12,000 W/m/K is consistent with experimental result. Difference between theory and experiment is measurement error.
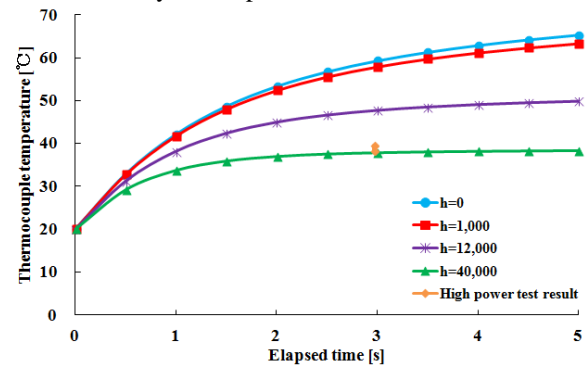
Fig. 7. Time evolution of polarizer temperature.

5. Summary

From the results of thermal stress analysis, the material of the polarizer was decided to chromium copper. High power test was performed in the twister. The dependence of Ohmic loss of polarizer in experiment agree with theoretical predictions.

References
[1]. M.I. Petelin, 1st International Workshop on ECRH transmission System, Florida, 1990.
[2]. N.Sugiyama, et al., (2011), "Research and Development of High Power Wide-band Polarizer for ECCD System" Plasma Conference 2011, Kanazawa, 23P098-P.

C02

Practical Dynamic SSE with Forward Privacy

○Hirotoki Sato*, Yasuhiro Ohtaki**

Major in Computer and Information Sciences, Graduate School of Science and Engineering, Ibaraki University,
**Center for Information Technology, Ibaraki University*
E-Mail: *13NM711Y@hcs.ibaraki.ac.jp, **y.ohtaki@mx.ibaraki.ac.jp
Keywords: Searchable Symmetric Encryption

1. Introduction

Cloud storage services have become very convenient in our lives. These storages have a possibility of being cracked by a third party. In order to prevent sensitive information from leaking, we may encrypt all of files before uploading to the storage server. However, a simple encryption will make it difficult to find and retrieve the files that you need. Searchable Symmetric Encryption (SSE) can prevent information leakage without losing the convenience of the cloud storage.

A basic SSE scheme consists of a store phase and a search phase. In the Store phase, the client builds an index that describes the correspondence between the files and keywords. The client stores the encrypted index when storing the encrypted files to the server. In the Search phase, the client sends an encrypted keyword to the server. The server can determine the files that contain the keyword without decrypting the encrypted keyword and the index. The server learns nothing about the keyword and the files.

Dynamic SSE is a SSE scheme that allows client to *add* or *update* files after the production of the encrypted index. SSE schemes that are not dynamic are called *static* SSE. In dynamic SSE scheme, we have to consider a property called "forward privacy". In this paper, we proposed a practical dynamic SSE that satisfies the requirements for forward security.
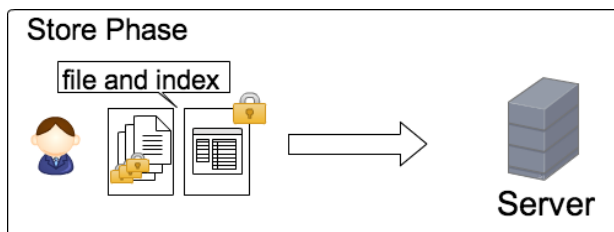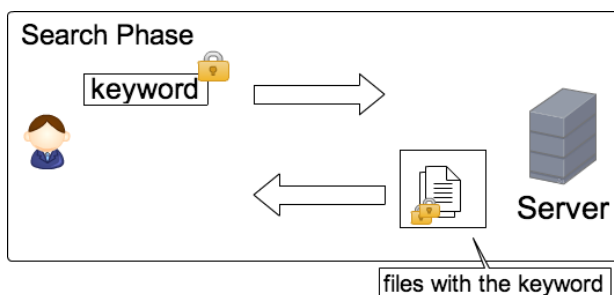

Fig. 1. Store Phase

Fig. 2: Search Phase

2. Related works

In 2006, Curtmola *et al.* proposed two static SSE schemes called SSE-1 and SSE-2 [1]. The encrypted index of SSE-1 is built as a linear list. SSE-1 is CKA1-secure. The index of SSE-2 is built as a look-up table. SSE-2 is CKA2-secure. Curtmola defined the classification of leakage information allowed in SSE, and formulated its security requirements.

In 2012, Kamara *et al.* proposed a *dynamic* SSE scheme [2]. In their approach the encrypted index is build by extending the linear list in SSE-1. The scheme is CKA2-secure. However, the structure of the index is too complicated and is hard to implement. It also has some drawbacks. When updating the index, partial information stored in the list structure are leaked to the server.

In 2013, Kamara *et al.* proposed another dynamic SSE scheme that supports parallelizing [3]. The index of this approach is built as red-black tree. This scheme is also CKA2-secure.

In 2013, Ogata *et al.* proposed a dynamic SSE scheme called SSE-1' [4]. They relaxed the security requirements of SSE-1 and proposed a lightweight version of it. First they show three requirements to be "practical", which are "efficient search", "reasonable index size" and "scalability". They also formulated additional security requirements to the one formulated in [1], which permits additional leakage from the practical point of view.

3. Forward Privacy in SSE

In a dynamic SSE, the following information are allowed to leak:

1. Encrypted keyword used for keyword search.
2. Document identifiers of documents that matched in a specific keyword search.
3. Document identifiers of added or deleted documents in the update phase.
4. Index size

Ideally, any other information must not leak through search or update operations.

Related to the second leakage information, there is an important issue called "Forward privacy". That is, if we search for a keyword w and later add a new document containing keyword w, the server does not learn that the new document contains the keyword w.

When "updating" the index in dynamic SSE, there are two approaches. One is to add information related to the new file inside the existing index and update the structural information. In this paper, we call this approach as "index update type". This update method does not satisfy forward privacy. Another approach is to generate and add a new index, which contains information according to the new file. So the whole index consists of many indexes of different generation. In this paper, we call this approach as "index-adding type". This approach satisfies forward privacy if we change the master encryption key to build each generation of index. However this approach has a drawback. We have to send many encrypted keywords in the search phase. That is, we have to send keywords to search through each generation of index. Thus the number of encrypted keyword sent to the server increase as we *update* the index. If the index has been updated 100 times, then the client have to send 100 search keyword tokens $t_1(w),...,t_{100}(w)$.

C02

4. Proposed scheme

In this section, we propose a new dynamic SSE by extending the construction of SSE-2. This is because SSE-1 is inferior to SSE-2 from the aspect of security; SSE-2 is CKA2-secure while SSE-1 is CKA1-secure. The basic structure of the index is a set of lookup table, which implementation is easy. Thus there is little leakage information to the server when "updating" the index. We can obtain the same security as other dynamic SSE shown in [3][4].

4.1. Structure of the Index

The basic structure of the index is shown in Fig.3. To achieve forward privacy, the index is designed as "index-adding type". Each generation of index consists of four tables: Tw, Ts, Tf and Td.
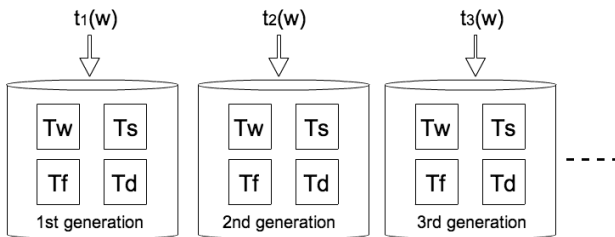

Fig. 3: Index of proposed scheme

Tables Tw and Ts are used in the search phase. The server first lookups Tw to find the number of file related to the search token $t(w)$. Let n_w denote this. Then the server generates n_w search data to lookup Ts and obtain a set of document ID.

Tables Tf and Td are used when deleting a file in the update phase. On file deletion, entries in Ts related to the file should be removed. Tf and Td are used to find the location of the entry in Ts without decrypting Ts. The server receives an encrypted file ID from the client and lookups Tf to find the number of keywords related to the file. Then the server generates search data to lookup Td. The server can know the address of entry in table Ts by looking up Td. To keep consistency, the number of files recorded in Tw should be also updated. This update is done when an inconsistency is found in the search phase performed latter.

4.2. Generation key management

As mentioned before, "index-adding type" SSE has a problem that the number of the encryption key increases according to each update. To solve this problem, we developed a generation key management scheme. Instead of maintaining encryption keys for each generation, we designed to calculate each generation key using public key encryption and a counter. For example, the search token $t_3(w)$ for the third index is calculated as follows:

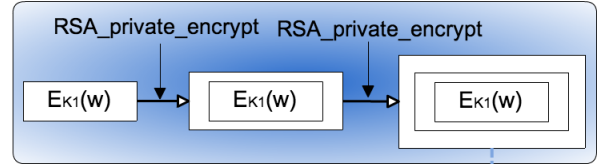$$t_3(w)=H(E_{K1}(E_{K1}(E_{K1}(w)))) \qquad (1)$$

Here, $K1$ is the private key of public encryption scheme and $H()$ is a cryptographic one-way hash function.

Assume that the third generation is the latest. In the search phase, the client calculates

$$s_3 = E_{K1}(E_{K1}(E_{K1}(w))) \qquad (2)$$

and send it to the server. The server can calculate the encrypted search keyword for every generation of index as follows:
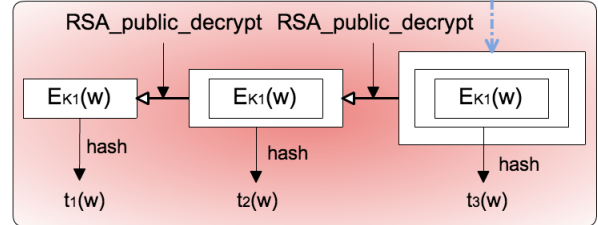
Fig. 4. Generation key management

$$\begin{aligned}
t_3(w) &= H(s_3)=H(E_{K1}(E_{K1}(E_{K1}(w)))) \\
t_2(w) &= H(D(s_3))=H(E_{K1}(E_{K1}(w))) \qquad (3) \\
t_1(w) &= H(D(D(s_3)))=H(E_{K1}(w))
\end{aligned}$$

Here, $D()$ denotes decryption using a public key.

Upon adding a new file, the forth generation index is created. Each entry in the tables of the forth index are encrypted by the scheme mentioned above.

Thus the client only has to send a fixed number of search keyword.

5. Conclusion

In this paper we proposed a new practical dynamic SSE scheme. The basic structure of the index is based on lookup table and is easy to implement. Our scheme is designed as index-adding type and thus satisfies forward privacy. In order to reduce the number of encrypted keywords sent in the search phase, we also developed a new generation key management scheme.

References

[1]. Reza Curtmola, Juan Garay, Seny Kamara, Rafail Ostrovsky, "Searchable symmetric encryption: improved definitions and efficient constructions", Proc. of CCS'06, pp. 79-88, 2006.

[2]. Seny Kamara, Charalampos Papamanthou, Tom Roeder, "Dynamic Searchable Symmetric Encryption", Proc. of CCS'12, pp. 965- 975, 2012.

[3]. Seny Kamara and Charalampos Papamanthou, "Parallel and Dynamic Searchable Symmetric Encryption", Proc. of the 2013 Financial Cryptography and Data Security, 2013.

[4]. Wakaha Ogata, Keita Koiwa, Akira Kanaoka, Shin'ichiro Matsuo, "Toward Practical Searchable Symmetric Encryption", Proc. of the Advances in Information and Computer Security, LNCS Vol. 8231, pp .151-167, 2013.

C03

Development of Virtual File Manager for Organizing Files

○Yoshihiro Ito*, Masaru Kamada*
Department of Computer and Information Science, Ibaraki University
E-Mail: 14nm701r@vc.ibaraki.ac.jp

Keywords: file manager, organize files, virtual

1. Introduction

This study aims at a file manager by which the user can organize files fast by virtual file operations for renaming, copying and moving. The user can organize files smoothly even when moving large files because the files will not be moved physically until the user presses the "commit" button. In addition, files can be organized like a file manager that we are familiar everyday use in appearance.

File operations on the virtual file manager is executed together after the file organization is over. The time is not applied to the file operation since it is summarized in the last time-consuming processing.

This software has been created as a Windows application by using the *Windows form* of *.Net framework*.

2. Related Works

2.1. XADisk

XADisk [1] is an open source software that Nitin Verma developed in Java. This is possible to access the file system by using the transaction to transfer multiple files at a time while keeping the ACID properties of the files. However, it does not offer a graphical user interface but a text-based interface.

2.2. Time-Machine Computing and Time Space

Time-machine computing is a computer desktop environment based on the concept of time-centric user interfaces by Junichi Rekimoto [2] that the accumulated history of user operations enables us to go visually back to the state of computer desktop at any time in the past. Apple computer's Time Machine can be regarded as a descendant of this time-machine computing. On the basis of this invention, a software product named TimeSpace has been developed. It offers the pseudo desktop such as shown in Fig. 1. TimeScape allows for file organizations along the time-space dimensions. It works as a backup tool as well as a quick search tool.

Fig. 1. The main screen of the Time Space.

3. System Overview

This section describes the overview of the system depicted in Fig. 2. This system is intended to offer a fast means of rearranging the files and folders in terms of graphical user operations (unlike the text-based interface of XADisk) but not to remember all the historical states of the file system (unlike the time-machine computing).

On boot, the system creates a virtual file system, i.e., a virtual copy of the real file system. If we would make a complete virtual copy of all the files on the computer at a time, the user would be kept waiting for a long time until he can start operating on the virtual file system. Instead, the system makes the virtual file system dynamically and incrementally, i.e., the real files and folders are made virtual only when they are touched by the user. This makes it possible to prevent the user from waiting for the virtual file system to be completed. Since the virtual files do not have their contents on the physical drives, all file operations on the virtual file system can be performed at a high speed.

Every time the user applies an operation on a virtual file or folder in the virtual file manager, the system pushes it into the operation history queue. After a series of virtual operations, the user presses the "commit" button to activate the real file operations. Each operation is taken out one by one from the operation history queue and applied to the real file system in the order they are pushed in the operation history queue. That is how the file operation on the virtual file system is consistently applied to the real file system.
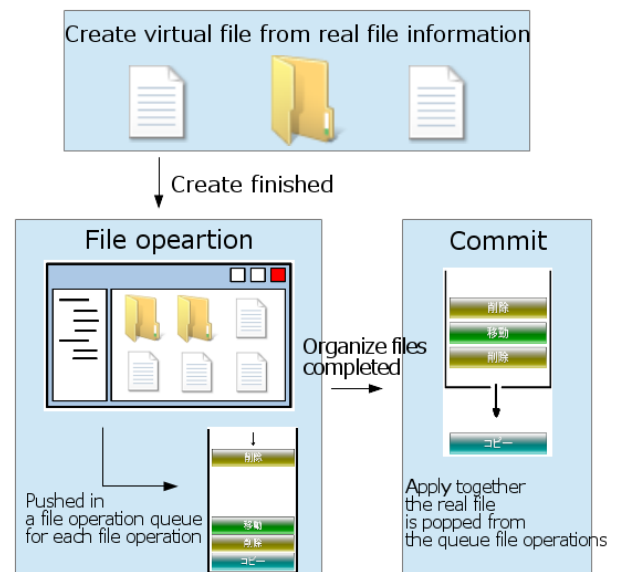

Fig. 2. Schematic diagram of a system of virtual file manager.

C03

4. Functions

This Section describes the functions of the virtual file manager.

The user see the main screen as displayed in Fig. 3 when the user starts the virtual file manager. The user operates files and folders on this virtual file manager. Real application of the operations to the real file system will be delayed until the user press the "commit" button.

4.1. Cut

This function is intended to move a virtual file or folder to another folder. After this operation, the user is supposed to select the folder to which the user plans to move the cut file.

4.2. Copy

This function is intended to copy a virtual file. After this operation, the user is supposed to select the folder to which the user plans to make a duplicate copy of the file.

4.3. Paste

This function is intended to paste the cut or copied file into a specified folder.

4.4. Remove

This function is intended to remove the specified file.

4.5. Rename

This function is intended to rename the specified file.

4.6. Create new Folders

This function is intended to create a new folder and give a name to it.

4.7. Undo

This function is used to retrieve the last operation.

4.8. Redo

This function is used to start over the operation just retrieved.

4.9. Commit

This function is executed by pressing the "commit" button. It is intended to apply all the virtual file operations to the real file system so that the structure of the real file system be the same as that of the virtual file system.

Fig. 3. Main screen of the virtual file manager.

5. Conclusion

We developed a virtual file manager that a file operation on the virtual file. It will improve the efficiency of file organization because the user can operate files smoothly without waiting for the real file system to finish he real file operation in the process of file organization.

References

[1] Nitin Verma. (2010). "Transaction with File System in Java |XADisk" <https://xadisk.java.net> (Accessed 11.08.14)
[2] Junichi Rekimoto. (1999). "Time-Machine Computing: Towards Time-centric User Interfaces", Workshop on Interactive System and Software '99 (WISS '99).
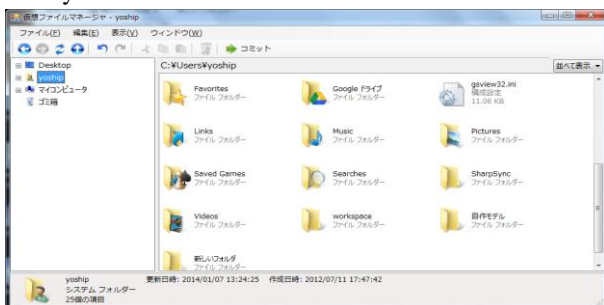
C04

Development of cost effective WSN system for accurate land displacement disaster prevention

G.Anne Nisha[1], Atsushi Minato[1]
[1]Department of Science and Engineering, Ibaraki University
(4-12-1, Nakarusawa, Hitachi, 316-8511, Japan)
E-Mail: [1]annenishag@gmail.com, [1]minato@mx.ibaraki.ac.jp
Keywords: bubble tube, landslide prevention, disaster measurement, WSN, Raspberry Pi

1. Abstract

Landslide is a major disaster causing natural catastrophes frequently. Monitoring the inclination of land is important to prevent and reduce the negative effects of landslide. While considering the large scale installation, the monitoring system should be stable and inexpensive. This paper deals with the development of a new low cost inclination measurement system and its application to a wireless sensor network for disaster prevention. The achieved resolution was 0.000153°/pix using bubble tube level with a radius of curvature of 20000mm. Measurement data was compared with the data from commercial inclinometer.

2. Introduction
2.1.1. Research background

Landslide hazard monitoring and analysis can provide useful information for the catastrophic loss reduction and assist in the development of guidelines for a sustainable land use planning

In the devastated area with a risk of landslide, monitoring the ground movement is necessary to predict the risk of landside. At present, there are several commercial equipments, which can detect changes of the land area. Even though these equipments can be used to obtain more accurate information, their cost is very high [1] [2]. So the development of inexpensive and reliable equipments has become a social requirement at present.

2.1.2. System description & Principle of measurement

This system has a USB web camera, a calibrated cylindrical bubble tube with 20000mm radius of curvature for greater precision and an XBee wireless module for real time monitoring. The bubble tube is continuously monitored by the USB camera, the angle and direction of inclination is measured by the change in bubble position. A GNL18/M model THORLABS goniometer was used to record the inclination (Fig. 1).
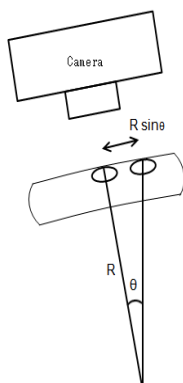

Fig. 1. Conceptual diagram of the measurement technique
Amount of shift in the bubble's center position ΔX can

be defined as $\Delta X = R\theta_x$ (1)

Where R: RoC, θ_x: device tilted angle in X direction.

If the change in the X-axis direction of the pixel value on the image Δix and assuming 'a' as the real space of one pixel, $\theta_x = (a/R) \Delta ix$ (2)

The same technique can be applied to the Y direction.

In this system, the image data of the bubble is captured by using a digital camera. Shooting instruction for the camera was performed using microcomputer or personal computer.

The proposed method is to calculate the angle and tilt direction of the apparatus from the position of the bubble center.

3. Evaluation experiment
3.1.1. Basic experiment

The vial is set on top of the goiniometer and adjusted in such a way that when the base is horizontal the bubble tries to remain at the highest point of the tube and moves along the scale. If the base is tilted to an angle in the range of +/-0.5°, the bubble will move to a distance. Inclination of the device changes to 0.000153° for the bubble of one pixel. The number of pixels was set to 640x480.

3.1.2. Continuous measurement

Continuous measurements at particular time interval are required to understand the characteristics of the bubble movement and land displacement. For this purpose, a sensor network system was developed based on the basic system description discussed in section 2.1.2. The basic configuration of the sensor network is shown in Fig.2.
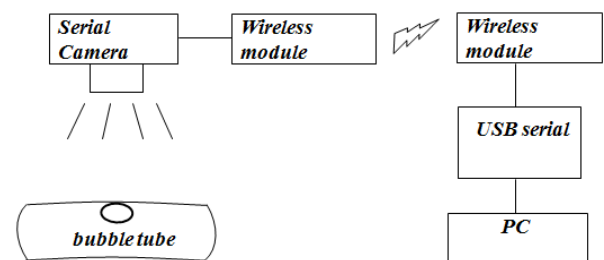
Fig. 2. Sensor network setup

For wireless module either Blue tooth or Xbee module can be used based on the distance between the locations of the sensors. Here, we used class 1 bluetooth module which has about 100m range of communication. For higher distances XBee communication module can be used (Which has a range of 1km communication).

The measurement was done simultaneously by using a Raspberry Pi computer for validation purpose. A 12V/5Ah battery with DC-DC converter is used to obtain the 5V power supply for the system. Linux based Python is used as a controlling program for

C04

Raspberry-Pi. Cron-tab technique is used to execute the program automatically when Raspberry Pi is turned on.

Basic configuration of the network is shown in Fig.3.
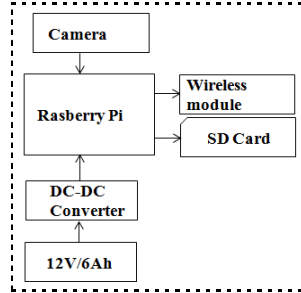
Fig. 3. Schematic diagram of Raspberry Pi network

3.1.3. Experiment results and validation

Sensitivity of the bubble tube is expressed as the angle of tilt for which the bubble will move in the bubble tube.

The sensitivity is directly related to the radius of curvature of the vial, longer the radius more sensitive the vial will be. Bubble tube with high radius of curvature is difficult to manufacture and it has some error due to flatness. It is necessary to calibrate the vial with goniometer to determine the sensitivity.

Bubble tube sensitivity θ is calculated by taking radius of curvature as 20000mm

θ = (pi/180)*20000 =349mm/deg.   (3)

The below graph shows the change in pixel value with respect to the angle of inclination (Fig. 4).

Fig. 4. Sensitivity graph (deg Vs pixel)

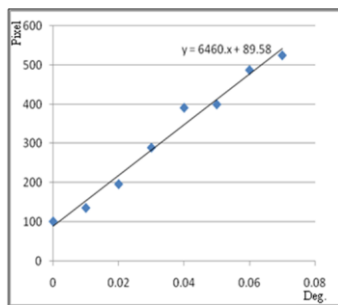From the figure it is shown that Y = mx+c; where m is the slope. Hence sensitivity is calculated as 6460°/pix. m=6460.

The below figure shows the change in the bubble position from the center in mm with respect to the angle of inclination (Fig. 5).
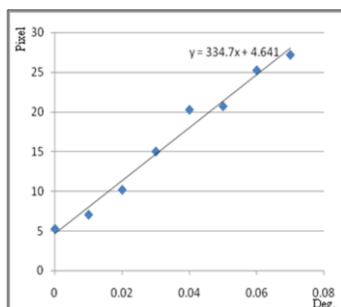

Fig. 5. Sensitivity graph (deg Vs mm)

The real time sensitivity of the bubble tube is 334mm/° which is closer to the bubble tube sensitivity.

Geometric distortion has to be considered for the image data. Two common types of distortion are barrel distortion and pincushion distortion. Distortion is tested with a graph sheet plotted with plots and the image data captured. The result was checked for how it appears on the optics, when conducted result shows error of 1-2%. Left part of the image is distorted comparing to the right part of the image (Fig. 6).
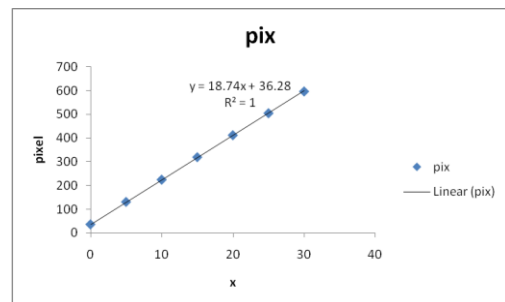
Fig. 6. Distortion graph obtained from the camera image

Continuous measurement of data with 10minutes time interval was taken automatically with interval shot web camera and the change in bubble tube was noted. Below figure shows the results obtained from continuous measurement of the bubble (Fig. 7).
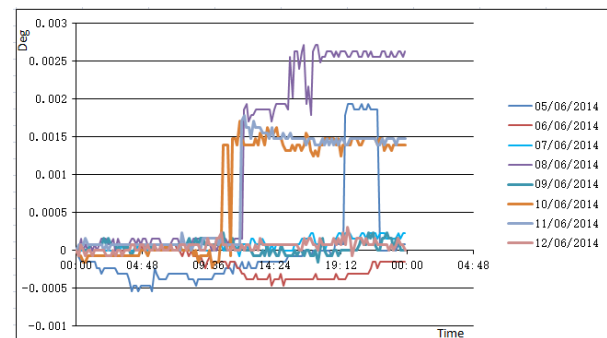
Fig. 7. Results of continuous measurement of the bubble.

4. conclusion

Even small changes in land position can be measured successfully from this experiment and the obtained measurements were proven reliable. As the setup cost is very low, it can be implemented in large scale. The major advantages of the proposed method are that it is not affected by electrical noise and it is less susceptible to temperature changes.

Anyhow, measurement cannot be done when the liquid inside the bubble tube is inflated at high temperature or when it is frozen at low temperature causing the disappearance of the bubble. Hence field observations in such extreme hot or cold regions should be done with a temperature control device.

The analysis is used to evaluate the factors related to land displacement measurement, formulate the measurement technique and to predict the landslide hazard in future.

References

[1]. Sasahara Katsuo, Tamura Keiji (2010) "Simulation model of surface displacement of steep slope made of granite soil under middle scale rainfall", *Journal of the Japan Landslide Society : Landslides* 47(3), 155-160.

[2]. Mo Yang, Masanori Itaba, Atsushi Minato, Satoru Ozawa (2013) "Development of perpendicular sensor and Its Application for Raging", *ISCIU6*, 75-76.

D01

The Relationship between the Thrombogenicity and the Generated Flow around 3-Dimentional Micro Geometrical Structures on the Bio-material -Investigation of Micro Flow-

○Akiko Ota-Ishigaki*, Toru Masuzawa*, Takayuki Shibata**,
Takahiro Kawashima**, Osamu Maruyama***
*Ibaraki University, **Toyohashi University of Technology,
*** National Institute of Advanced Industrial Science and Technology
E-Mail: *11nd209s@vc.ibaraki.ac.jp, ** shibata@me.tut.ac.jp, *** osamu.maruyama@aist.go.jp
Keywords: Thrombogenicity, Surface Roughness, Micro Geometrical Structure, Micro Flow,

1. Introduction

The problems of blood compatibility have researched to develop artificial hearts and artificial valves for long time. However, many researches have focused on the effect of electrical and chemical property of bio-materials on blood compatibility [1]. But, Biological reaction on bio-materials are complicated and have not yet revealed.

To develop artificial hearts, thrombus formation on artificial heart surface is a serious problem to prevent infarct [2]. The cause of thrombogenicity, that are electrical and chemical nature on artificial material, blood property, shear flows in an artificial heart and surface roughness [3], are reported in a lot of study.

However, several factors are intricately interrelated and have not yet revealed completely. Especially, the contributions of surface roughness on the blood compatibility are reported that not only to cause thrombogenicity but also to inhibit thrombogenicity as 'textured surface' [4]. The complicated reaction in thrombogenicity process on the rough surface has to be investigated for improvement of blood compatibility in artificial organs. It is considered that the shear flow in micro level cause thrombogenicity on a rough surface. The irregularities on the rough surface generates complex flow on rough surface, and it is difficult to evaluate relationship between micro shear flow around irregular pattern and thrombogenicity. Therefore, we focused on 3-dimentional micro geometrical structures composed of roughness surface.

The objective of this study is to investigate the relationship between the thrombogenicity and the generated flow around 3-Dimentional micro geometrical structures on the material. Flow conditions around 3D micro geometrical structures on a silicon surface are reported in this paper as a basic study.

2. Method

2.1. CFD analysis for flow visualization

The flow condition around micro cylinders on a test piece are analyzed with Computational Fluid Dynamics (CFD) analysis. The range of 20 mm square flow part as Figure 1 is built for CFD model. The flow part was modeled using about 10,000,000 hexahedral elements. The analysis was calculated with laminar flow model. The condition for the CFD analysis is shown in Table 1.
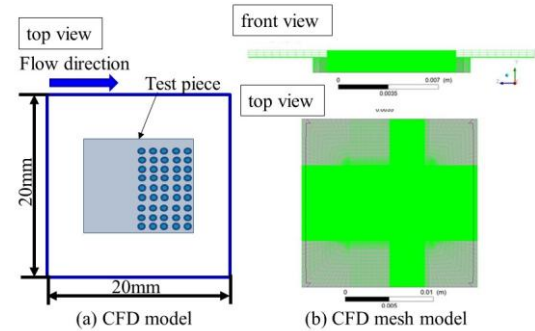
Fig. 1. CFD model and CFD mesh model

Table 1. CFD conditions

Software		ANSYS CFX Ver.14
Boundary Condition	Flow in	0.1 L/min
	Flow out	0.1 L/min
	Wall	No slip
Working Fluid	Viscosity(blood)	0.003 Pa*s
	Density(blood)	1050 kg/m^3
The number of mesh components		About 10,000,000
Analysis model		Laminar flow model

2.2. Experimental Flow visualization

Silicon test pieces with 3D micro geometrical structures are constructed by Micro Electro Mechanical Systems (MEMS) as shown in Figure 2. The test piece size is 10×10 mm, and 9 rows 5 columns of micro cylindrical structures are set at backward of flow region. The cylinder has a diameter of 10 mm and a height of 50 μ m. The distance between each cylinders are set to 1000 μ m to avoid flow interference.
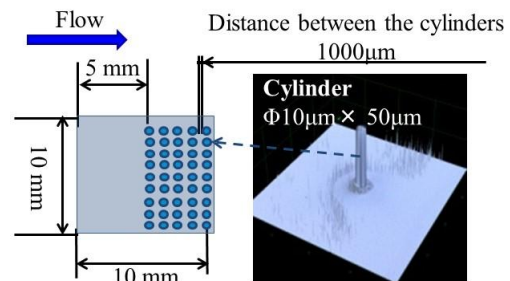
Fig. 2. Test piece with 3D micro geometrical structures

Figure 3 shows a perfusion chamber that is designed as widen inlet and narrow outlet to prevent secondary flow and eddy flow in the chamber. The fluid channel height is 1 mm. The test piece is set at 11 mm square groove of the chamber. There is a clearance between the 11 mm square groove and the 10 mm square test

D01

piece for priority setting of the test piece.

Fig. 3. Perfusion chamber

A perfusion test circuit are assembled for flow visualization to evaluate flows which are generated around the micro 3D geometrical structures (Figure 4). The chamber connected to a peristaltic tube pump (RP-2100, Tokyo RIKAKIKAI co.) and a 200 mL beaker with connecting silicon tubes.

A polyvinyl alcohol (NA-150 YAMATO) as a tracer particle are mixed in the water. The mixed water was filled in the circuit and perfused in the circuit at 200 S^{-1} (Flow rate is about 0.1 L/min) on the test piece that was controlled with the peristaltic pump for 20 min. After perfusion, test piece was removed and observed pigment adhesion around the geometrical structures by using a 3D laser measuring microscope (LEXT OLS4000-SMT, Shimadzu Co.).
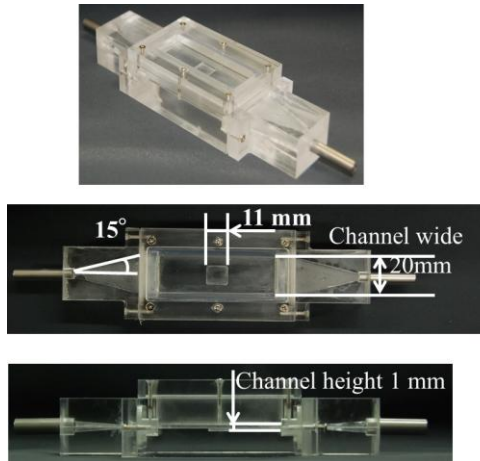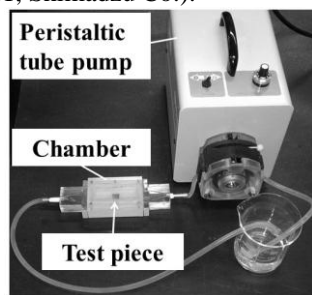

Fig. 4. Perfusion test circuit for flow visualization

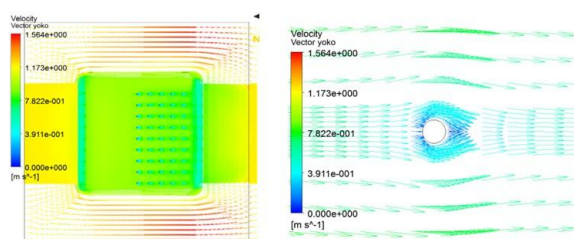## 3. Result
3.1. CFD result

Fig. 5. Velocity vector

Figure 5 is shown the CFD result as velocity vector. The left and right pictures show overall of the CFD model and close up of one cylinder, respectively. The flow between each cylinders didn't interact each other as a left picture. No turbulence flow shown on the test piece. Slow flow is shown near the cylinder root compare with the middle point of cylinders.

3.2. Experimental result

Figure 6 is shown the observed result of perfusion with the mixed polyvinyl alcohol in the water. The left picture shows the bellows half of cylindrical line-columns photographed by a 2.5 times lens, and the right picture shows one cylinder photographed by a 50 times lens. Agglomeration of a polyvinyl alcohol was observed around the root of cylinders. However, irregular adhesion was shown on the overall test piece.
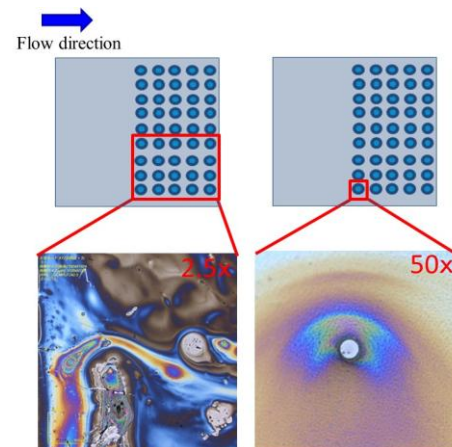
Fig. 6. Observation on the silicon surface and around the cylinder with mixed polyvinyl alcohol

4. Discussion

A polyvinyl alcohol was shown aggregation by the root of cylinder as the result of experimental flow visualization. Adhesion of the polyvinyl alcohol at the cylinder root may have been due to small flow velocity at the root compare with the middle point of each cylinders as shown in the result of CFD analysis.

On the other hand, the polyvinyl alcohol irregularly adhered at overall on the test piece as shown in the experimental result. It is considered that the clearance, between the groove and the test piece, generate turbulent flow cause of fluctuation of the test piece during perfusion. And also, peristaltic tube pump might generate pulsatile flow in the chamber. The blood cell adhesion could be shown at the root of cylinder in the experiment with blood, however, it is need to improve the experimental chamber for inhibition of flow turbulence in the experiment with blood.

References

1]. Lindsey E. Corum *et al.* (2010). "Screening platelet–surface interactions using negative surface charge gradients" *Biomaterials* 31(12):3148-3155
2]. Kirklin JK *et al.* (2013). "Fifth INTERMACS annual report: risk facto r analysis from more than 6,000 mechanical circulatory support patients." *J Heart Lung Transplant.* **32(2)**:141-156
3]. Furukawa KS. *et al.* (2000). "Effect of shear stress on platelet adhesion to expanded polytetrafluoroethylene, a silicone sheet, and an endothelial cell monolayer", *ASAIO* **46(6)**: 696-701.
4]. Yukiko Yamada *et al.* (2011). "Neo intima-inducing inflow cannula with titanium mesh for left ventricular assist device", *Artificial Organs* **14**: 269-275.

D02

Turbidity monitoring of water bodies using color measurement system

○S.H.P.K. Lakesh*, D.D.G.L. Dahanayaka, Jiazhenzhen, Atsushi Minato
Graduate School of Science & Engineering, Ibaraki University, Japan
E-Mail: * lakeshk77@yahoo.com
Keywords: Secchi disk, Turbidity, Water color, Water body

1. Introduction

Turbidity is a parameter of water clarity to a degree to which the water loses its transparency due to the presence of suspended particulates. Suspended materials include soil particles (clay, silt, and sand), algae, plankton, microbes, and other substances. Turbidity can affect the color of the water and therefore water color is essential parameter to evaluate turbidity. Higher turbidity also reduces the amount of light penetrating the water, which reduces photosynthesis and the production of dissolved oxygen (DO). Turbidity can be useful as an indicator of the effects of runoff from construction, agricultural practices, logging activity, discharges, and other sources. Turbidity often increases sharply during a rainfall, especially in developed watersheds, which typically have relatively high proportions of impervious surfaces [1], [2], [3].

Turbidity is generally measured by using a turbidity meter. Another approach is to measure transparency (an integrated measure of light scattering and absorption) instead of turbidity. Water clarity/transparency can be measured using a Secchi disk. The Secchi disk can only be used in deep, slow moving rivers. Both methods have several advantages and disadvantages [4], [5], [6].

Table 1. Comparison of commercial available Turbidity meter with Secchi Disk.

Turbidity Meter	Secchi disk
High accuracy	Low accuracy
High cost	Low cost
No Personnel errors	Personnel errors of the reading
No effect from sun's glare	errors because of the sun's glare on the water
Can be used any time	Can be used day time only

Therefore to avoid these disadvantages we proposed a simple and inexpensive instrument for water color monitoring.

2. Experimental Design
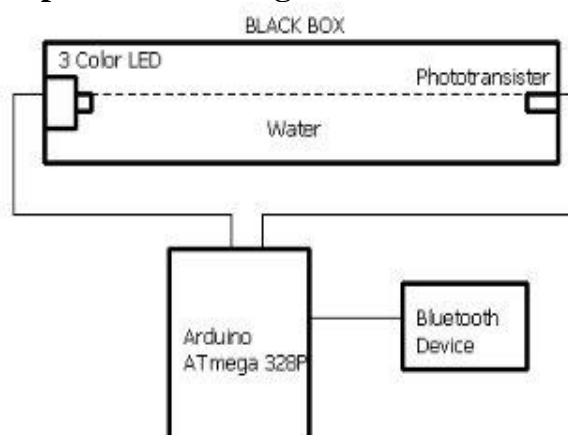
Fig.1. Diagram of Water color monitoring system.

We developed water color measuring system using three color LED and phototransistor.

In this study, we used the Arduino (Atmega 328), the three colors LED (OSTA71A1D-A; Red, Blue and Green LED) and phototransistor (KPT08IM31). Here we fixed the phototransistor and three colors LED in a distance of 15cm each other beside a plastic black box. The size of the box is: 20cm x 3cm x 3cm. In order to avoid the current leak, the both leads of LED and phototransistor are proofed with the water proof adhesive. In addition, the Bluetooth devise(RN/41) is also connected, in order to access the system remotely and powered the system using the three rechargeable batteries (AA 1.2V; 2400mAh) and the current is supplied thorough high efficient single inductor buck-boost converter 1.8-A switched with DC to DC converter (TPS6300) and the 5V output voltage is given to the system. The Figure.1 shows the system design.
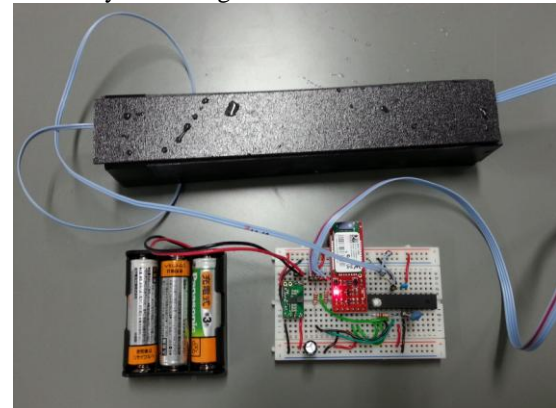
Fig.2. Test Circuit device.
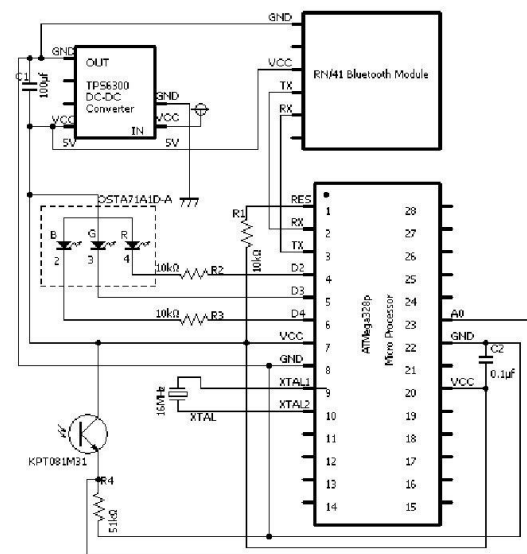
Fig.3. Circuit design of the system

Three color LED illuminates in short time. The voltage of phototransistor corresponds to the intensity of three color lights. These values depend on the absorption of water color between the LED and the phototransistor. In addition, it is capable of sending data to the PC or

D02

Tablets wirelessly via Bluetooth communication. Here we used the android tablet to get RGB data in wirelessly. Figure 2, 3 depict the test circuit device and circuit design of the system. Figure 4 shows the measuring of water transparency using Secchi disk during our previous studies in Lake Senba, Mito, Japan. Commercially available turbidity meter (TN-100), which we used in our experiment works given in figure 5.

Fig.4. Measuring water transparency using Secchi disk at Senba Lake, Japan during our previous studies.

Fig.5. Commercially available Turbidity meter (TN-100).

3. Experiment

For this experiment we used the technique of transmittance between three color LED and phototransistor. According to the water color, the transmittance of RGB value will be change. By getting transmittance RGB value from clear water and different colors (Red, Green and Blue), it is possible to develop accruable and standard water color parameter for turbidity monitoring in the water environment.

At first we put the test box in to the clear water (Tap water) and got the transmittance of the RGB value. After that we got the transmittance of RGB value from a pond (Ibaraki University pond; Lon: 36.57406°N |Lat:140.64251°E).

In the previous studies, we had done the fundamental test using three colors of water and tested the transmittance RGB value and compared it with commercially available spectrometer (SP-300).

According to the data comparison, we understood

that the blue green and red signals are stronger at each colored water.

At the present stage of experiment, we got the transmittance of clear water. The transmittance of RGB value in the pond water was at high level comparing with clear water. Turbidity can be calibrated comparing with clear water. According to this experiment we understood that, it is possible to develop accruable and standard water color parameter for turbidity monitoring by comparing with RGB transmittance value of clear water, reading of both Secchi disk and TN-100 commercially available turbidity meter.

4. Conclusion

The proposed mobile water color monitoring system can be applied to the measurement of water color which used for turbidity and Chlorophyll-a calculation of the water environment. In addition, we plan to conduct continues monitoring and get data at the actual water environment in the next experiment stage. Our previous studies we used the expensive turbidity meters as well as simple Secchi disk methods for the water quality measurements. Since there are disadvantages of commercially available turbidity meters and traditional methods like Secchi disk, we realized that the development of a low-cost portable water color measuring system is necessary to use in monitoring programs of developing countries.

References

[1]. APHA. (1992). "Standard methods for the examination of water and wastewater ". 18th ed. American Public Health Association, Washington, DC.

[2]. Mississippi Headwaters River Watch. (1991). "Water quality procedures". Mississippi Headwaters Board. March.

[3]. Mitchell, M.K., and W. Stapp. "Field manual for water quality monitoring". 5th ed. Thompson Shore Printers.

[4]. Tennessee Valley Authority (TVA). (1995) (draft). "*Clean Water Initiative Volunteer Stream Monitoring Methods Manual*".TVA, 1101 Market Street, CST 17D, Chattanooga, TN 37402-2801

[5]. USEPA. 1991. Volunteer lake monitoring: *A methods manual.* EPA 440/4-91-002. Office of Water, U. S. Environmental Protection Agency, Washington, DC.

[6]. White, T. (1994). Monitoring a watershed: Nationwide turbidity testing in Australia. *Volunteer Monitor.* 6(2):22-23.

D03

Proposal of Android Application for Waiters to Enable Service Like Fancy Restaurant

○Yuji FUJISHIMA*, Masaru KAMADA**

* Graduate School of Science and Engineering, Ibaraki University, ** Computer and Information Sciences Ibaraki University

E-Mail: 14nm718h@vc.ibaraki.ac.jp,

Keywords: Android, POS system, Human recognition, Voice recognition, System enhancement

1. Introduction

Casual restaurants are a resort for families and young people. They offer inexpensive dishes with reasonable quality. In order for better service at lower cost, many restaurants are equipped with a point-of-sale (POS)[1] system for ordering, kitchen scheduling, stock management, billing, and accounting. The current system processes data by the unit of a table and lacks the ability to serve personally each of the guests sharing the table.

We have been developing a software product prototype that converts a Google Android[2] tablet into a POS terminal that is capable of serving guests personally. In this report, we will describe the motivation for this product, its overview and possible impact on the management of casual restaurants.

2. Motivation

We shall review the current restaurant POS systems from the guest's point of view to highlight their problems.

Sitting on a table at a casual restaurant, guests are welcome by a waiter with a handy terminal in his hand. Each guest individually tells the waiter what to have unless the party has a strong leader who is willing to control everything. The waiter inputs the orders one by one as told into the handy terminal. In case the dish offers some optional choices, the terminal prompts the waiter to ask the quest to choose an option.

After taking all the orders for dishes, the waiter says' "Is that all? I repeat what is ordered." Then he starts reading the list of ordered dishes that appears on the terminal. Currently the list is not arranged individually for each guest or in the time-series of orders. The list is rearranged in the order favorable for kitchen scheduling and billing. The bureaucratic declamation of the list is followed by the message "Is that right?" Suppose, for example, that three out of five guests on the same table ordered hamburger stake individually. Each guest remembers what he is going to have. But they cannot calculate easily that there are exactly three hamburger stakes that the party will have as a whole. The guests have no choice other than confirming the incomprehensive list. Otherwise the waiter runs into a deadlock state and the dishes will never be served.

This bureaucratic list in favor of kitchen staff and cashers causes no troubles with the waiter. He has only to ask the same thing every time he brings a dish to the table, "Who is going to have this dish?"

Personalized service makes a restaurant comfortable and even look classy. It would be nice if a waiter takes orders personally, remembers which guest will have which dishes, and brings the dishes straight in front of each guest. That has been practiced for a ling time at the first class restaurants.

A similar personalized service can be practiced even at casual restaurants with a little help from a little more intelligent POS terminal. It is not at all difficult for a computer system to rearrange the list of dishes in the personal form, in the order of kitchen operation, or in any form suitable for a task. The personalized list of dishes is useful even at the casher in case the party wants to go Dutch.

In this study, we concentrate our consideration on the waiter's interface of the handy terminal so that it allow for personalized services.

3. Related work

3.1. Cross i

"Cross i" is the iPad self-ordering system that CROSS-DREAM Inc. has developed.Waiter is unable to identify the person who ordered because this system aggregates the order by the unit of table.

3.2. China fire pot shop small fertilizer sheep

"China fire pot shop small fertilizer sheep" is a smartphone app that webCrew Inc. has developed. This app identifies the location of the table by using the QR code and iBeacon. Also customers can individually order from their smartphones. So this system can identify the terminal that has placed the order but the waiter does not know it.

4. System Overview

The proposed system is an application that runs on Android devices. System overview is shown in (Fig. 1.). The waiter enter ordered items together with the person who ordered in the Android terminal, and the system stores the information. Bringing dishes to the table, the waiter checks the terminal see whom to serve the dishes.
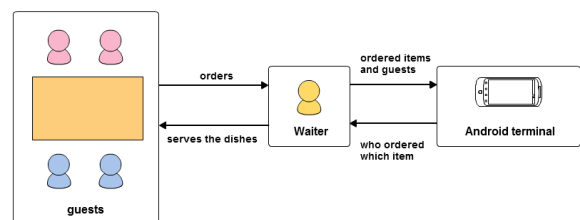

Fig. 1. System overview.

The next section explains the functions of the proposed system.

5. Functions of the system

5.1. Setting the table layout

The user can layout the tables according to each

D03

restaurant. By checking the state of tables in restaurant on the screen such as (Fig. 2.), the waiter can see the status of each table.
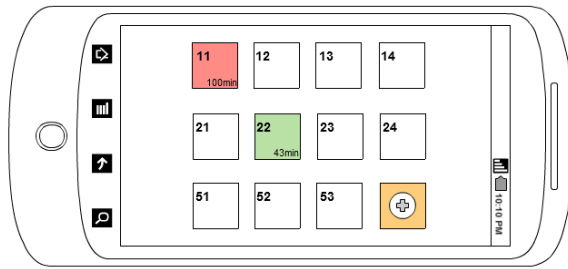
Fig. 2. Screen of checking the state of tables.

5.2. Setting the menu

Function to set items, prices and categories in the menu.

5.3. String with the seat and humans by person recognition

The waiter takes a picture of the guests on the table by the terminal that has a built-in camera when guests have arrived at the table. Then the system extracts persons out of the photo and remembers who is sitting each seat.

5.4. Speech recognition of orders

The terminal analyzes the voice uttered from a customer or a waiter at the time of repetition by voice recognition to pick up the ordered item from the menu.

5.5. Registration of orders

The waiter drags the selected item and drops it onto the guest on the group photo of the table as shown in (Fig. 3.).
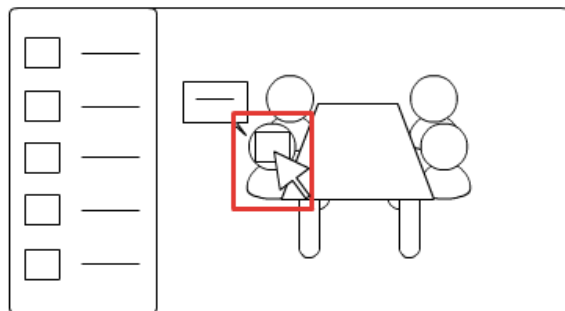
Fig. 3. Order registration by dragging and dropping the item onto the guest.

5.6. Table status view

The waiters and the manager can check the status of each table.

State of the table and their description are shown in (Table. 1.).

Table. 1 State of the table and their description.

State of the table	Description
Empty	The table is empty and clean for new guests.
Waiting for order	We are waiting for the orders.
Now catering	We are serving the dishes.
Now cleaning	The table is to be cleaned.

5.7. Serving the dishes

This feature enables a waiter to know at a glance whom he should serve the dish currently in his hands.

5.8. Accounting

This allows the verification of the ordered items and accounting of the orders of each individual and the entire table.

6. Conclusion

A handy terminal with the proposed user interface will transform an ordinary waiter a skilled one such as working at classy restaurants. This software system is still under development and will hopefully be integrated into the existing POS system for restaurants.

References
[1] http://en.wikipedia.org/wiki/Point_of_sale
[2] http://en.wikipedia.org/wiki/Android_(operating_system)
[3] CROSS DREAM (2010). "Cross i"
[4] WebCreaw Inc. (2014). "China fire pot shop small fertilizer sheep"

D04

Evaluation of band-to-band position gaps in ASTER thermal infrared bands

○Atsushi Kato*, and Hideyuki Tonooka*
*Ibaraki University
E-Mail: *14nm706g@vc.ibaraki.ac.jp

1 Introduction

At-sensor radiances of five ASTER thermal infrared (TIR) bands are converted to surface temperature and the surface emissivities of the five bands through atmospheric correction and temperature and emissivity separation (TES)[1]. In this processing, band-to-band position gaps due to the sensor architecture will produce significant errors. Though band-to-band registration is performed in the level-1 processing, its designed accuracy is 0.1 pixel[2], which may be accurate enough in radiance or temperature-based usage but not in spectral emissivity-based usage, because TES enhances such errors in spectral emissivity images. In the present study, we therefore evaluate band-to-band position gaps on level-1 images using the phase only correlation (POC) method.

2 Methodology

The latitude and longitude at each lattice point (70 pixel interval) are calculated for each band in the level-1 (L1) processing, and stored in each level-1A (L1A) product[3]. Thus, we calculated band-to-band gaps in L1A products using this information (referred to as the method 1). In level-1B (L1B) products, these gaps have been already removed by geometric correction in the L1 processing.

In addition, we applied the phase only correlation (POC) method[4] to L1A and L1B products in order to evaluate more accurate band-to-band gaps (referred to as the method 2).

3 Results

3.1 Test scenes

The two methods were applied to several scenes with various conditions, particularly in latitude and pointing angle. Fig. 1 shows an L1A image at band 11 around Los Angeles as an example of the test scenes used.

3.2 Results for L1A products

The left in Fig. 2 shows the cross-track profiles of band-to-band gaps between the L1A images of bands 11 and 13 for 11 different along-track positions using the method 1, indicating arrhythmic changes dependent on the along track positions. The center in Fig. 2 displays those for 69 different along-track positions using the method 2, showing similar to but more detailed and precise gaps than the method 1's results though some small deviations caused by mismatching in the POC method can be seen. It is likely that the mean profile of the results by the method 2 is the actual band-to-band position gaps due to the sensor architecture.
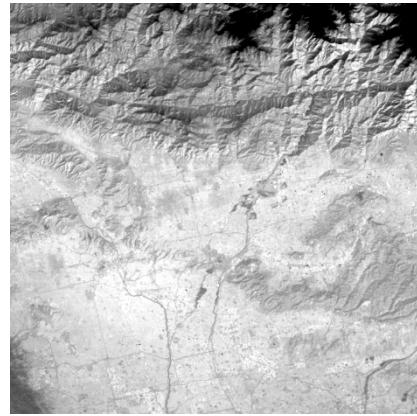
Fig. 1: L1A test image observed at band 11 on 23 January 2005 around Los Angeles, USA.

3.3 Results for L1B products

As mentioned, L1B products which the geometric correction have been applied have the designed accuracy of 0.1 pixel in band-to-band registration, but such errors can give an impact to TES. We therefore applied the method 2 to the L1B image generated from the L1A image used in 3.2. The right in Fig. 2 shows the results, which indicates that position gaps are almost within ±0.1 pixel as expected from the sensor design.

3.4 Impact analysis to TES

Next, we analyzed an impact of the above band-to-band position gaps to TES as follows:

(1) Retrieve surface temperature image by applying atmospheric correction and TES to the L1B image used in 3.3 (ST1 image)

(2) Simulate surface radiance image of each band by combining an ST1 image shifted in the cross track direction and an emissivity of unity, where the quantity of shifting is determined for each band based on the maximum band-to-band position gap of each band

(3) Retrieve surface temperature image (ST2) and spectral emissivity images by applying the normalization method, one of TES algorithms, with the maximum emissivity of 1 to the simulated radiance images of the five bands (if there is no position gaps, ST2 will be identical to ST1, and all emissivity values will be unity. Actually, this is not true due to the position gaps given)

(4) Generate the max-min difference (MMD) image of the retrieved emissivity images of the five bands (if there is not position gaps, MMD will be zero at all pixels. Since the gaps exist in actual, the MMD image can be used for evaluating the impact of such gaps to TES.)

D04

Fig. 2: Position gap profiles between bands 11 and 13 in the cross-track direction (left: method 1 for L1A, center: method 2 for L1A, right: method 2 for L1B)
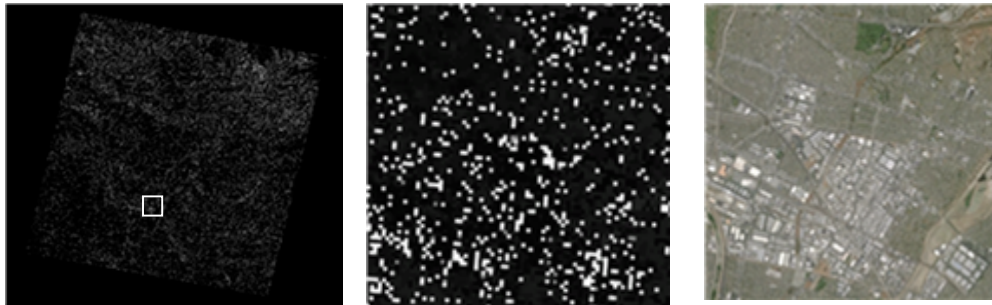
Fig. 3: Obtained MMD image (left). Center is an enlarged image for the white box area on the left image. Right is the Google Earth image for this area.

Fig. 3 shows the MMD image obtained, where a larger MMD indicates a larger spectral distortion in emissivity. Though MMD values are not so large in the whole, they are slightly higher around mou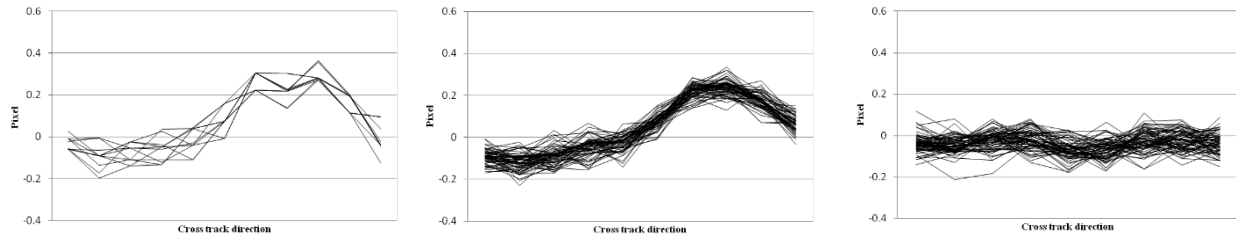ntains probably because spatial variation of surface temperature is larger due to topographic effects in these regions. Some urban areas including large-scale buildings also show large MMD values, because such buildings can be distinguished by ASTER/TIR.

MMD values are about 0.03 in typical, and ±0.065 at maximum. Since the requested accuracy of TES is 0.015 in emissivity, these values are not small in TES.

4   Conclusion

Band-to-band position gaps in L1A and L1B images were analyzed using the two methods, and their impact to TES was evaluated using the actual ASTER/TIR image. As a result, position gaps in L1B images are almost within ±0.1 pixel, but they may give some impacts to TES accuracy. In addition, position gaps stored in L1A products showed unexplainable fluctuation in the band-to-position position gaps at the lattice points. Since the current geometric correction in the L1 processing is performed using these gaps, it may be affected by the fluctuation. Since the POC method in the present study can estimate more accurate band-to-band position gaps, it may be able to improve the accuracy of geometric correction in the L1 processing.

【Reference】
1) A. Gillespie, S. Rokugawa, T. Matsunaga, J. S. Cothern, S. Hook, and A. B. Kahle: A Temperature and

Emissivity Separation Algorithm for Advanced Spaceborne Thermal Emission and Reflection Radiometer (ASTER) Images, IEEE TGARS, 36 (4), 1113-1126, 1998.
2) A. Iwasaki, and H. Fujisawa: ASTER Geometric Performance, IEEE TGARS, 43 (12), 2700-2706, 2005.
3) Algorithm Theoretical Basis Document for ASTER Level-1 Data Processing Ver. 3.0, ERSDAC, 1996.
4) Y.Sasaki, K.Tanaka, T.Aoki, T.Higuchi, and K.Kobayashi: High-Precision Image Registration Based on Phase-Only Correlation, TECHNICAL REPORT OF IEICE, 102 (13), 49-54, 2002.

E01

Diversity of the ABO Blood Group Genes in the Human Population

○Masaya Itou*, Takashi Kitano**
*Graduate School of Science and Engineering, Ibaraki University, **Department of Biomolecular Functional
Engineering, College of Engineering, Ibaraki University
E-Mail: *13nm502y@hcs.ibaraki.ac.jp, **tkitano@mx.ibaraki.ac.jp

1. Introduction

The human ABO blood group consists of three major types, A, B, and O [1]. These alleles code for glycosyltransferases, with the terminal sugar chain modifications varying between types. The enzyme encoded by functional alleles of type A and B transfer a GalNac or a Gal on the precursor. The nucleotide sequences of the human ABO genes have been determined and the molecular basis of these differences has been revealed [2, 3]. The alleles A and B differ in exon 7 by four nonsynonymous mutations, and two of which are critical for the sugar specificity (codons 266 and 268 encode L-G for A and M-A for B). The major O allele has a single nucleotide deletion (Δ261) in exon 6 [4] that induces a frameshift, resulting in a truncated protein deprived of any glycosyltransferase activity.

Major haplogroups (A101, B101, O01, and O02) exist in the human ABO genes [5, 6]. A101 and B101 are the main haplogroups for the A and B alleles, respectively. O01 and O02 are the main haplogroups of the O type. A series of nucleotide differences have been observed between O01 and O02 [5-7].

Several studies have examined the evolution of the human ABO genes [5, 7–11]. These studies have identified that the A allele is the most ancient, because the chimpanzee, which is the closest relative of humans, has A and O alleles. The O allele of the chimpanzee has evolved by a different mechanism compared to humans [9, 11]. The B allele diverged from the A allele, with nucleotide substitutions on the two critical residues in exon 7. The O02 allele diverged from the A allele with a single nucleotide deletion (Δ261) in exon 6, after which the O01 allele diverged from the O02 allele. In contrast, there are some studies [12, 13] that argue trans-species polymorphism of the A and B alleles. In any case, these studies suggested that these alleles have been maintained by balancing selection.

2. Materials and Methods

2.1. Datasets

We retrieved two kinds of phased haplotype datasets for the ABO genes from the HapMap Project [14]. The first was the three population dataset (3pop_data) that included the Yoruba in Ibadan, Nigeria (YRI), Utah residents with ancestry from northern and western Europe (CEU), Japanese in Tokyo, Japan, and Han Chinese in Beijing, China (JPT+CHB). The other dataset contained eleven populations (11pop_data) including African ancestry in Southwest USA (ASW), Chinese in Metropolitan Denver, Colorado (CHD), Gujarati Indians in Houston, Texas (GIH), Luhya in Webuye, Kenya (LWK), Mexican ancestry in Los Angeles, California (MEX), Maasai in Kinyawa, Kenya (MKK), Toscans in Italy (TSI), YRI, CEU, CHB, and JPT.

2.2. Phylogenetic Analysis

Phylogenetic networks were constructed manually following the procedures of [8, 15]. A chimpanzee sequence data was used as an outgroup.

2.3. Detection of Recombinant

We attempted to detect recombinants from the phylogenetic network analysis following the procedure of [16]. We used model data to explain how to infer a recombination event from a phylogenetic network (Fig. 1).
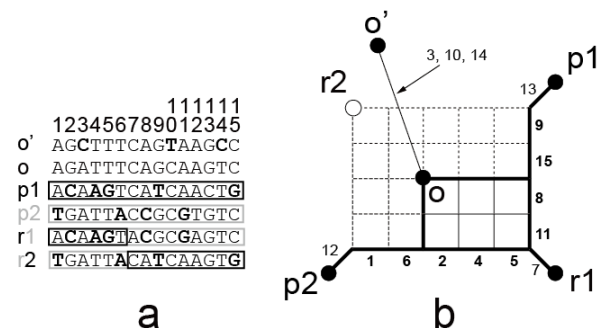
Fig. 1. Explanation of a recombination event in a phylogenetic network using model data. A nucleotide sequence (a) and a corresponding phylogenetic network (b) are shown.

First, an ancestry sequence (o) produces two different sequences (p1 and p2) (Fig. 1a). The p1 has five substitutions (2, 4, 5, 9, 15), and the p2 has four substitutions (1, 6, 8, 11), from sequence o. Then, if recombination occurred between sites 6 and 7 for p1 and p2, two recombinants (r1 and r2) exist. After the recombination, three nucleotide substitutions at sites 7, 12, and 13 accumulate to p1, p2, and r1, respectively, and three nucleotide substitutions (3, 10, 14) also accumulate to produce an outgroup (o') from sequence o. Assuming that r1 and r2 were produced by a single recombination event, transmission of both recombinant alleles to the next generation is highly improbable. Therefore, we assumed that r2 had disappeared. Fig. 1b is the phylogenetic network represented by Fig. 1a at the time. The phylogenetic network (Fig. 1b) indicates the relationship between the extant alleles (p1, p2, and r1) and an outgroup (o'). Two parental alleles (p1 and p2) are located on opposing vertices of the rectangle and have longer (compared to that of the recombinant allele) external branches, while the recombinant allele (r1) is located on the vertex opposing the outgroup allele (o') and has a shorter (compared to those of parental alleles) external branch. "External branch" means a single line extended from reticulations to an external node here.

3. Results and Discussion
3.1. Phylogenetic Analysis of the Human ABO Blood Group Genes

Fifty-four and 36 SNPs for 3pop_data and 11pop_data, respectively, were retrieved from the HapMap Project, and we predicted ABO types for each haplotype by using haplotype-specific SNPs, following data of [5].

Fig. 2a describes a phylogenetic network using 3pop_data.

Fig. 2. The phylogenetic network constructed from 3pop_data.

The O01 haplogroup is thought to be a recombinant lineage, where the O02 and B101 haplogroups are its parental allele lineages (Fig. 2b). Seven sites support O01 and B101 haplogroup cluster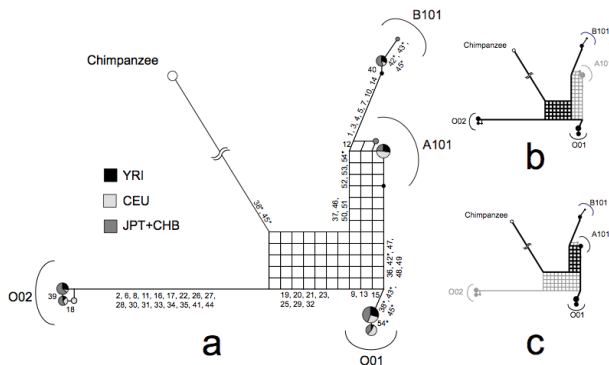ing, while five sites support O01 and O02 haplogroup clustering. The recombination point is estimated to be between intron 2 and intron 3. It is also thought that the A101 haplogroup is a recombinant lineage, where its parental lineages are the O01 and B101 haplogroups (Fig. 2c). We can expect that the recombination point is located in exon 6, because A101 should not have Δ261.

We also used 11pop_data, which contains data from 993 individuals from the world, but the number of SNPs is lower at 36 compared to 54 in 3pop_data. The phylogenetic networks indicated similar results to 3pop data. Since each haplogroup consists of individuals from several populations, it is suggested that they had been formed before divergences of human populations, that is, prior to migration out of Africa. In addition, we observed the v haplotype, which is a rare haplotype, and this haplotype could not be predicted as a known haplogroup.

3.2. Evolutionary History and Diversity of the Human ABO Blood Group Genes

We assume A as an ancestor in humans, because chimpanzees mainly have A alleles [9, 11, 17]. B101 then diverged from A, followed by substitutions for the two critical sites, and O02 diverged from A with Δ261. O01 might be formed by a recombination coupled with gene conversions between B101 and O02 [6]. A101 is the recombinant product with the intact exon 6 from B101 and two critical A type sites inexon7 from O01 that had been joined to form the functional A allele. The results from this study, using the HapMap data, mirror the results of [6]. A101 should be distinct from the ancestral A allele, which produced the B101 and O02 haplogroups. It is not clear whether the ancestral A allele coexisted with other haplogroups in modern humans. If the

ancestral A allele exists in the human population, it should be located near the common ancestral position with a longer external branch in a phylogenetic network. We observed the v haplotype, which is located near the common ancestral position in a phylogenetic network. Since this haplotype consists of individuals from ASW, CEU, GIH, MEX, and TSI, it seems to have been formed prior to migration out of Africa. Thus, it is possible to expect that the v haplotype may be the ancestral A haplotype, that is, the most ancient haplotype [18].

References

[1]. K. Landsteiner (1901) "Uber Agglutinationserscheinungen normalen menschlichen Blutes" *Wien Klin Wochenschr* **14**: 1132-1134.

[2]. F. Yamamoto *et al.,* (1990) "Molecular genetic basis of the histo-blood group ABO system" *Nature* **345**: 229-233.

[3]. F. Yamamoto *et al.,* (1990) "Sugar-nucleotide donor specificity of histo-blood group A and B transferases is based on amino acid substitutions" *J Biol Chem* **265**: 19257-19262.

[4]. F. Yamamoto (2000) "Molecular genetics of ABO" *Vox Sang* **78**: 91-103.

[5]. F. Calafell *et al.,* (2008) "Evolutionary dynamics of the human ABO gene" *Hum Genet* **124**: 123-135.

[6]. T. Kitano *et al.,* (2012) "The functional A allele was resurrected via recombination in the human ABO blood group gene" *Mol Biol Evol* **29**: 1791-1796.

[7]. F. Roubinet *et al.,* (2004) "Evolution of the O alleles of the human ABO blood group gene" *Transfusion* **44**: 707-715.

[8]. N. Saitou *et al.,* (1997) "Evolution of primate ABO blood group genes and their homologous genes" *Mol Biol Evol* **14**: 399-411.

[9]. N. Kermarrec *et al.,* (1999) "Comparison of allele O sequences of the human and non-human primate ABO system" *Immunogenetics* **49**: 517-526.

[10]. A. Seltsam *et al.,* (2003) "The nature of diversity and diversification at the ABO locus" *Blood* **102**: 3035-3042.

[11]. K. Sumiyama *et al.,* (2000) "Gene diversity of chimpanzee ABO blood group genes elucidated from exon 7 sequences" *Gene* **23**: 454-461.

[12]. J. M. Martinko *et al.,* (1993) "Primate ABO glycosyltransferases: evidence for trans-species evolution" *Immunogenetics* **37**: 274-278.

[13]. L. Ségurel *et al.,* (2012) "ABO is a trans-species polymorphism in primates" *Proc Natl Acad Sci USA* **109**: 18493-18498.

[14]. The International HapMap Consortium (2003) "The International HapMap Project" *Nature* **426**: 789-796.

[15]. H. J. Bandelt (1994) "Phylogenetic networks" *Verh Naturwiss Vereins Hamburg* **34**: 51-71.

[16]. T. Kitano *et al.,* (2009) "Relic of ancient recombinations in gibbon ABO blood group genes deciphered through phylogenetic network analysis" *Mol Phyl Evol* **51**: 465-471.

[17]. A. Blancher *et al.,* (1997) "Molecular biology and evolution of blood group and MHC antigens in primates" *Springer.*

[18]. M. Itou *et al.,* (2013) "Analysis of a larger SNP dataset from the HapMap project confirmed that the modern human A allele of the ABO blood group genes is a descendant of a recombinant between B and O alleles" *Inter J Evol Biol* **2013**: 406209.

E02

Social consciousness study concerning rational use of energy in the city districts based on the research in the area of Kashima city

○Kazuki TANABE*，Toshiaki KIN**

*Ibaraki University Science & Technology Division City E&E System Major Dr.course

**Ibaraki University Science & Technology Division City E&E System Major PhD.Professor

E－Mail：*12nd305r@hcs.ibaraki.ac.jp、**tkin@mx.ibaraki.ac.jp

Keywords: cities and districts, rational use of energy, human activities, correspondent consciousness gap

1． Introduction

The direction for the rational use of energy in many cities and districts is positively recognized and actively promoted by the responsible officials in recent years mainly by introducing innovative hardwires. However, the effect of human activities is still unknown and there exist correspondent consciousness gap between the officials and residents.

2． Background of Study

As the energy saving policy, application of the law about rational use of energy has been widely expanded from the industry to the residential and transportation sectors from 1998 till today. But the increase of energy consumption in the city districts is gettung very big. For this reason, many support enterprises to the city areas such as smart community, environment model city, future city and total energy treating model project including to create/store/conserve energy, are undertaken by the responsible relative ministries, from 2008 and afterwards. Moreover, the environmental law was revised[1] and the duty to promote global warming protection measure for all local government bodies was imposed. However, such as enterprises or measures have not yet been carried out in many local governing bodies, as shown in Table 1

Table 1.Number of support enterprises and global warming measures implementation cities

GB		Number of cities and support enterprises							Number of Local governments			
	METI	MOE	COF	MLIT	Number of enterprises		Number of cities		MOE			
Classify	Smart com.	E-Model city	E-Future city	H-Energy city	Enterp. A	Ratio A/D (%)	Cities B	Ratio B/D (%)	LG C	Ratio C/D (%)	Total cities D	
ODC	3	5	2	1	11	55	7	35	9	45	20	
MUC	0	5	2	2	9	20.9	7	16.3	31	72.1	43	
SDC	0	0	0	1	1	2.5	1	2.5	17	42.5	40	
Other city	1	13	7	6	27	1.7	25	1.5	82	5	1640	
Total	4	23	11	10	48	2.8	40	2.3	139	8	1743	

Note: GB:Government body in charge, ODC:Ordinance-designated city,
COF:Cabinet Office,MUCMajor urban City, SDC:Specially designated city
MLIT:Ministry of Land, Infrastructure, Transport and Tourism, Smart com.:Smart communty
METI:Ministry of Economy,Trade and Industry, MOE:Ministry of Environment,
E-:Environmental, H-:Hybrid with Renewable Energy,Storage of Energy and Emergy conservation
Enterp.:Enterprises, LG:Local government implementing global warming protection measures

This table is the writer creation from the ministries 'official information

3． Promotion organization outline

About the promotion organization, according to the regional characteristic situation, the subjects are mainly promoted by a respective local governing body, companies and experts, by introducing mainly every type of energy management systems, new transportation systems, natural-power-sources and energy efficient

equipments. For the global warming protection, local governments lead the measures with regional universities, experts, suitable organization representatives. But it is presumed that the action to the residents who are the leading role in a city area is extremely insufficient

Table 2.Implementation structure

This table is the writer creation from responsible officials & city homepage publicity matters

Implementation Structure	Support Enterprises for designated cities		Global Warming Measures for every cities/by the Law		(Reference) EC Mmeasures
Classification	City Area	Home	LG Area	Home	DEM Factory
GB	METI,MOE, COF,MLIT		MOE	(Eco-Audit)	METI／ANRE
Main Promoter	LG	PR & DASS	LG	PR & DMPS, Eco-Audit	DEM Factory
Cooperator	Univ.,Expert		Univ.,Expert		DE Manager EC Tech. Support Company andSpecialist
	Company, Office		Company, Office		
	Community		Community		
Home Promoter					DEM to All Processes

Note EC：Energy Consevation、LG：Local Government
Univ.：University, PR：Propaganada (Information Popuralization)
DASS：Designated (Limitted Area) Support System
DMPS：Designated Members Promortion System for Grobak Warming Measure
DEM:Designated Energy Management , DE:Designated
EC Tech.:Energy Conservation Technology, DEM:Designated Energy Manager

4． Purpose of Research

Even the support enterprises and the global warming protection measures are promoted or not, it is thought there is a big gap of information between the promoters and the residents about the consciousness of autonomous cooperation. The purpose of this research is to make clear the existence of the gap at Kashima city, as a typical city without promoting both the enterprise and measures, and to propose a suitable method to fulfill the gap. It will be applicable not only many cities in Japan but also the cities of foreign countries who want to promote residential sectors energy conservation.

5． Present Problem

The following problems are recognized from the above mentioned contents.

(1) The number of local governing bodies who are enforcing the enterprises and measures is very small size comparing the total number of local governing bodies.

(2) Furthermore, for the enterprises and measures promotion, instead of official members the number of participants from residents is very insufficient.

(3) In these situation, for the residents, it is presumed that there are a few opportunities to receive suitable information of rational use of energy.

Therefore there exists the gap, or insufficient supply of information between the promoters and the residents beyond the attitude formation[2] of rational use of energy conservation.

E02

6. Research and Questionnaire

In Kashima[3] of Ibaraki prefecture, as the typical city of not doing the enterprise nor the measures against global warming, the research was carried out with questionnaire. Five researches were performed as pilot surveys for the visitors at the civil and environmental exhibition from 2011 to 2013 (in every exhibition, the total number of visitors is about 3,000 persons, answered person to the simple questionnaire is about 150 persons respectively). And as the main survey, two times of research with precise questionnaires were performed for the Kyuchu area, central district of Kashima city.

Ist time was performed with paying attention to the consciousness of energy saving (24.5%, 492 copies of recovery rate by a random mailing system for the Kyuchu area 2,000 household), and the 2nd time mainly paying attention to the practice situation of energy saving (18.5%, 496 copies of recovery rate for the said circumference area 3,000 household).

7. Analysis Result

7.1. Energy Saving Navi Spread Situation

The result of the energy saving Navi install situation in pilot surveys are shown in Fig.1.
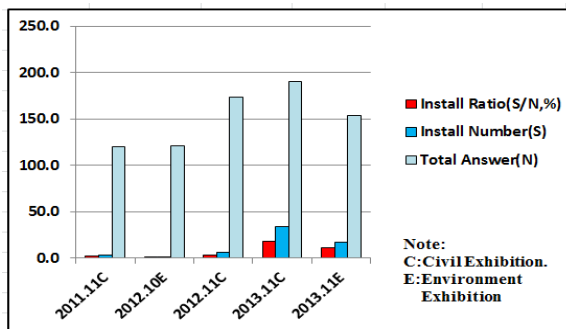

Fig. 1. Energy-saving Navi install situation transition

The information was supplied with practical and simple explanation at the energy saving corner in the civil exhibition concerning energy and environment.
This is the more effective way of spreading information individually for the visitors comparing the way of open public spreading. In this way the energy saving Navi, till then hard to be public, was expected the install volition to be improved.

7.2. Residents' energy saving consciousness

As the main information source for the residents is overwhelmingly dependent on the newspapers and media devices, so it is obvious that there are very few opportunities to be instructed individually the exact practical information by the specialist.

In addition, the recognition level concerning the energy saving basic keywords those started about fifteen years ago, such as the top-runner system (start in 1999) ,the label system (2000), Navi (1999) and HEMS (Home Energy Management System, 2007) were still in very low stage, nearly 10% of recognition rate.
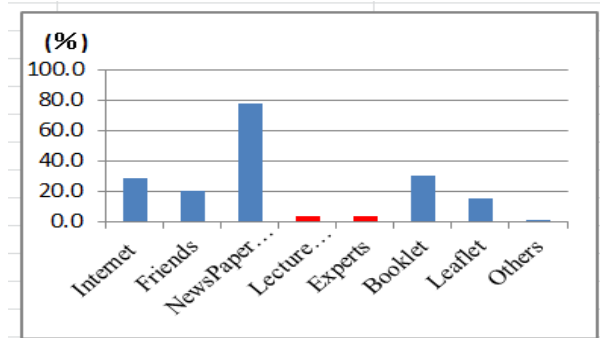
Fig. 2.Sources of information for residents

7.3. Effect by the information

From the analysis of questionnaire in 2013, the actual energy saving situation is rather exclusive for the residents who had recognized the importance of the electric power
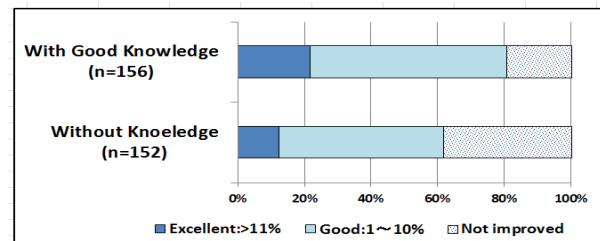
details (this is statistically analyzed by chi square analysis as 5% significant).

Fig. 3. Knowledge of Energy consumption details,

From the results of questionnaire in 2014, the recognition situation of the electric power details, as a few limited tool of "visualization[4]", is relatively high level of 68%. There is also other effective method of energy saving diagnosis to the individual offered homes, but in this present situation, with such a method, the number of performance have been very limited.

8. Conclusion

The promotion of rational use of energy in the city districts is the inevitable subject. To the residents who are the individual main energy users, suitable information supply is not sufficient. Therefore, there exist information gap to the residents. The most effective way to fulfill the gap, will be the individually information supply system to the residents instead of existing public supply system.

References

[1]. MOE officers (2009)"Municipal corporation execution plan"< http://www.env.go.jp >(13.05.2014)

[2]. K.Okada et al."Existence and Attitude formation consideration" Business creative study Feb.2010,1-11

[3]. KashimaLG officers, researcher K.Tanabe et al. (24.03.2012)" The third Kajima city comprehensive plan (FY2012-2031)"

[4]. Y.Motofuji(2012)" Possibility of energy saving in the home by energy visualization system"Y.Motofuji Japan Institute of Energy 2012.91 (7) 563-569

E03

Optimum utilization of fly ash for achieving properties of high performance concrete

○Anjeza Alaj*, Tatsuya Numao**
*PhD student Ibaraki University, **Professor, Ibaraki University*
E-Mail: *anjezalaj@gmail.com, **numao@mx.ibaraki.ac.jp.com*
Keywords: fly ash, compressive strength, chemical analyses, optimization.

1. Introduction

Coal fly ash is obtained as final product by combustion of coal in power plants during process of producing electrical energy. In conventional power plants the combustion of coal usually takes place at temperature (1200-1700)°C and these ashes is major part of all remnant after producing energy.

In Kosovo electricity production and its generation is dependent largely based on coal burning power plants. Currently 97% of electrical energy is produced only from coal and based on reserves of this mine and the situation of other resources it seems that for long time coal will be the only source of energy. As result average of coal fly ash is around 1,16 million t/year [1].

So, considering this situation, idea of substituting different percentage of cement with coal fly ash in producing concrete will help to reach the point of recycling waste material, reducing amount of cement production, increasing quality of concrete, protecting environment and it has positive effect in economical aspect too

The literature is rich in publications regarding influence of fly ash in concrete, especially for low-calcium fly ash (less than 10% of CaO) [2-4] but suitability of high-calcium fly ash in concrete still is anticipated with skepticism [5]. These happen especially related to chemical compositions high content of CaO and SO_3 can affect volume stability and concrete stability [6,7,8].

Following this approach, an experimental investigation of quality of concrete with different percentage of high-calcium fly ash content is carried out. In focus is high performance concrete C 50/60 and all work took place in concrete lab in Prishtina according to EN 206-1.

Table. 1. Physical properties of fly ash.

Fineness	
• 0.200mm	0.1
• 0.090mm	4.9
• 0.063mm	8.1
• 0.043mm	12.5
Capacity mass g/cm³	2.83
Specific surface cm²/g	6 600
Pozzolanity MPA	
• Flexural	4.5±0.3
• Compressive	21.1±0.7

2. Materials, mixture proportions and experiment procedures

Table 1 and 2 shows physical properties and chemical compositions and of fly ash and cement. Table 3 shows mix compositions for eight different mix design including control concrete with 440 kg/m³ cement content until 50% cement replacement with fly ash. All specimens were removed from molds after 24 hours and cured in 22°C and 99% relative humidity until examination day, after 3, 7, 21, 28, and 56 days.

It must be emphasized that to reach results of compressive strength of concrete was applied European standard EN 206-1 and used specimens were in cubic shape (15x15x15)cm and each value was average of minimum three results from different samples in different period of curing.

Table. 2. Chemical compositions of cement and fly ash.

Elements	Cement	Fly ash
SiO_2 %	19.79	19.28
Al_2O_3 %	6.13	5.67
Fe_2O_3 %	2.73	4.85
CaO %	63.86	42.92
MgO %	2.42	4.31
SO_3 %	2.98	19.41
Na_2O %	0.19	0.58
K_2O %	0.68	0.36
MnO %		0.08
LOI %	4.14	2.30
Chromium VI mg/l		0.395
Moisture 105°C %		0.29
CO_2 %	0.59	0.70
Insoluble residue in HCL/Na_2CO_3 %	0.20	11.05
Insoluble residue HCL/KOH %	0.10	6.58
Reactive CaO %	1.50	28.44
Reactive SiO_2 %		15.69

3. Results and discussions

During conducting the experiment it was observed that content of fly ash can effect on some properties of fresh concrete. Increasing of fly ash content the workability of concrete was increased. Mass of fresh concrete was stickier even more bleeding and segregation was not observed.

Workability was measured by slump test, and it was kept constant according curve S3 based on European standards, see table 3.

The compressive strength of all different mixing of fly ash concrete at early ages was lower than control

E03

concrete, the strength decrease gradually by increasing fly ash content. At 3 days old, specimens show the compressive strength of M2-M8 of mix designs were (57 – 31.2) MPa, while for M1 it was 59MPa. By the time compressive strength of fly ash concrete was increased, so after 56 days M2 – 10% fly ash content reached 75.2MPa. Respectively 101% compared to control concrete. See fig 1.

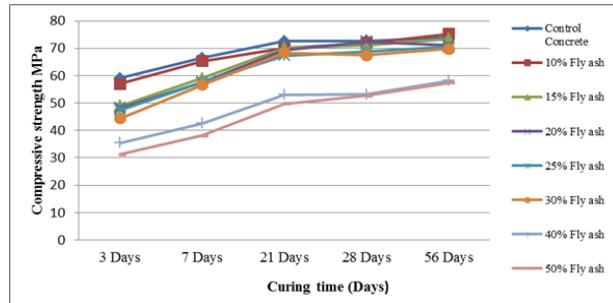**Fig. 1. Compressive strength of concrete against fly ash.**

Table.3. Mixture proportions for 1m ^{3}high performance concrete C 50/60

1/2

Materials	M1	M2	M3	M4
Cement (kg)	440	396	374	352
Fly ash (kg)	0	44	66	88
Sand (kg)	790	783	780	777
Gravel (kg)	965	958	954	951
Water (kg)	176	176	176	176
Additive (kg)	4.40	4.40	4.40	4.40
W/C ratio	0.34	0.41	0.38	0.35
Slump (vm)	12	11.5	15	15

2/2

Materials	M5	M6	M7	M8
Cement (kg)	330	308	264	220
Fly ash (kg)	110	132	176	220
Sand (kg)	774	771	775	778
Gravel (kg)	946	943	952	958
Water (kg)	176	176	176	176
Additive (kg)	4.40	4.40	4.40	4.40
W/C ratio	0.34	0.34	0.40	0.40
Slump (vm)	13	11	14	15

4. Conclusion

Results proved that it is possible to achieve high performance concrete by replacing cement with fly ash. It effects in increasing workability in fresh concrete especially together with suitable superplasticizier. The simple optimum percentage of replacing cement with fly ash is proposed to be 20%, based in this short term of examination. But, the study showed that the efficiency factor is not constant, it depend from different parameters including curing time, amount of cement content, chemical and physical properties of fly ash, replacement ratio.
According to this middle time examination replacement

of cement with more than 30% of fly ash will indicate to develop moderate strength in concrete. However, it becomes a possible alternative to use for application of lean concrete, subbase, etc.

References

[1]. Kosovo Government, Ministry of environmental and Spatial Planning (2011). Areas of particular interest – the new mine fields. Institute of Spatial Planning.

[2]. P.K. Mehta (1989). Pozzolanic and cementitious by-products in concrete-another look. Proceedings of 3rd International Conference on the Use Of Fly Ash, Silica Fume, Slag and natural Pozzolanic in Concrete, V.M. Malahotra (ED), ACI, pp. 1-43 (ACI SP-114, Trondhemi).

[3]. R.Sersale (1983). Aspect of the chemistry of additions. Elsevier pp.432-438.

[4]. S.N. Ghosh (Ed) *al.* (1998). Advances in cement Technology. Pergamon. pp. 537-567

[5]. ACI Committee 226 (1987). Use of fly ash in concrete. ACI Mater J 84:382-409.

[6]. Y. Fu, J. Ding, J.J. Beudoin (1997). Expansion of Portland cement mortar due to internal sulfate attack. Cem Concr Res 27:1299-1306.

[7]. Y. Zhang, W. Sun, L. Shang (1997). Mechanical properties of high performance concrete made with calcium high sulfte fly ash. Cem Concr Rws 27: 1093-1098.

[8]. Papadakis VG (1999). Effect of fly ash on Portland cement systems Part I: Low-calcium fly ash. Cem Concr Res 29:1727-1736.

E04

Comparative analysis of different atmospheric sources input to the ASTER/TIR standard atmospheric correction

○Takahiro Uehara*, and Hideyuki Tonooka*
* Ibaraki University
E-Mail: 13nm702a@hcs.ibaraki.ac.jp

Keywords: atmospheric correction, ASTER, GDAS, GSM, MODTRAN

1.   Introduction

The ASTER thermal infrared (TIR) standard atmospheric correction is based on radiative transfer calculation by the MODTRAN code combined with National Centers for Environmental Prediction (NCEP)'s Global Data Assimilation System products which have a spatial resolution of 1-degree grid. Atmospheric correction parameters like transmittance and path radiance are spatially interpolated on a pixel-by-pixel basis from surrounding grid points, but local weather phenomena induced by topography, atmospheric instability and so on are not considered in this approach, which will give some impacts to accuracy in atmospheric correction. In the present study, we therefore evaluate this issue using Japan Meteorological Agency (JMA)'s Global Spectral Model (GSM) with a higher spatial resolution than GDAS.

2.   Objective analysis data

2.1.   GDAS

The GDAS is one of the data assimilation systems operated by NCEP, and its products are used as standard inputs for ASTER/TIR standard atmospheric correction. They cover the whole of the world with a horizontal grid of 1 degree by 1 degree.

2.2.   GSM (Japan Region)

Global Spectral Model (GSM) is one of the numerical weather prediction models operated by JMA. GSM products are used as initial values for the short-term weather forecast of the numerical weather prediction, the week weather forecast, and the typhoon forecast. The GSM (Japan Region) referred to as GSM_JPN is a sub-model which covers only Japan and surrounding areas (N20 to N50 & E120 to E150) with a horizontal grid of 0.2 degree by 0.25 degree.

3.   Methodology

In the present study, we evaluated ASTER/TIR atmospheric correction by a simulation study with different atmospheric sources of GDAS and GSM_JPN for a given time as follows:

[1]   In each grid point of GSM_JPN at a given time, surface air temperature included in GSM_JPN is derived for using it as the surface temperature in the following calculation.

[2]   Surface radiance at that grid point at that time is calculated for each ASTER/TIR band by combining the above surface temperature and an emissivity of unity.

[3]   The surface radiance is converted to the top-of-the atmosphere (TOA) radiance using MODTRAN combined with air-temperature, humidity, and geopotential height profiles included in GSM_JPN.

[4]   Atmospheric correction with GDAS profiles at that grid point at that time is applied to the above TOA radiance for retrieving a surface radiance at each ASTER/TIR band, where the GDAS profiles are interpolated in space if the grid point is not matched with grid points of GDAS (this interpolation is performed also in the actual processing).

[5]   Surface temperature is estimated from the surface radiance by the ASTER Temperature and Emissivity Separation (TES) algorithm.

[6]   The surface temperature obtained in [5] is compared with that given in [1].

4.   Results

GDAS and GSM_JPN products at 00Z, 06Z, 12Z, and 18Z from 1 September to 31 December in 2009 were used in the present study (the number of times is 484).

Fig. 1 shows the root mean square (RMS) of the surface temperature difference images derived from all grid points (see [6]). In the figure, larger values are found in some areas such as the North Kanto district, the Seto Inland Sea, which indicates that GDAS and GSM_JPN profiles gave a large discrepancy in radiative transfer calculations.

The Seto Island Sea showed a larger RMS in September than in other months (the RMS for September is 3.1 K, while that for four months is 1.9 K). This region is surrounded by mountain ranges, so that it has a drier climate in summer than other areas in Japan (e.g., a typical humidity in September is 70% in Okayama City, while it is 78% in Tottori City and 80% in Kochi City). Since such a localized climate is not easy to express in a numerical forecast, it can cause some discrepancy between GDAS and GSM_JPN. This region was also investigated using ASTER images observed around Okayama City at 01:58 on 12 October 2009. Fig. 2 displays the difference image between the surface temperature image retrieved with GDAS and that with GSM_JPN, indicating that the surface temperature in the urban area of the city is about 3 degree C higher in GDAS than in GSM_JPN. Fig. 3 is an image observed by

E04

MODIS band 2 on the same time, showing that the west of Japan was partially covered by isolated clouds. Fig. 4 shows the mean surface temperature differences between GSM and GDAS for 10 by 10 pixels in each of five cities of Tottori, Tsuyama, Okayama, Marugame, and Kochi in the following three cases: ASTER retrievals, the RMS results on 12 October 2009, and the RMS results for the four months. These results indicate that the largest discrepancy probably due to localized climate can be found for Okayama City located in the Seto Inland Sea.

5. Conclusions

In the present study, two kinds of atmospheric sources for the ASTER/TIR standard atmospheric correction, GDAS and GSM_JPN, were first evaluated by the simulation study for Japan and surrounding areas from September to December in 2009, which indicated that some areas like the Seto Inland Sea have a larger discrepancy between GDAS and GSM_JPN probably due to localized climate effects. Then, the two atmospheric sources were compared around Okayama and some near cities using ASTER images

observed on 12 October 2009, showing a surface temperature difference of 3 K between GDAS and GSM_JPN around Okayama. These results indicate that the accuracy of the ASTER/TIR standard atmospheric correction depends on localized climates for which objective analysis data can produce some discrepancy. For higher accuracy, such a localized climate should be considered in the atmospheric correction.

References

[1]. F. Palluconi, G. Hoover, R. Alley, M. J. Nilsen, and T.Thompson, "An atmospheric correction method for ASTER thermal radiometry over land", Jet Propulsion Lab., ASTER Algorithm Theoretical Basis Doc., Pasadena, CA, revision 3,1999.

[2]. H. Tonooka, and F. D. Palluconi, Validation of ASTER/TIR standard atmospheric correction using water surfaces, IEEE TGARS, 43 (12),2005.Author3. (Date of last update). "Web site Title" <URL> (Accessed Date).

[3]. http://www.jma.go.jp/jma/menu/menureport.html

[4]. T. Uehara, and H. Tonooka, Accuracy reduction of ASTER/TIR standard atmospheric correction around Seto Inland Sea, Proc. of the 56th conference of RSSJ, pp.99-100, May 2014
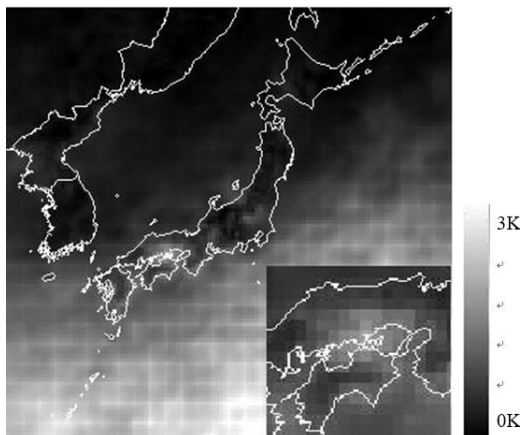
Fig. 1: RMS of surface temperature difference between GDAS and GSM_JPN for four months of September to December, 2009.
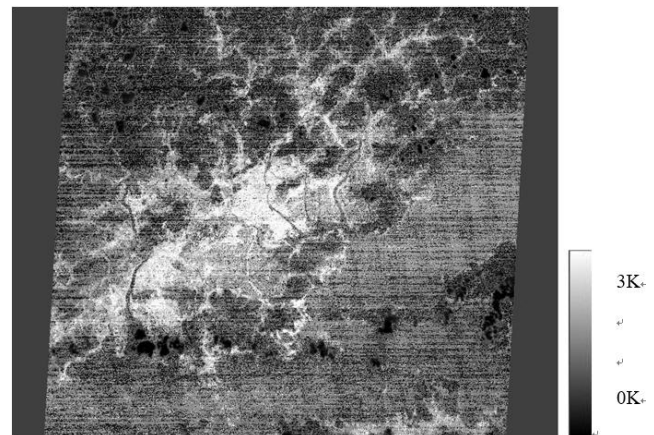
Fig. 2: Difference of surface temperature images retrieved with GDAS and GSM_JPN from the ASTER image observed on 12 October 2009.

Fig. 3: MODIS image observed on 12 October 2009.

Fig. 4: Difference of surface temperatures between GDAS and GSM_JPN for five cities in the three cases of ASTER retrievals, RMS results on 12 October 2009, and RMS results for four months.

F01

A Coloring System for Monochrome Images with Human Faces

○Chisato Nagayama*, Nobuyuki Umezu**
*Department of Intelligent Systems Engineering, Faculty of Engineering, Ibaraki University
E-Mail: *14nm918l@vc.ibaraki.ac.jp, **umezu@mx.ibaraki.ac.jp

Keywords: Coloring, Face Detector, Image Processing

1. Introduction

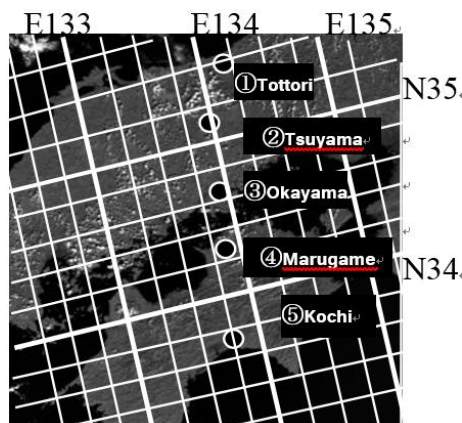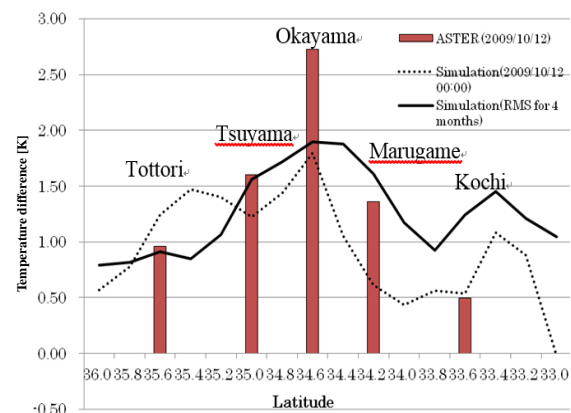The technology of photography was introduced into Japan in 1848. Photograph materials were monochrome up to 1960s. Since amount of color picture's information has more than monochrome photo's [1], research on coloring technology using image processing has been prospering recently [2].

Value of a monochrome image is increased by coloring a face because a face has much amount of information for man. In this study, we develop a system that especially colors a face region in a monochrome image with high precision.

2. Coloring Human Faces

2.1. Skin Area Extraction

Coloring procedures of skin area using the reference color of skin are summarized as follows.

1. Typical skin color is extracted from facial images.
2. The reference color of skin is determined.
3. Our system compares the intensity of each pixel in input monochrome image with it of the reference color.
4. The skin area is extracted and colored using the reference color.
5. Regions outside the face are colored using the existing technique [3].

2.2. Reference Skin Colors

In this study, the target of skin color extraction is limited to images with one person younger than 20 years old. 90 images were collected from internet and an image collection DVD. These images are arbitrary sizes.The computational environment is as follows; Mac OS X 10.7.5, CPU Intel Core i5 2.7GHz, and Memory 4GB. We use HSV color space [4]. We obtain skin colors that a light source state is not influenced by using it.

A distribution of hue and saturation values in rectangle areas including faces are recorded with 90 portrait images (Fig. 1). Hue value varies between 0 to 360 degrees and represents the angle of polar coordinates in Fig. 1. Saturation, whose value is between 0 to 1, represents the radius of polar coordinates in Fig. 1. The intensity of the graph represents the frequency of its corresponding color in the images.

The range of the reference skin color is decided by using a threshold calculated from the histogram of skin color. Our system uses the ranges of region 1, 2, 4 and 6 in Fig. 1 as skin color. The regions 3, 5 and 7 are not suitable for skin color because the area 3 corresponds to almost white in HSV color space and the domains 5 and 6 to pink.

The method above also can be used to determine the reference color of mouth. Our system uses the colors in

region 1 and 4 to paint mouths in images. The colors in regions 2 and 3 are of facial skins (Fig. 1) and unsuitable for painting mouths.
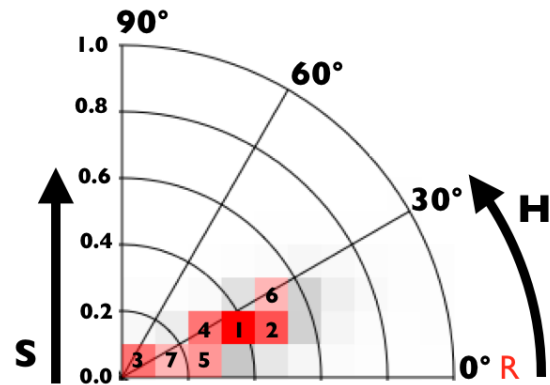
Fig. 1. Skin Color Extraction
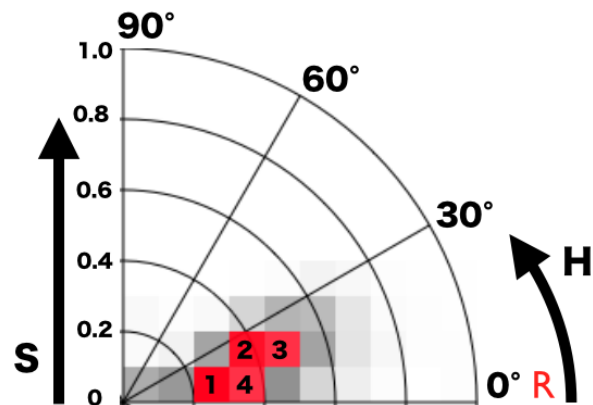
Fig. 2. Mouth Color Extraction

2.3. Skin Coloring

Our system compares the intensity extracted from each pixel in input monochrome image with it of the reference color. A skin pixel is extracted from the skin area in the monochrome image. Then the chromatic component of the reference color with the most similar intensity to it of the pixel, is transferred to color the pixel.

We get the coordinate of a square area including a face in the input image by using face-recognition API of Mac OS. The region is regarded as skin if the following two conditions are satisfied.

1. It has the largest area.
2. The average intensity is within the limits.

A monochrome image has only intensity values, hue and saturation are not included. Our system locates a square area including a face from color images such as Fig.3. The intensity of each pixel in the color image is extracted when the pixel in the square area is close to the reference color of skin. When the intensity of a monochrome pixel is between 0.25 and 0.85, our system leaves only the intensity information and transfers the

F01

reference skin color in Fig. 1. Fig. 4(b) shows a result example.

Our current system colors only in the square area including a face. The pixels are colored using only the comparison between the intensities, coloring is performed over regions outside the face. We need to implement two aforesaid conditions.

The eyes and the mouth are colored in the same skin color because our current implementation handles a single skin color. After painting the eyes and the mouth with the skin color, those regions are painted with more appropriate colors. We locate rectangles on the eyes and on mouse according to the average size and locations calculated by MacOS face recognition APIs (Fig. 5). We determine the reference colors to paint eyes and mouths according the characteristics of those rectangles. We paint bright pixels in the eye region with white and the mouth region with red colors.

Fig. 3. Skin region including a Face

| (a) | (b) |
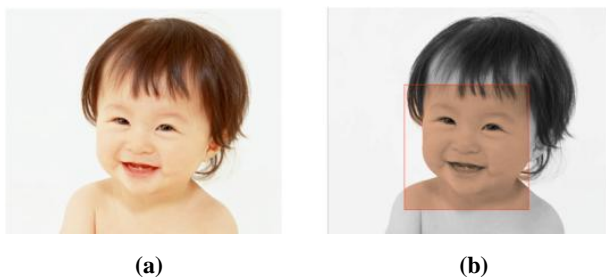
Fig. 4. Example of images used in Experiment
(a) Original image   (b) Coloring result with only intensity comparison
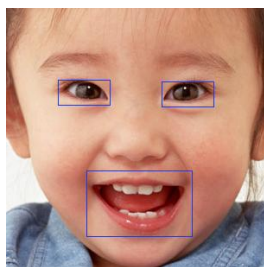
Fig. 5. Rectangles for the eyes and for the mouth

3.   Evaluation of Coloring System
3.1.   Evaluation of Coloring Accuracy

We evaluated coloring accuracy using the correct answer images. A color image is converted into monochrome and used as an input image. We can compute a similarity between the coloring result of our system and the original color image. We use the HDTV type monochrome transform technique. HDTV looks the most natural when it is transformed into monochrome and it is used by the global standard. Five pairs of an original image and our coloring result are used (one example in Fig. 4) and color difference is calculated for each pair. The average accuracy is 89.6 % for 5 pairs.

The precision is reason that the colored area is large. A face is always occupied about 90% in a square area including face. An accuracy judgment is made now only in the square area including a face. Whole image will be colored and judged an accuracy.

3.2.   Evaluation by Examinees

The nature of our coloring result was estimated by 16 students in our laboratory. The coloring result of our system is presented to the examinees and they evaluate the result using the four-level scale. Larger values represent better evaluation. In this study, we aimed at the average evaluation value to be 3.5 or lager. It was 2.6 and smaller than the expected value.

The opinion that flesh color is brighter was acquired through the experiment. The skin color reminded usually is brighter was acquired through the experiment. The skin color reminded usually is brighter than the color of Fig. 4. Man is considered that information is transmitted to a brain after the belief has rectified some brightly rather than the actual color. However, this reason is not only a reason of a fixed concept. The answer images were shown to the subjects. The subjects were made to compare with the coloring result of this system. As a result, the color of an actual skin answered, when the color brighter than a coloring result was carried out.

4.   Conclusion and Future Work

We focused skin color using the distribution model of hue-saturation space. Our system compared the intensity of each pixel in input monochrome image with it of the reference color and colored the pixels. We proposed the extraction method of skin region using the area and intensity average.

Future work includes the reference color spread in H-S space and coloring of the whole input image. Implementation of a region-segmentation and the proposed criteria is also required. We first manually specify the face boundaries of many images to collect face pixels.

References

[1]. C.Morita et al.(2006). "Web Image Retrieval Considering Color Tendency for Colorization of Grayscale Images", Proceedings of the 17th Data Engineering Workshop, 5B-i9

[2]. T.Horiuchi(2007). "Colorization of Monochrome Pictures", Journal of Color Science Association of Japan, Vol.98, No.4, pp.298-303

[3]. T.Welsh et al.(2002). "Transferring Color to Greyscale Images", Proceedings of ACM SIGGRAPH, Vol.20, No.30, pp.277-279

[4] J.M.Chaves-Gonzalez, M.A.Vega-Rodriguez, J.A.Gomez-Pulido, J.M.Sanchez-Perez(2010). "Detecting skin in face recognition systems: A color spaces study", Digital Signal Processing 20, 806-823

F02

Cardio vascular circulation simulator to evaluate ventricular assist effect

○Wataru Kurosaki*, Toru Masuzawa**
*Ibaraki University, **Ibaraki University*
E-Mail: *kurosaki@mx.ibaraki.ac.jp, **masuzawa@mx.ibaraki.ac.jp

Keywords: Heart failure, Ventricular assist device, Coronary circulation, Mock circulation simulator

1. Introduction

Cause of death of the 20% world's population is heart failure [1]. An artificial heart used in the treatment of heart failure is often required to compensate limited the total amount of donor hearts and it has been saving many lives to use as "bridge to transplantation" and "destination therapy". Currently, ventricular assist devices are applicable to clinically, and their multifaceted applications have been extended. One of applications is a therapeutic extracorporeal blood pump which aim to recovery of natural heart of acute heart failure patients. The therapeutic blood pump enhances coronary flow rate of the natural heart and reduces heart load corresponding to the patient condition by regulating pump driving in synchronism with natural heartbeat. The efficacy of treatment with the therapeutic blood pump and the effect of difference in pump driving modes on coronary circulation have been evaluated with animal experiments and it is found that hemodynamic is significantly varied in response to change in pump driving modes. But, animal experiments are difficult to gather quantitative data with reproducibility. The aim of our study is development of a cardio vascular circulation simulator (CCS) for evaluation of the acute heart failure treatment methods utilized the therapeutic blood pump in vitro. The CCS which is mimic the coronary circulation based on the "myocardium pump model" has been developed to evaluate acute heart failure treatment methods utilized the therapeutic blood pump and the performance of it is displayed.

2. Materials and Methods

2.1. Mock circulation systems

The configuration of the CCS with mimic coronary circulation is shown in Fig. 1. The CCS consists of two atrial chambers to emulate left and right atrial, two sack type pumps for ventricles, and resistances and compliance chambers to mimic systemic, pulmonary and coronary vasculature components. The ventricular sack made of silicon is semi-ellipsoid shaped, and has an un-stretched volume of 600 ml. Jellyfish valves with a diameter of 30 mm are set at inlet and outlet of the sack pumps to mimic the cardiac valve. Compressed air is supplied from the pneumatic control device to the ventricle chamber during systole to compress the ventricle sack and to eject the fluid. The compressed air is vented out to atmosphere during the diastolic phase and the fluid in the atrial chamber is flow into the ventricular sack. Pulsatile flow is generated and the Starling's law of the heart is reproduced by this mechanism.

The systemic and pulmonary vasculatures are modeled based on the Windkessel model. Systemic and pulmonary vascular resistances are emulated with pinch valves and the vascular compliance is emulated with chambers to seal air.   The compliance is normally set at 10 ml/mmHg for the systemic venous chamber, 1 ml/mmHg for the pulmonary arterial chamber, 5 ml/mmHg for the pulmonary venous chamber, and 1 ml/mmHg for the systemic arterial chamber. The compliances of systemic and pulmonary arterial are adjustable by controlling the sealed air volume with operating the piston position in the chamber.
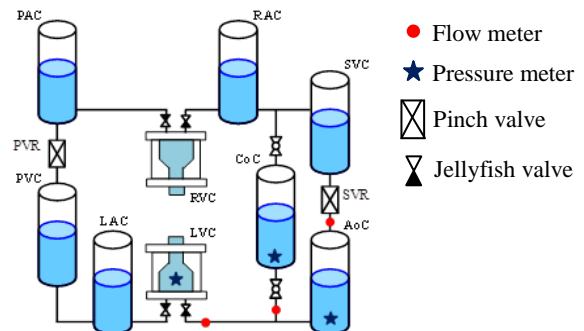

Fig.1 Configuration of the CCS

PVC, pulmonary venous chamber; PAC, pulmonary arterial chamber; RAC, right atrium chamber; RVC, right ventricle chamber; LAC, left atrium chamber; LVC, left ventricle chamber; CaC, coronary artery chamber; SVC, systemic venous chamber; AoC, aortic chamber; SVR, systemic. vessel resistance; PVR, pulmonary vessel resistance.

2.2. Coronary circulation model

The electrical model of coronary, cross-section and overall view of coronary circulation chamber and are shown in Fig. 2. The coronary circulation chamber and electrical model are designed on the basis of "intramyocardial pump model" [2] and constructed from acrylic chamber, diaphragm sheet and piston. The chamber made of acrylic is divided into water and air room by using the diaphragm sheet. The air room is connected to the left ventricle chamber to synchronize the timing of coronary vascular compression with the left ventricular contraction, and the water room is connected between aorta root and vein. Pinch valves at the inlet and outlet ports of the coronary circulation chamber reproduce the coronary artery and vein resistance. The coronary artery compliance is adjusted by changing sealed air volume with the piston as with the compliance of systemic and pulmonary arterial.
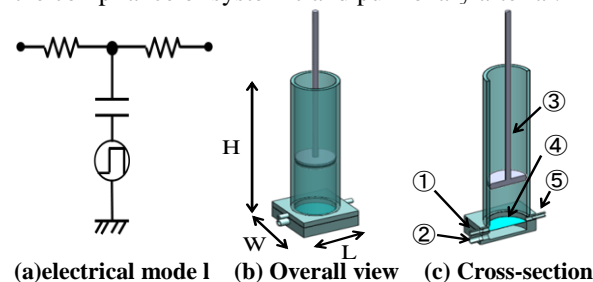
(a)electrical mode l   (b) Overall view   (c) Cross-section
Fig.1 Coronary circulation chamber

①, inlet port (coronary artery) ②, pneumatic device connection ③, piston ④, diaphragm ⑤, outlet port (Chamber size; 120×120×370 mm)

F02

2.3. Evaluation of the newly incorporated coronary circulation model in CCS

To evaluate the performance of the newly incorporated coronary circulation system in CCS, we confirmed whether the mimic coronary flow rate waveform is possible to reproduce the physiological coronary circulation characteristics. Typically, the physiological coronary circulation flow varies according to differential pressure between left ventricular and aorta, it is dominantly in the diastolic phase and occurs regurgitation into aorta during the systolic phase. In evaluation experiment of coronary circulation system performance, the CCS was set at the healthy resting condition. The setting conditions of the CCS were set at 120 mmHg for maximum left ventricular pressure, 100 mmHg for mean aortic pressure, 60 bpm for heart rate, and 40 % for ratio of systolic phase to cardiac cycle.

2.4. Comparison the coronary circulation system in CCS and numerical simulator

The coronary flow rate waveform of CCS was compared with result of numerical simulation to confirm whether the coronary circulation model is incorporated correctly in CCS. The numerical simulation is constructed on the digital simulator based on the differential equations of electrical network to mimic the cardiovascular system. The configuration of electrical network with mimic coronary circulation system is shown in Fig. 3. The ventricular contractility is represented by time-varying capacitances, and vascular resistance and compliance are modeled by electric resistances and capacitors. In comparison test, the each parameters of electric parts (resistance, capacitance and coil) were set to correspond to the experiment conditions of CCS evaluation test.
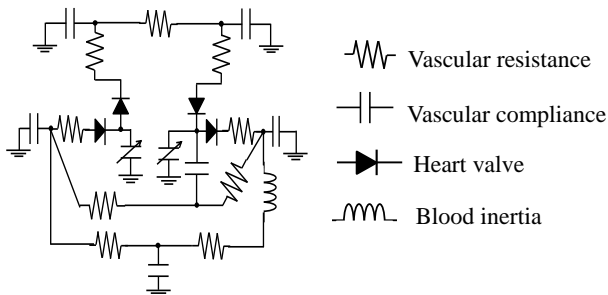

Fig. 3 Electrical network with coronary circulation

3. Result

Fig. 4 shows the coronary flow waveform (CoF) and differential pressure waveform (DP) between aorta and left ventricular at healthy resting condition. Fig. 4(a) is results of CCS and Fig. 4(b) is numerical simulator results. The high state of the synchronous signal indicates systolic phase and the low state of it indicates diastolic phase. The DP of CCS and numerical simulator changed from -38 to 92 and from -30 to 83 mmHg, respectively, in a maximum left ventricular pressure of 120 mmHg and mean aortic pressure of 100 mmHg. The mean coronary aortic flow rate was 310 ml/min and the mean regurgitant flow rate was 340 ml/min in the result of CCS, on the other hand they are 220 ml/min and 82 ml/min in numerical simulator

result. The both results showed a dominantly flow of coronary artery in the diastolic phase, and showed regurgitant flow to aorta during the systolic phase. These features are typical characteristics of the coronary artery flow.
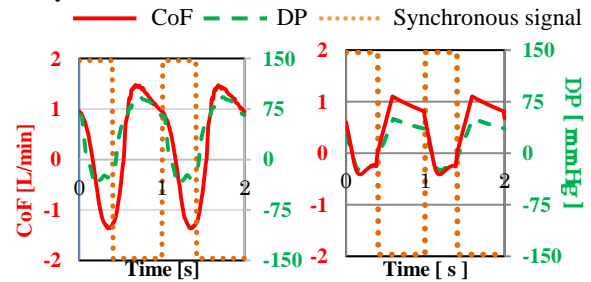
(a) CCS simulator   (b) Numerical simulator
Fig.4 CoF and DP

4. Discussion

The newly developed mock circulation simulator was able to reproduce the coronary flow waveforms. The coronary flow in Fig. 4 is superiority during the diastole phase. Regurgitant flow to aorta, which have been well known phenomenon as "translocation" was observed during the systolic phase. The coronary flow was synchronized with the differential pressure between aorta and left ventricular. The mimic coronary circulation system based on "Intramyocardial pump model" in our CCS can simulate characteristics of coronary flow in the physiological. We compared CCS and numerical simulation based on electrical network to confirm if the coronary circulation model in CCS is corresponded correctly with "intramyocardial pump model". The result of it was consistent with trend of waveform obtained from the CCS, and we confirmed that the coronary circulation systems in CCS correspond with the electrical model of "intramyocardial pump model". On the basis of these results, we will combine numerical simulation with physical model to emulate the physiological response which automatically regulated hemodynamic parameters.

5. Conclusion

The mimic coronary circulation system was newly incorporated in our CCS to evaluate the cardiac failure treatment method with therapeutic blood pump. The coronary circulation system incorporated in CCS reproduced target physiological hemodynamics characteristics of coronary circulation such as "translocation" and "superiority flow in the diastole phase". These results showed similar findings to the numerical simulator results. We will promote investigation regarding auto regulation of hemodynamic parameters, and combine numerical simulation with physical model to improve our CCS to be capable to reproduce more accurately.

References

[1]. Daniel L. Timms, Shaun D. Gregory, Nicholas A. Greatrex, Mark J. Pearcy, Jhon F. Fraser, and Ulrich Steinseifer, "A Compact Mock Circulation Loop for the In Vitro Testing of Cardiovascular Devices," *Artificial Organs*, vol. 35, 2010, pp. 384–391

[2]. Shigeru Ohta, Yasuo Ogasawara, Takeshi Matsumoto, Osamu Hiramatsu, Hiroshi Nakamoto, Takuji Okamoto, Fmihiko Kajiya "Analysis of Coronary Haemodynamics by Coronary Circulation Model with Three Layered Myocardium" IEEE vol. 1995

F03

Extending Infinite Series Representation of Napier's Constant

○ Kunimitsu Takahashi*
Department of Computer and Information Sciences, Ibaraki University
E-Mail: *14nm714l@vc.ibaraki.ac.jp

1. Introduction

Napier's constant is defined as the limit of the convergent sequence

$$e = \lim_{n \to \infty} \left(1 + \frac{1}{n}\right)^n$$

and can be represented in the form of an infinite series

$$e = \sum_{k=0}^{\infty} \frac{1}{k!} = \frac{1}{0!} + \frac{1}{1!} + \frac{1}{2!} + \frac{1}{3!} + \frac{1}{4!} + \dots (1)$$

This infinite series for Napier's constant can be modified to converge more faster to Napier's constant. This article proposes three new infinite series converging to Napier's constant faster than ever and describes a possible means of their further generalization.

2. Extending Infinite Series

2.1. Infinite series compression

The following two infinite series are already known[1].

$$e = \sum_{k=0}^{\infty} \frac{2k+2}{(2k+1)!} = \frac{2}{1!} + \frac{4}{3!} + \frac{6}{5!} + \frac{8}{7!} + \dots (2)$$

$$e = \sum_{k=0}^{\infty} \frac{9k^2+1}{(3k)!} = \frac{1}{0!} + \frac{10}{3!} + \frac{37}{6!} + \frac{82}{9!} + \dots (3)$$

Equality (2) is derived from equality (1) by aggregating every two adjacent terms as follows :

$$\frac{1}{n!} + \frac{1}{(n+1)!} = \frac{n+2}{(n+1)!}.$$

Because this resulting single term represents two terms in equality (1), we   obtain equality (2) by replacing *n* by *2k*.

Equality (3) is derived from equality (1) by aggregating every three adjacent terms as follows :

$$\frac{1}{(n-2)!} + \frac{1}{(n-1)!} + \frac{1}{n!} = \frac{n^2+1}{n!}.$$

Because this resulting single term represents three terms in equality (1), we   obtain equality (3) by replacing *n* by *3k*.

2.2. Extending infinite series

This article presents three new infinite series, which converge faster than (2) and (3), from the algebraic point of view as follows :

$$e = \sum_{k=0}^{\infty} \frac{64k^3 + 16k^2 + 4k + 2}{(4k+1)!}$$
$$= \frac{2}{1!} + \frac{86}{5!} + \frac{586}{9!} + \frac{1886}{13!} + \dots (4)$$

$$e = \sum_{k=0}^{\infty} \frac{625k^4 + 375k^3 + 75k^2 + 20k + 5}{(5k+2)!}$$
$$= \frac{5}{2!} + \frac{1100}{7!} + \frac{13345}{12!} + \dots (5)$$

$$e = \sum_{k=0}^{\infty} \frac{117649k^6 + 67228k^5 + 2401k^4 - 1029k^3 + 833k^2 + 203k + 16}{(7k+3)!}$$
$$= \frac{16}{3!} + \frac{187301}{10!} + \frac{9714770}{17!} + \dots (6)$$

Equality (4) is derived form (1) by aggregating every four adjacent terms as follows :

$$\frac{1}{(n-2)!} + \frac{1}{(n-1)!} + \frac{1}{n!} + \frac{1}{(n+1)!} = \frac{n^3 + n^2 + n + 2}{(n+1)!}.$$

Because this resulting single term represents four terms in (1), we   obtain (4) by replacing *n* by *4k*.

Equality (5) is derived form (1) by aggregating every five adjacent terms as follows :

$$\frac{1}{(n-2)!} + \frac{1}{(n-1)!} + \frac{1}{n!} + \frac{1}{(n+1)!} + \frac{1}{(n+2)!}$$
$$= \frac{n^4 + 3n^3 + 3n^2 + 4n + 5}{(n+2)!}.$$

Because this resulting single term represents five terms in (1), we   obtain (5) by replacing *n* by *5k*.

Equality (6) is derived form (1) by aggregating every seven adjacent terms as follows :

$$\frac{1}{(n-3)!} + \frac{1}{(n-2)!} + \frac{1}{(n-1)!} + \frac{1}{n!} + \frac{1}{(n+1)!} + \frac{1}{(n+3)!}$$
$$= \frac{n^6 + 4n^5 + n^4 - 3n^3 + 17n^2 + 29n + 16}{(n+3)!}.$$

Because this resulting single term represents seven terms in (1), we   obtain (7) by replacing *n* by *7k*.

Table 1 below shows how many terms are required to approximate *e* up to 1, 10, 100, 1000   decimal digits by equalities (1)~(6).

Table 1

Equality	1 digit	10 digits	100 digits	1000 digits
(1)	5 terms	15 terms	71 terms	451 terms
(2)	3 terms	7 terms	36 terms	226 terms
(3)	3 terms	6 terms	25 terms	151 terms
(4)	2 terms	4 terms	18 terms	113 terms
(5)	2 terms	4 terms	15 terms	91 terms
(6)	2 terms	3 terms	11 terms	65 terms

3. Possibility of Generalization

3.1. Sequence of numerator

Equality (2) aggregates every two adjacent terms. By an aggregating a different set of two adjacent terms by

$$\frac{1}{(n-1)!} + \frac{1}{n!} = \frac{n+1}{n!},$$

we have

$$e = \sum_{k=0}^{\infty} \frac{2k+1}{(2k)!} = \frac{1}{0!} + \frac{3}{2!} + \frac{5}{4!} + \frac{7}{6!} + \dots (7)$$

by replacing *n* by *2k*.

Then taking the sum of (7) and (2), we have

$$2e = \frac{1}{0!} + \frac{2}{1!} + \frac{3}{2!} + \frac{4}{3!} + \frac{5}{4!} + \frac{6}{5!} + \dots (8)$$

In the same way, even for aggregation of three terms and four terms, we obtain

F03

$$3e = \frac{1}{0!} + \frac{2}{1!} + \frac{5}{2!} + \frac{10}{3!} + \frac{17}{4!} + \frac{26}{5!} + \ldots, (9)$$

$$4e = \frac{1}{0!} + \frac{2}{1!} + \frac{5}{2!} + \frac{16}{3!} + \frac{41}{4!} + \frac{86}{5!} + \ldots (10)$$

We analyze the sequence appearing in these numerator in the next subsection.

3.2. General term of the sequence of numerator

Solving for the general term of the sequence of numerator in equalities (8), (9), (10) and also others, we find their general term of the sequence of numerator as listed in Table 2.

Table 2

Left side	The general term of the sequence of numerator
e	1
$2e$	$k+1$
$3e$	k^2+1
$4e$	k^3-2k^2+2k+1
$5e$	$k^4-5k^3+9k^2-4k+1$
$6e$	$k^5-9k^4+30k^3-41k^2+20k+1$
$7e$	$k^6-14k^5+76k^4-195k^3+233k^2-100k+1$

3.3. Possible means of generalization of $n \times e$ in infinite series

It is expected that general term in Table 2 can be represented as n is the coefficient of e as follows:

$$f(n) = \sum_{i=1}^{n} \frac{k!}{(k-i+1)!} \ldots (11)$$

Therefore we can represent natural number multiples of e by the infinite series

$$n \times e = \sum_{k=0}^{\infty} \frac{f(n)}{k!},$$

we have the numerator is given by equation (11).

4. Conclusion

We presented more advanced infinite series representation of e by extending the known infinite series. The new ones converge to e more faster.

In addition, we presented a possible means of further generalization. It is yet to see if this further generalization is useful in computation.

References
[1] Representation of Napier's constant
<http://en.wikipedia.org/wiki/List_of_representations_of_e>

F04

Determination of distribution of heavy metals from motor vehicle include a complex mixture of metal from tires, brake wear and resuspended road dust

○S.P.I.P. Kumara
University of Kelaniya, Sri Lanka
E-Mail: kumara.spip@gmail.com

Keywords: Metal dusts, Atomic Absorbance, Spectrometry, Environmental sustainability

1. Introduction

Dust fall is one of the most complex and hazardous pollutants in the atmospheric environment [1] due to the presence of trace heavy metals. The accumulation of heavy metals in dust caused by particulate matter (PM) emitted from motor vehicles include complex mixtures of metals from tires, brakes and parts wear. Both tire treads [2] and tire [3] contain significant amounts of Zinc (Zn). Brake housing dust and crushed brake pads analyses indicate high concentrations of Iron (Fe) and Copper (Cu) [3] High levels of metals, such as Cu, lead (Pb) and Zn, in urban street dust have been reported in many countries and linked to the high motor vehicle traffic in these areas [4].

Road dust is an increasing problem in developed and developing countries and it is a source of various diseases. Heavy metals in dust can be accumulated in the fatty tissues and internal organs of the human body via direct inhalation, ingestion and dermal contact absorption [5] and pose potentially deleterious effects on human health [6] e.g. affecting the central nervous system and acting as cofactors, initiators, or promoters in other , especially for young children who were more sensitive than adults [7]. Dust derived from natural sources and anthropogenic sources can be carried by the wind into sensitive environments [8], e.g. kindergarten and elementary school. Therefore analyzing the heavy metals in the road dust and quantifying them is essential.

2. Concept

The aim of this study is to assess metals in road dust associated with motor vehicle traffic, and to determine which metals are associated with brake and tire wears and analyze the top soil and the roadside dust in urban areas which are known to be contaminated with heavy metals from atmospheric deposition. Reflux method, chemical digestion using a sonicator and microwave digester are used to digest the samples. Then the analysis is carried out using FAAS (flame atomic absorption spectroscopy).

The technique makes use of absorption spectrometry to determine the concentration of an analyte in a sample. It therefore relies heavily on the Beer-Lambert law. When the metallic salt solution is aspirated into the path of the flame, metal atoms into gaseous state are obtained. Some of the metallic atoms absorb thermal energy and get excited.However, majority of the atoms remains in the ground state. These ground state metallic atoms are absorbing radiation of their own specific wavelength. When radiation from an external source (hollow cathode lamp) emitting a spectral line that corresponds that corresponds to this characteristic wavelength, is allowed to pass through a flame containing free, unexcited atoms (Fig 1); part of that radiation is absorbed, depending on the population of the ground state the absorption of the radiation by ground state atoms follow Lamberts Beers Law.

$$A = \varepsilon * b * c$$

A $\longrightarrow$ absorbance
ε $\longrightarrow$ molar absorbtivity with units of L mol-1cm-1
b $\longrightarrow$ path length of the sample (cuvette)
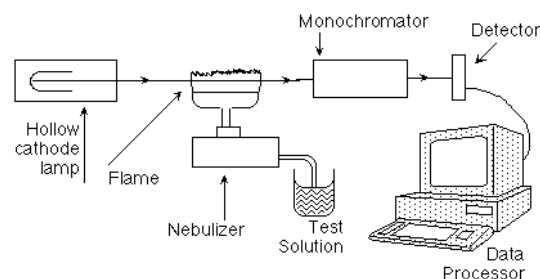C $\longrightarrow$ Concentration of the compound in solution, expressed in mol L-1

Figure 1 Experiment methodology outline

F04

3.　　Methodology

The sample was collected in urban roadside in near to the Kelaniya university, Sri Lanka. Then sample sieved by using small stainless sieve set (<2mm) (Fig 2). The sample was Oven dried 72 hours at 45 C^0.Dust (2.0g) sample Digested with con. HNO_3, HCl and H_2O for 1 hour at 95 C^0.Then Filtered　Sample Use to determine the amount of Heavy Metals (Cr,Cu,Ni,Pb) by using AAS(Atomic Absorbance Spectrometry). We use a Graph which plotted by using values of Concentration and Absorbance of stranded samples, to determine the concentration of each Metal.

Figure 2 Sieving process of the sample

4.　Results

The following tables show the experimental results obtain from this research;

Table 1 Concentration and Absorbance of Cr

Sample	Concentration	Absorbance
Sample 01	1.423	0.158
Sample 02	1.019	0.123
Sample 03	1.173	0.135
Sample 04	1.287	0.140
Sample 05	1.523	0.165
Sample 06	1.546	0.168
Sample 07	1.687	0.172
Sample 08	1.662	0.170

Table 2 Concentration and Absorbance of Cu

Sample	Concentration	Absorbance
Sample 01	4.096	0.152
Sample 02	3.968	0.147
Sample 03	3.758	0.138
Sample 04	3.652	0.131
Sample 05	4.652	0.168
Sample 06	4.068	0.146
Sample 07	4.224	0.185
Sample 08	4.158	0.172

5.　Conclusion

The proposed method successfully can be used to determine the heavy metal particles in road dust. The same process is planned to carry out in various locations including urban and rural areas.

6.　References

[1].　Joshi UM *et al.* (2009) Elemental composition of urban street dusts and their dissolution characteristics in various aqueous media. Chemosphere 77:526–533

[2].　Fauser, P *et al.* (1999. Quantification of tire-tread particles using extractable organic zinc as tracer. Rubber Chemical Technology 72, 969-977

[3].　Adachia, K., Tainoshob, Y., 2004. Characterization of heavy metal particles embedded in tire dust. Environment International 30, 1009-1017.

[4].　Culbard, E.B *et al.*1988. Metal contamination in British urban dusts and soils. Journal of Environmental Quality 17, 226-234

[5].　Lu X et al. (2009a) Contamination assessment of mercury and arsenic in roadwaydust from Baoji, China. Atmos Environ 43:2489–2496.

[6].　Faiz Y et al. (2009) Road dust pollution of Cd, Cu, Ni, Pb and Zn along Islamabad Expressway, Pakistan. Microchem J 92:186–192

[7].　Kong S, Lu B, Ji Y, Zhao X, Chen L, Li Z, Han B, Bai Z (2011) Levels, risk assessment and sources of PM10 fraction heavy metals in four types dust from types dust from a coal-based city. Microchem J 98:280–290

[8].　Meza-Figueroa D, De la O-Villanueva M, De la Parra ML (2007)Heavy metal distribution in dust from elementary schools in Hermosillo, Sonora, Me´xico. Atmos Environ 41:276–288

P01

Mobile Radiation Monitoring with GPS Module

○Nguyen Cao Thang, Nalin Warnajith, Atsushi Minato
Institute of Applied Beam Science,Ibaraki University, Japan
E-Mail: thangtict88@yahoo.com, nwarnajith@gmail.com, minato@mx.ibaraki.ac.jp
Keywords: Dose Meter, GPS, RaspberryPi, XBee, Google Map

1. Introduction

After the Fukushima Daiichi nuclear accident in 2011, measuring the radiation concentration has become an important issue in environmental sustainability. The concentration of the radiation is higher than normal in a wide range not only Fukushima area, but also in the east part of Japan. This research proposes a measuring method and portable measuring device that can record the radiation location, time and mapping them.

.

2. Methodology of the system

Developed system consists of a wireless communication device XBEE, GPS sensors, a small computer Raspberry Pi and radiation measuring instrument. The goal of this study is to measure radiation dose reading and location information from a remote location by using wireless communication methods. Also the retrieved information can be mapped or graphed using these readings along with the GPS information. The power consumption of this proposed whole system is very low, therefore the system is capable long term measuring.

Raspberry Pi is a small personal computer with low power consumption. Also, Raspberry Pi is one-tenth the price of a normal PC inexpensive. Also, it can be measured by automatically at the startup of the Raspberry Pi and from this feature the video display unit (monitor) can be removed from the system which consumes a lot of power supply.

Dose meter TA100 of Techno AP was used for measurement. This device can be controlled by USB serial Interface

The proposed system configured in two methods according to the intended use. The first one consists a GPS sensor and Raspberry Pi (Fig 1) and the next is with wireless configuration via XBEE (Fig 2).
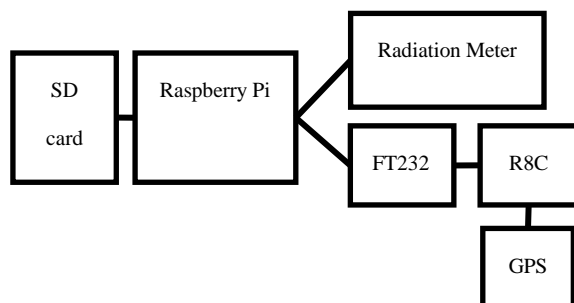

Fig. 1. Concept of the system with GPS sensor and Raspberry Pi
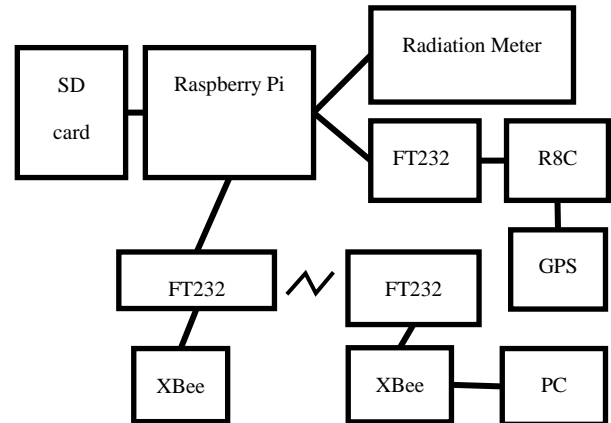

Fig. 2. Concept of the system with Xbee

Fig. 3. Developed system

The R8C microcontroller unit works as the intermediate interface between GPS sensor and the Raspberry Pi. It converts signals that receive from GPS sensor into the serial communication UART system.

Raspberry Pi (Linux board) works as the main hub of this system. GPS and radiation measurements are requested by Raspberry Pi through a Python programming interface from the sensors. The flow chart of the Python program is shown in figure 4. The obtained information can be viewed via XBEE in the wireless configuration.

3. Experimental data

To create a map as shown in the figure at the google map data that has been acquired. Where map at a glance what dose intuition.

Also, it is possible to manage the dose of each time using the wireless communication.

P01

Xbee is a short-range wireless communication device. We have demonstrated up to 550m and it can communicate in the experiment.
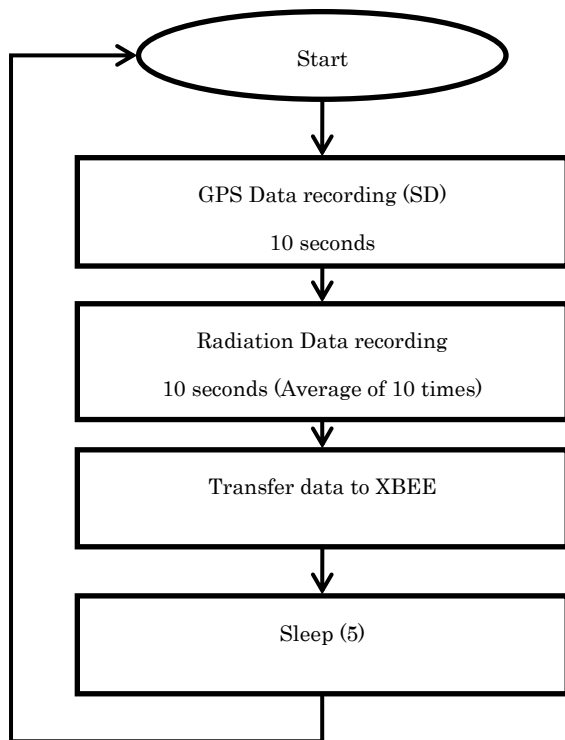

Fig. 4. Flowchart of Program
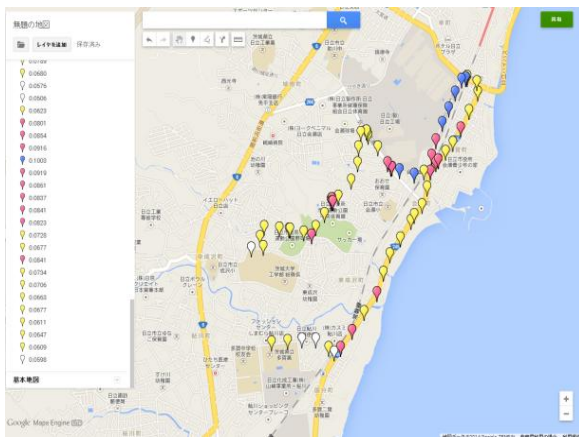

Fig. 5. Mapping by Google Map

4. Conclusion

This research made a device that can be measured in radiation data and GPS data through wireless using the Raspberry Pi. In future, We want to use this device to measure the data actually useful.

P02

Synthesis of Gd-DTPA immobilized SiO$_2$ Nanoparticles and Their Imaging Ability

○Yuta Shindo, Yoshio Kobayashi
Collage of Engineering, Ibaraki University
E-Mail: 14nm5151f@vc.ibaraki.ac.jp

Keywords: Gd-DTPA , nanoparticle , silica , imaging

1. Introduction

Complex compounds of gadolinium (Gd) ions have been commonly used as a contrast agent for magnetic resonance imaging (MRI) because of their excellent paramagnetic properties [1]. The Gd has the ability to absorb X-ray due to its large atomic number [2]. Accordingly, the Gd is available as a contrast agent for not only MRI but also X-ray computed tomography (CT). Gd-diethylene triamine pentaacetic acid (Gd-DTPA), which is a typical, commercial Gd-based contrast agent, is an aqueous solution of Gd complex molecules. The Gd-DTPA molecules have a short residence time in blood tube because of their small size in molecular order, which provides difficulty realizing steady imaging of focal sites. Immobilization of Gd-DTPA on nanoparticle substrate is promising to solve the problem. Nanoparticles are larger than molecules, and receive remarkable fluid resistance in blood. Consequently, their residence time increases, which improves the ability for contrast agents. The present study attempts to immobilize Gd-DTPA on SiO$_2$ particles that are colloidally stable and inert to living bodies.

2. Experimental

2.1. Preparation of SiO$_2$ particles and surface modification of them

Colloid solutions of SiO$_2$ particles were prepared by reacting tetraethoxysilane and H$_2$O in EtOH solution containing NaOH aq. for 24 h. After centrifuging the SiO$_2$ particle colloid solution and replacing the solvent with water, the SiO$_2$ particles were surface-modified with amino-groups (amination). A chemical used for the amination was (3-aminopropyl)triethoxysilane. The reaction time was 24 h (SiO$_2$-NH$_2$).

2.2. Immobilization of Gd-DTPA

Gd-DTPA used was Magnevist (Bayer, YJ code: 7290405A4031). Immobilization of Gd-DTPA on particles was performed by mixing the SiO$_2$-NH$_2$ particles and Gd-DTPA. The pH of the solution during the immobilization was adjusted to 3 by adding HCl aq. The reaction time was 24 h (SiO$_2$-Gd-DTPA).

2.3. Characterization

The obtained particles were observed with transmission electron microscope (TEM). Properties of particle surface were investigated by electrophoretic-light-scattering (ELS) and X-ray photoelectron spectroscopy (XPS). Their imaging ability was studied by an MRI instrument and a CT instrument by using laboratory animals.

3. Results and Discussion

3.1. Morphology of particles

TEM observation revealed production of spherical SiO$_2$ particles with a size of 101.1±12.3 nm. Such morphology did not change even after the Gd-DTPA immobilization, which indicated no damage to SiO$_2$ particles even with the pH adjustment.

3.2. Surface-modification

The ELS revealed that the SiO$_2$ particles had an iso-electric point (IEP) of ca. 3.0, which corresponded to that reported in the previous work [3]. For efficient immobilization of anionic Gd-DTPA on the anionic particle surface, the amination was performed for the SiO$_2$ particle surface. After the amination, the IEP shifted to 5.6, which indicated successful amination. N element was detected on the SiO$_2$-NH$_2$ particle surface by XPS, which supported the presence of amino groups on particle surface. After immobilization of Gd-DTPA, the IEPs were 5.6 and 4.0 for the solutions with no and with pH adjustment, respectively. The IEP for the pH adjustment was lower than that of SiO$_2$-NH$_2$ particles, which indicated that the pH adjustment was useful for efficient immobilization of Gd-DTPA on particle surface. The pH adjustment decreased the value of negative charge on particle surface, which made the Gd-DTPA molecules approach the particle surface easily [4].

3.3. Imaging ability

MRI imaging ability is evaluated with r1 value. The r1 values were ca. 0 and 1.0 mM^{-1}/s for SiO$_2$ and SiO$_2$-Gd-DTPA particle colloid solutions, respectively. Their CT values were 66 and 187 HU, respectively. The Gd-DTPA immobilized particle colloid solution had both abilities for MRI and CT imaging superior to the SiO$_2$ particle colloid solution.

4. Conclusion

In this work, fabrications of various particles such as the SiO$_2$, SiO$_2$-NH$_2$ and SiO$_2$-Gd-DTPA were performed. Each morphology of particles was spherical and monodisperse. The SiO$_2$-Gd-DTPA particle colloid solution exerted the MRI and CT abilities. Accordingly, it is expected to be used as a new MRI and CT contrast agent with a long residence time in living bodies.

References

[1]. Montri Ratanajanchai *et al*. (2014). "Photo-cured PMMA/PEI core/shell nanoparticles surface-modified with Gd-DTPA for T1 MR imaging" *J. Colloid Interface Sci. 415*, pp. 70-76.

[2]. Ji-Ae Park *et al*. (2010). "Gold nanoparticles functionalized by gadolinium-DTPA conjugate of cysteine as a multimodal bioimaging agent" *Bioorg Med Chem Let. 20* , pp. 2287-2291.

[3]. Marcell Palmai *et al*. (2013). "Preparation, purification, and characterization of aminopropyl-functionalized silica sol" *J. Colloid Interface Sci. 390*, pp. 34-40.

[4]. Hang-Deok Oh *et al*. (2013). "Facile synthesis of QD-anchored composite particles with magnetic cluster cores" *Mater Res Bull. 48*, pp. 2191-2195.

P03

Fabrication of Alumina Thin Films Crystallized at Low Temperature

○Katsumi Yamamura, Yoshio Kobayashi
Collage of Engineering, Ibaraki University
E-Mail: 14nm519y@vc.ibaraki.ac.jp
Keywords: Alumina, Crystallization, Film, Low temperature, Seeding, Hydrothermal

1. Introduction

Thin films have penetrated deeply into our daily life as materials that are required to compose various electronic devices like semiconductor device. Alumina, which is a representative material for thin film, has excellent thermal conductivity and electrical insulation, so that it can be applied to an integrated circuit [1]. There are various crystal structures in the alumina. Among the crystal structures, a crystal structure of alumina that has the excellent properties is α-type. Because the alumina is crystallized to α-type by annealing at high temperature (1100°C), selection of substrates is limited for production of α-alumina films. Recent years, researches on low-temperature crystallization to α-alumina have been intensively performed [2-3].

The present work proposes a method for preparing alumina sol from aluminum salt by utilizing a homogeneous precipitation method. Effects of hydrothermal treatment and seeding of crystallites on crystallinity of alumina were investigated for lowering its crystallization temperature. Fabrication of alumina films was also performed.

2. Experimental

2.1. Fabrication of alumina films

Alumina sol was prepared with the same method as performed in our previous work [4]. Precipitate of aluminum hydroxide was prepared by the homogeneous precipitation method, or by the following procedure. Al(NO$_3$)$_3$ and urea were dissolved in water in a glass bottle. The mixture was stirred at 80°C for 8 h, which produced white precipitate. The obtained precipitate was washed by repeating centrifugation, removal of supernatant, addition of the water and sonication over three times, and then peptized at 25°C (room temperature) with the addition of acetic acid. The precipitate was transformed to the alumina sol after the peptization. Alumina films were fabricated by dip-coating the alumina sol on sodium glass substrates and then drying it for gelation.

2.2. Hydrothermal treatment of alumina sol

The hydrothermal treatment was carried out in an autoclave. The autoclave containing the alumina sol was sealed tightly and heated in dry oven. Once the temperature reached 100°C, the temperature was kept for 1 h.

2.3. Preparation of alumina gel seeded with α-Al$_2$O$_3$ particles

Commercially-available α-Al$_2$O$_3$ particles were dispersed in the alumina sol after the hydrothermal treatment. The sol was casted onto a petri dish. Drying in air at room temperature converted the sol into solid alumina gel. The solid gel was pulverized with a mortar into powder, and then annealed in air at various temperatures of 500-900°C.

2.4. Characterization

Crystal structures of the alumina gel were characterized by X-ray diffractometry (XRD). A section of the alumina thin film was observed with scanning electron microscope (SEM).

3. Results and discussion

3.1. Alumina gel

The precipitates composed of fine Al(OH)$_3$ particles, which were produced with the homogeneous precipitation method, formed alumina sol transparent in visible region with the peptization. An alumina gel obtained by drying the sol was amorphous. The alumina was crystalized to γ-alumina by annealing at 900°C, and not to α-alumina. The gel produced from the hydrothermal treated sol was transformed to α-alumina by annealing at 900°C. The presence of fine and uniform crystalline particles, which were produced in the solution during the hydrothermal treatment, probably promoted the crystallization. The seeded alumina gel was transformed to α-alumina at 700°C. Surface of the seed crystallites was considered to function as staring points for crystallization of alumina. Transformation to α-alumina usually requires annealing at ca. 1100°C. In contrast, the α-alumina was produced at the temperature as low as 700°C in the present work, which was 400°C lower than the conventional crystallization temperature of 1100°C.

3.2. Alumina film

According to the SEM observation, the alumina film was successfully fabricated. A thickness of the film was ca. 300 nm.

4. Conclusion

The alumina gel treated with hydrothermal treatment and seeding of crystallites was crystallized by annealing at the temperature lower than that for the non-treated alumina gel. The alumina thin film was successfully fabricated by the dip-coating technique. Accordingly, thin films of the alumina fabricated by the processes of hydrothermal treatment and seeding are expected to be used as electrically-insulated materials.

References

[1]. L. Juhász *et al.* (2009). "Humidity sensor structures with thin film porous alumina for on-chip integration" *Thin Solid Films. 517*, pp. 6198-6201.

[2]. W. Wang *et al.* (2009). "Low-temperature synthesis of BaTiO$_3$ powders by the sol–gel-hydrothermal method" *Ceram. Int. 50,* pp. 276-282.

[3]. T. Yamaguchi *et al.* (2011). " Low-temperature formation of α-alumina from various polyhydroxoaluminum -hydroxy acid composite gels" *Ceram. Int. 37,* pp. 201-216.

[4]. K. Inoue *et al.* (2013). " Fabrication of transparent self-supporting alumina films by homogeneous precipitation process" *J. Ceram. Soc. Japan. 121*, pp. 494-497.

Development of techniques for fabricating of platinum-Immobilized titania particles by electroless plating process

○Masataka Sakai, Yoshio Kobayashi
Collage of Engineering, Ibaraki University
E-Mail: 14nm509h@vc.ibaraki.ac.jp
Keywords: platinun , nanoparticle ,electroless plating process

1. Introduction

Platinum (Pt) nanoparticles function as catalyst in fuel cell electrode and catalyst cleaning exhaust gas produced from automobile because of its excellent catalytic performance. Since Pt is one of the rarest metals in rare metal, its amount used is desired to be reduced. And so, Pt nanoparticles are expected to increase their catalytic activity and decrease amount of Pt. Nanoparticles tend to aggregate, which deteriorates their unique propaties derived from the size effect. Immobilizing of nanoparticles on supports such as plates and particle is a candidate to prevent the aggregate. The present work draw on method of forming a metal thin film on the insulating material, that electroless metal plating technique [1-3], and develop technique for producing Pt nanoparticles-immobilized support of TiO_2 nanoparticles. This method was combined with the electroless metal plating technique to develop a method for fabricating Pt-coated particle.

2. Experimental

2.1. Preparation of TiO_2

TiO_2 particles were prepared by a sol-gel process. Titanium tetraisopropoxide (TTIP) (TiO_2 soruce) dissolved in 2-propanol (2-PrOH) was added to a mixture of water (Initiator), CH_3CN (base catalyst), and CH_3NH_2/2-PrOH. Then the resultant particles were annealed at 100℃ and 300℃.

2.2. Pt-Immobilization of TiO_2 nanoparticles

Pt-Immobilization of TiO_2 nanoparticles were prepared by a electroless metal plating technique. The annealed TiO_2 particles were surface-modified with polyvinylpyrrolidone (PVP). Then sensitization and activation of TiO2 particles surface were performed to add an Sn solution and an Pd solution in turn , respectively. Pt nano particles supports on TiO_2 particle surface to order of addition H_2PtCl_6 and hydrazine hydrate.

2.3. Fabrication of Pt-coated particle

This method was combined with the electroless metal plating technique to develop a method for fabricating Pt-coated particles.

2.4. Characterization

The obtained particles were observed with transmission electron microscope (TEM). In order to analyze structural characteristics, X-ray diffraction (XRD) and X-ray photoelectron spectroscopy (XPS) were used.

3. Results and Discussion

3.1. Annealing TiO_2 particle

According to XRD of approach similar to TiO_2, annealing transformed the crystalline phase of TiO2 to amorphous (100℃) and anatase (300℃). And TEM observation, the TiO_2 particles were sintered and grown by heat-treatment.

3.2. Pt-Immobilization of TiO_2 nanoparticles

According to TEM observation, the TiO_2 particles were spherical and supported Pt. For 100℃ and 300℃ annealing, the particle size were 196±82 and 190±51 nm, respectively. Pt was supported more 100℃ than 300℃ annealing. This indicated that hydroxyl groups were remained on the TiO_2 particles surface. Therefore, each metal ions of adsorbed amount was increased.

3.3. Fabrication of Pt-coated particle

TEM observation revealed that the amount of Pt immobilized on the particles increased with the Pt-coating process compared to the Pt-immobilized particles. Pt was considered to be immobilized on the Pt particle surface on the Pt-immobilized particles by an autocatalytic reaction in the electroless plating method.

4. Conclusion

The present work performed the preparation of Pt-supported particles by electroless metal plating method. Pt shell thickness was increased to repeat several times electroless plating process. Pt-supported particles possessing a small particle size, acid resistance, heat resistance and catalytic activity are required to be studied to realize fuel cell electrode.

References

[1]. Yoshio Kobayashi *et al.* (2014). "Fabrication of TiO2/Pt core–shell particles by electroless metal plating" *Colloids and Surfaces A: Physicochemical and Engineering Aspects 448*, pp. 88-92.

[2]. M.L. Bosko *et al.* (2013). "Controlled Pd deposition on fibers by electroless plating. The effects of the support on the reduction of nitrite in water" catalysis Today 212, 16-22.

[3]. G. Mondin *et al.* (2013). "Metal deposition by electroless plating on polydopamine functionalized micro- and nanoparticles" *Journal of Colloid and Interface Science 411,* pp.187-193.

Water color monitoring system using Bluetooth

Jia Zhenzhen[*],   S.H.P.K.Lakesh,   Atsushi Minato

E-mail:13nm021t@hcs.ibaraki.ac.jp

Key word: *Low cost, LED, phototransistor, water color, water environment.*

1．Introduction

Currently, the world faces unprecedented challenges in water environmental monitoring. Therefore, the target is to collect and analyze water environment data in order to avoid any water pollution risk. In that case, water color is essential parameter to evaluate turbidity or phytoplankton. Commercially available water monitoring system is big in size as well as very expensive. Therefore, we developed a simple and inexpensive instrument for water color monitoring.

2. Content of research

2.1 Experimental Design
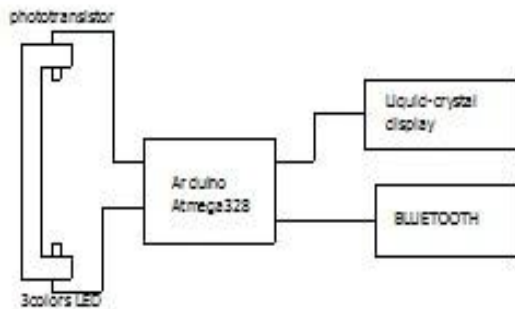
Figure.1 Water color monitoring system .

In this study, we used the Arduino (Atmega 328), three color LED (Red, Blue and Green), phototransistor and liquid crystal (LCD). Here we fixed the phototransistor and three color LED beside the plastic tube and keep the 20cm distance between LED and Phototransistor. The Bluetooth device is also connected to microcomputer. Figure.1 shows the system design.

Three color LED illuminates in short time. The voltage of phototransistor corresponds to the intensity of three color lights. These values depend on the absorption between the LED and the phototransistor. In addition, it is capable of sending data to the PC or wireless Tablets via Bluetooth communication.
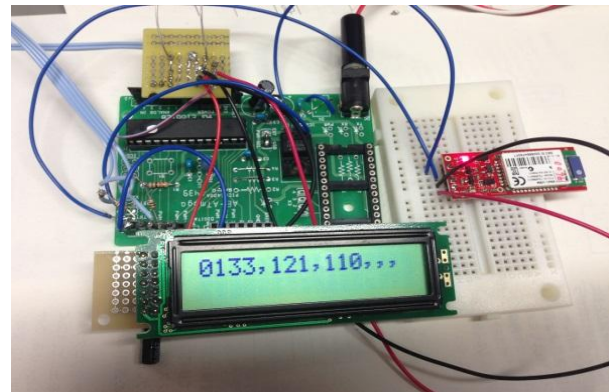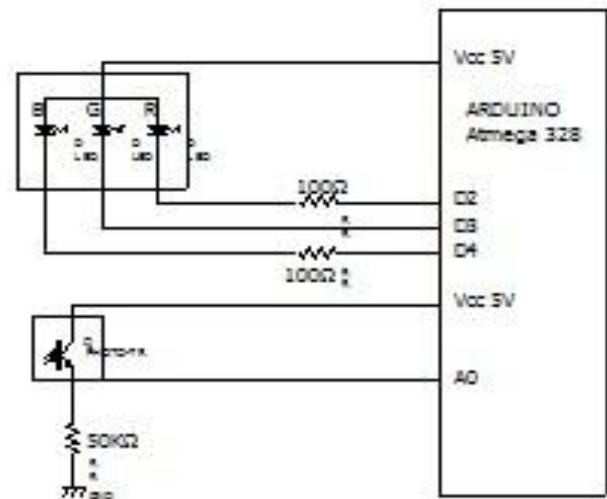

Figure.2 Test Circuit device

Fidure.3 Phototransistor measuring device circuit

3. Experiment Result

Colored liquids (L1, L2 and L3) were prepared for the fundamental test. L1, L2 and L3 are Blue, Green and Red waters. The absorption of these liquids measured by spectrometer (SP-300) is shown in Fig. 4. The RGB values measured by developed system is also shown in the figure.
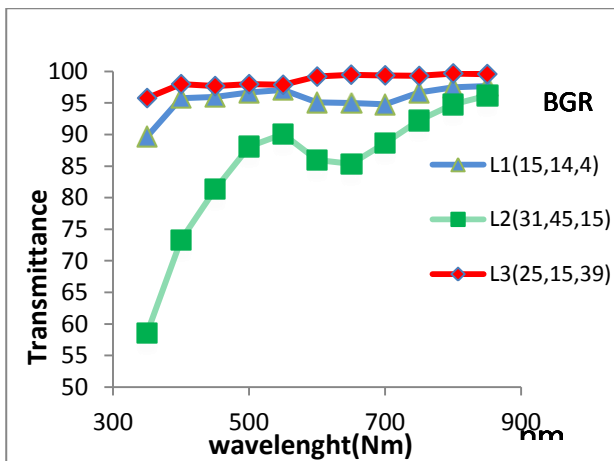
Figure.4   Absorption spectrum of test liquids (Red, Green and Blue) data.

4. Conclusion

The proposed color monitoring system can be applied to the measurement of turbidity and phytoplankton in the water environment. In addition, we are planning to conduct monitoring actual water environment in the next experiment stage.

5. Reference

[1].StacyA.C.NELSON*,Patricia.SORANNO,Kendra Spence CHERUVELIL,SamA.BATZLI & David L.SKOLE（2013）. Regional assessment of lake water clarity using satellite remote sensing. Bolsena Conference(2002).   Timein lakes   :Science,Management,Education J.Limnol.,62(suppl.1):27-32,2003.

[2].Atmel Corporation   Atmega328   Date sheet(2010)＜ http://akizukidenshi.com/download/mcu/avr/atmega4 8-88-168-328_A_P_PA.pdf＞(10.8.2014).

Investigation of the diffusion behavior of hydrogen in a ferritic steel by means of hydrogen microprint technique

○**Sugawara Atsushi* and Itoh Goroh****

*Graduate Student, Graduate school of Science and Enginnering, Ibaraki University,
**Department of Mechanical Engineering, Ibaraki University
E-Mail: *13nm424f@hcs.ibaraki.ac.jp, **gitoh@mx.ibaraki.ac.jp

Keywords:feritic steel, hydrogen microprint technique, stress, hydrogen embrittlement, cathodic electrolytic charging, hydrogen diffusion, hydrogen invasion, hydrogen emission,

1. Introduction

The use of hydrogen energy is demanded to solve the problem of the global warming, but a phenomenon called hydrogen embrittlement must be taken into account when we use hydrogen. Hydrogen embrittlement causes a drop of strength and elongation of metallic materials arising from invasion of hydrogen. This phenomenon is easy to occur in high-strength materials. Therefore, in the case of use of high-strength steel, elucidation of the hydrogen embrittlement mechanism is very important. However, the mechanism of the embrittlement and the behavior of hydrogen in steels have not been clarified yet.

Hydrogen in metals is classified into two types introduced in the material either during the service or in the course of production process. The former type is referred to as environmental hydrogen and acts a major role in the hydrogen embrittlement.

In this study, the behavior of hydrogen in a stress-loaded SPFC (Steel Plate Formability Cold) steels was investigated in stress loading by mean of the hydrogen microprint technique (HMPT).

2. Specimens and Procedure
2.1. Cathodic electrolytic charging

The principle of cathodic electrolytic charging is schematically shown in Fig.1. The metal specimen and a platinum foil are placed in the cathode and anode, respectively. The following reactions (1) and (2), i.e., electrolysis reactions of water, occur concurrently.

Anode(+) : $4OH^-{\rightarrow}2H_2O+O_2+4e^-$
Cathode(-) : $4H^++4e^-{\rightarrow}2H_2$ $\qquad$ (1)

If hydrogen recombination poison such as NH_4SCN is added to the electrolysis solution, a recombination reaction at the cathode can be inhibited and some of hydrogen can invasion the metal in the atomic state.
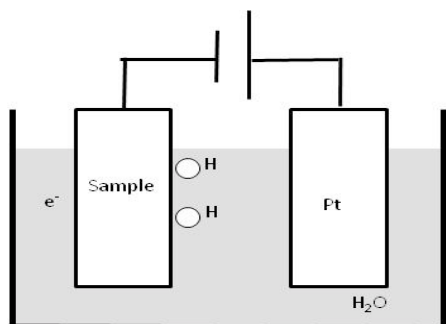

Fig.1. Schematic for cathodic electrolytic charging technique.

2.2. Principle HMPT

The HMPT is a way to visualize the hydrogen emitted from a metallic material using photographic emulsion. Fig.2 shows the schematic diagram of the principle of HMPT. First, the surface of the specimen is covered with photographic emulsion by the wire loop method. Then, when hydrogen atoms with strong reducing power are emitted from the interior of the specimen, silver bromide contained in the emulsion changes into metallic silver.

$$Ag^+ + H \rightarrow Ag + H^+ \qquad (3)$$

Here, unreacted silver bromide is dissolved and removed by the fixing treatment. On the other hand, metallic silver produced is retained in the gelatin layer of the emulsion, so that position of the hydrogen emission is the position of the metallic silver. After rising and drying, the location of the hydrogen emission can be observed together with the microstructure of the specimen using a scanning electron microscope (SEM).

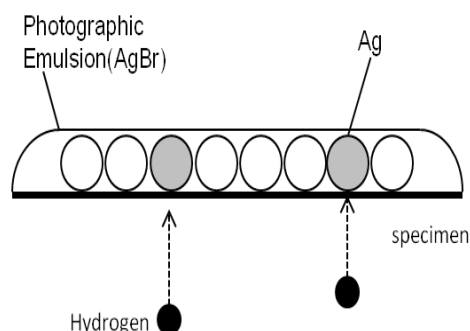The amount of emitted hydrogen can be assessed from the amount of metallic silver.

Fig.2. Principle of hydrogen microprint technique (HMPT).

2.3. Specimens

The specimen used in this study is a 1.0mm thick sheet of SPFC steel. Table 1 shows its chemical composition. Samples of 50mm×10mm were cut from the sheets, wet-ground with #2000 abrasive paper, and then mirror-finished with alumina and silica particles. To investigate the effect of the stress loading, we compared the sample which gave 20% of tensile deformation and didn't give.

Table 1. Compositions of the specimen in mass%.

C	Si	Mn	P	S
0.15	0.02	0.97	0.013	0.004

2.3. Experimental Procedures

To investigate the effect of stress loading as well as cathodic hydrogen charging, four kinds of specimens were prepared: (A) without electrolytic hydrogen charging without stress loading, (B) without electrolytic hydrogen charging with stress loading, (C) with electrolytic hydrogen charging without stress loading,

(D) with electrolytic hydrogen charging with stress loading.

The cathodic electrolytic charging was performed from one side of the sample. In a sulfuric acid aqueous solution pH=2.5 with 0.1mass% NH4SCH at a current density and voltage of 10mA/cm^2 10V, respectively for 30min at room temperature. After the sample was rinsed with water and then acetone, either the same or the opposite side of the sample was covered with the photographic emulsion (Ilford Scientific Product diluted to 4 times with distilled water) by the wire loop method. The sample with the emulsion layer was dried, held at 24h in a darkroom to allow the hydrogen to be emitted, fixed in an aqua solution with 15% of sodium thiosulfate for 15min, immersed in an aqua solution with 10% of sodium nitrite for 30 minutes dried naturally, and finally observed with an SEM together with energy dispersive X-ray spectroscopic (EDXS) analysis to confirm whether the particle observed was silver.

3. Results and Discussion

An example of HMPT/SEM images of the SPFC steel is shown in Fig. 3 where observation was made on the hydrogen-charged side. Hydrogen is not detected in the sample without hydrogen charging, Figs. 3 (A) and (B), which means that there is no effect of the hydrogen introduced during the production process of material. In contrast, hydrogen is detected in the samples with hydrogen charging, Figs. 3 (C) and (D).In the sample with hydrogen charging without stress loading, Fig. 3 (C), the silver particles exist inside the grain, grain boundary and pearlite, while in the sample both with hydrogen charging and stress loading, Fig.3 (D), major portion of silver particles are on the grain boundary with minor portion on the slip line. Thus, grain boundary, slip line and pearlite were the diffusion paths for hydrogen. Although the applied stress in the present study is under the yield stress, local plastic deformation is known to occur resulting in the dislocation motion forming the slip line.

In the sample both with hydrogen charging and stress loading, hydrogen charging time was decreased to 10min. The resultant HMPT/SEM images are shown in Fig. 4. Silver particles on the grain boundary especially at the triple points are still observed, while there is no particle on the slip line.

To investigate the diffusion behavior of hydrogen more in detail, permeation side (the other side than the hydrogen-charged side) was observed. An example of resultant HMPT/SEM images is shown in Fig. 5. Hydrogen is detected only from the grain boundary in the sample without stress loading. On the other hand, hydrogen is also detected inside the grain especially on the slip line. The latter type of hydrogen can be attributed to the transport of hydrogen by the moving dislocations, inside the grains.
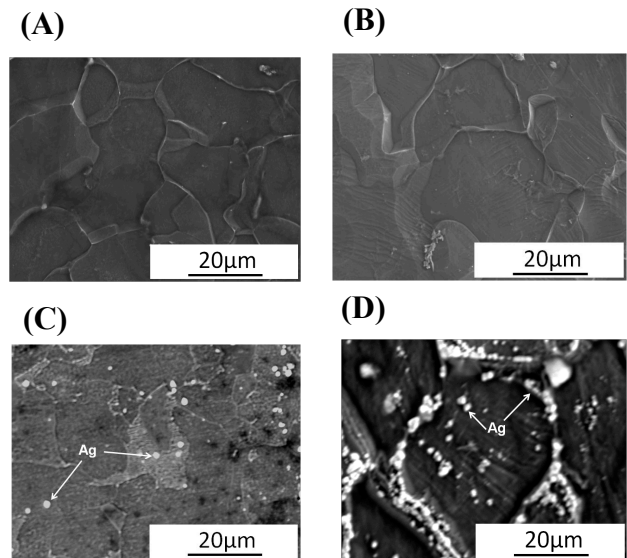

Fig. 3. HMPT/SEM images of the SPFC samples
(A) without hydrogen charging without stress loading,
(B) without hydrogen charging with stress loading,
(C) with 30min hydrogen charging without stress loading,
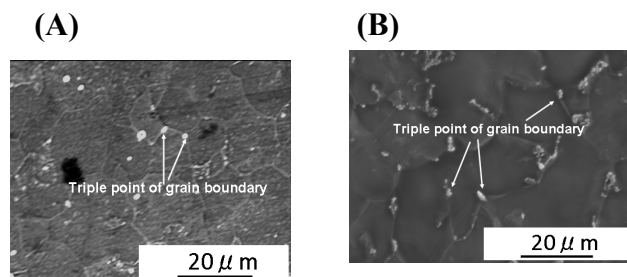(D) with 30min hydrogen charging with stress loading.

Fig. 4. HMPT/SEM images of the SPFC samples hydrogen-charged for 10min.
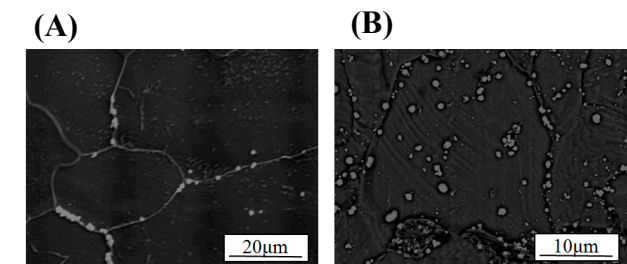(A) without stress loading,
(B) with stress loading.

Fig. 5. HMPT/SEM images on the permeation side without(A) and with(B) stress loading.

4. Conclusion

The behavior of hydrogen in SPFC steel was investigated, and the following results were obtained.
1. Grain boundary, slip line and pearlite were the paths where hydrogen is easy to diffuse.
2. Diffusivity can be thought to be largest along the triple point of grain boundary and next along grain boundary.
3. It is considered that hydrogen detected inside the grain especially along the slip line is transported by the dislocations.

Inclination measurement using camera and bubble tube

Gu Zhenghe[1] , Anne Nisha and Atsushi Minato[1]
[1]Department of Science and Engineering, Ibaraki University
(4-12-1, Nakanarusawa, Hitachi, 316-8511, Japan)
E-Mail: [1]13nm023g@vc.ibaraki.ac.jp
Keywords: R8c, bubble tube, Bluetooth, Microcontroller

1. Abstract

Monitoring of inclination of land is important to prevent damage from landslide. Low cost and stable system is necessary for this purpose. This paper presents a new inclination measurement system and its application to sensor network of disaster prevention. This system has a cylindrical bubble tube and a USB web camera. The angle and direction of inclination is measured from the photo of bubble tube with radius of curvature 20000mm. A GNL18/M model THORLABS goniometer was used to record the inclination.

2. Introduction

According to the report of the Ministry of Land, Infrastructure and Transport, during the 10 years period (2013-2012), average number of natural disasters like earthquakes, torrential rain, snow melting, and typhoons, landslides, and landslides amount to 1180 cases in Japan. It was also revealed that the number of deaths and people missing by such accidents are about 30 people every year.

Landslides cause extensive property damage, injury, death and adversely affect a variety of resources like water supplies, fisheries, sewage disposal systems, forests, dams and roadways. Recently, the Kedarnath land slide on 16 June 2013 caused the death of 5,700 people in India.

Landslide hazard monitoring and analysis can provide useful information for catastrophic loss reduction and assist in the development of guidelines for sustainable land use planning

In order to minimize the damage caused by landslides, monitoring measures in advance and rapid response after the earthquake is essential. Development of the inexpensive and reliable equipment has become a major social requirement.

3. System description and Principle of measurement

This system has a JPEG camera, Renesas R8C microcontroller (M11A), a calibrated cylindrical bubble tube with 20000mm radius of curvature and a wireless module for real time monitoring.
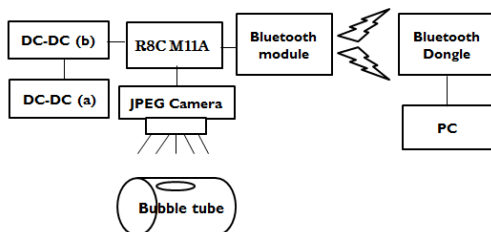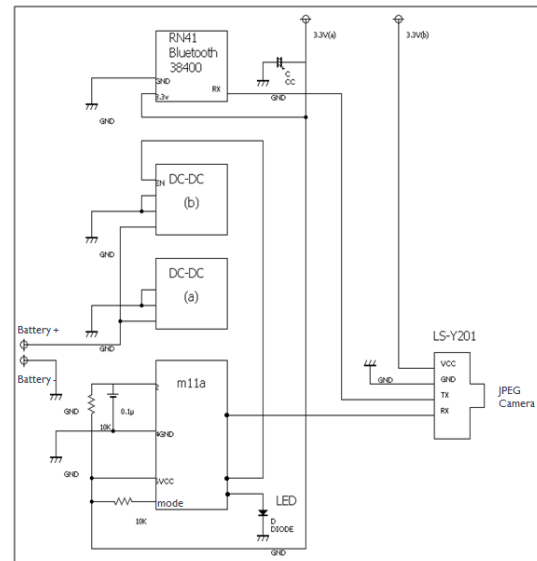

Fig. 1. Experimental setup

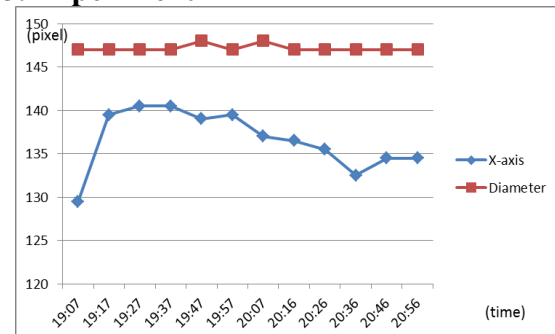**Fig. 2. Circuit of experimental system**

3. Experiment

Fig. 3.Example of measured data

Figure 3 shows an example of measured data. The microcontroller takes photo every 10 min and JPEG data is sent via Bluetooth to a windows PC. A processing program on the PC stores data as JPEG file. The movement of bubble and the diameter are shown in Fig. 3.

4. conclusion

Test system for inclination monitoring using bubble tube was developed. The system works using wireless communication. Class 1 Bluetooth module was used. The range of communication is 100m in the open air.

References

[1]. Sasahara Katsuo, Tamura Keiji (2010) "Simulation model of surface displacement of steep slope made of granite soil under middle scale rainfall", Journal of the Japan Landslide Society : Landslides 47(3), 155-160.

[2]. Mo Yang, Masanori Itaba, Atsushi Minato, Satoru Ozawa (2013) "Development of perpendicular sensor and Its Application for Raging", ISCIU6, 75-76.

Development of Efficient Algorithm for Ion-Mobility Spectrometry

○Ryodai Suzuki*, Masaru Kamada*
*Department if Computer and Information sciences Ibaraki University
E-Mail: *14nm711g@ vc.ibaraki.ac.jp
Keywords: sparse approximation, efficient algorithm, Matching pursuit

Abstract—Employing discrete B-splines instead of the Gaussian distribution, we construct an algorithm for the analysis of ion-mobility spectrometry profiles. The algorithm is suitable for hardware implementation because the discrete B-splines are supported by a simple digital filter to compute their weighted sum and their correlations with a given signal. Minutely shifted discrete B-splines are deployed of which weighted sum is to approximate a given profile with non-negative weights. Closely neighboring discrete B-splines are almost linearly dependent so that they may cause numerical instability in the approximation process. But numerical experiments deny this anxiety at least for the final results. Varying the width of discrete B-splines, we obtain a number of different approximations. Out of sufficiently precise approximations, we choose the sparse one in the sense that it comprises few discrete B-splines with large weights.

1. INTRODUCTION

Ion-mobility spectrometry [1] is a method of discriminating chemical molecules in the atmosphere. Its capability of identifying tiny amounts of various chemicals has made it possible to analyze odor and flavor and to detect poisons, drugs and explosives. The analysis is mainly composed of physical and computational processes.

The physical process proceeds in this way: (i) Chemical molecules are ionized and injected near the cathode as shown in Fig.1 (a). (ii) The ions move toward the anode with the acceleration proportional to their charge-mass-ratio as illustrated in Fig. 1(b). Light ions reach the anode earlier than the heavier ones on the average. The ions bump and bounce against air and other molecules during their travel so that even ions of the same kind arrive at the anode in different traveling times. (iii) The ions give their charges to the anode which constitute the electric current called profile like the curve in Fig. 2(a). The profile is modeled as a weighted sum of several distributions as schematized in Fig. 2(b). Each distribution is traditionally supposed to be Gaussian because any random displacements of ions by their collision with other molecules amount to a Gaussian distribution if they happen infinitely many times.

The computational process identifies each different distribution in a given profile. Its weight and average tell, respectively, how much and what kind of ions are present. The standard algorithm employs the steepest descent method to search for locally optimal values of unknown parameters such as average, variance and weight of an unknown number of Gaussian distributions. This search has to be conducted sequentially so that it consumes much time even on the latest fast CPUs.

While a tiny chip from Owlstone Nanotech [2] and a system solution from ATONARP [3] have already made it possible to complete the physical process in a few milliseconds, the computational algorithm is still sequentially searching for local optima at much computational cost. In this paper, we shall approach a

new algorithm which matches up to the compact and fast physical system. This approach is characterized by the following four features:

(i) Instead of the Gaussian distribution, we use the B-spline [4] of order m that is defined as the m-fold convolution integral of a uniform distribution and represents the distribution of ion position after m collisions if one causes a uniformly random displacement. The B-spline is a good substitute since it tends to the Gaussian at the limit $m \to \infty$. We can even say that the Gaussian was not the perfect choice because it has infinitely long tails that never exist in reality. We had better take a large m but do not have to make it infinity.

(ii) For the sake of simpler computation, the B-splines are further replaced by their discrete version1 defined as the *m* fold discrete convolution of the uniform discrete distribution. The discrete B-splines can be generated by only additions and subtractions [6]. There is also a fast digital filter to compute their correlations with a given signal [7].
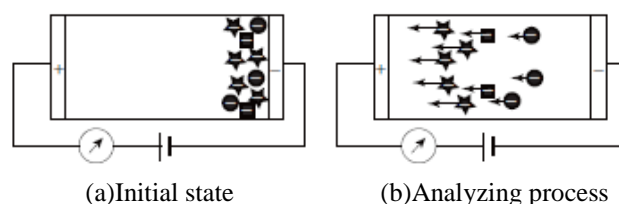

(a)Initial state   (b)Analyzing process
Fig.1 Schematics of the ion-mobility spectrometry

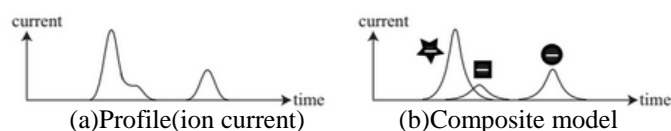(a)Profile(ion current)   (b)Composite model
Fig.2 Ion-mobility spectrometry profile

(iii) We dare to deploy the discrete B-splines shifted by a minute interval as analyzing components of which weighted sum is to approximate a given profile even though we risk numerical instability in the approximation process due to the almost linear dependency among the overcrowding components. Otherwise, the algorithm would fall back to the slow sequential search for an unknown number of arrival times. The weights are constrained to be non-negative since ion counts cannot be negative numbers.

P08

2. ALGORITHM

The B-spline of order m is composed of

$$b_m[k] = \frac{1}{2}(b_{m-1}[k] + b_{m-1}[k-1]), \left(m = 2,3,4 \ldots \right) \quad (1)$$

which on the basis of the discrete B-spline on the first order

$$b_1[k] = \begin{cases} 1/2 & k=0,1 \\ 0 & \text{otherwise} \end{cases} \quad (2)$$

$$\{b_m[\cdot - j]\}_{j=0}^{N-1}(m = 1,2,3,4,\cdots,M)$$

The set of functions are composed by shifting   (1) and they are referred to as the dictionary.
Then the problem   is to find

$$C_i \geq 0 \quad, \quad j_i \quad \text{and} \quad m_i(i=1,2,\cdots,I) \quad \text{,so that}$$

$$E_2 = \sum_{k=0}^{N-1} \left(P[k] - \sum_{i=1}^{I} c_i b_{m_i}[k - j_i] \right)^2 \quad (3)$$

is minimized for the given profile p[k].
We employ the orthogonal matching pursuit [8] to solve this problem with the nonnegative least squares approximation algorithm [9].
We also have to determine an optimal I somehow because approximation error E_2 is always smaller is larger.
It holds good that

$$\sum_{k=-\infty}^{\infty} c_i b_{m_i}[k - j_i] = \sum_{i=1}^{I} c_i \quad (4)$$

because $b_{m_i}[k] \geq 0$, $c_i \geq 0$ and $\sum_{k=-\infty}^{\infty} b_{m_i}[k] = 1$.

In addition, (4) becomes constant :

$$\sum_{i=1}^{I} c_i \doteqdot \sum_{k=0}^{N-1} p[k] = constant \quad (5)$$

when E_2 is small enough Therefore, a criterion for the sparsity of the approximation is evaluated by

$$E_1 = \log \frac{\left(\sum_{i=0}^{I} C_i\right)^2}{\sum_{i=0}^{I} C_i^2} \quad (6)$$

We take I that minimizes $E_1 + E_2$.

3. CONCLUSIONS

This paper developed a fast algorithm of discrete B-splines approximation for the ion-mobility spectrometry. We are yet to verify the performance by applying it to many data.

References

[1] P.W. Purves, R. Guevremont, S. Day, C. W. Pipich and M. S. Maty-jaszczyk, Mass spectrometric characterization of a high-field asymmetricwaveform ion mobility spectrometer, Rev. Sci. Instrum., 69, 4094-4105,1998.

[2] Owlstone Nanotech, Inc. http://www.owlstonenanotech.com/technology/

[3] ATONARP, Inc. http://www.atonarp.com/en/

[4] M. Unser, Splines: A perfect fit for signal and image processing, IEEE   Signal process. Magazine, 16(6), 22–38,1999.

[5] K. Ichige and M. Kamada, An approximation for discrete B-splines intime domain, IEEE Signal Process. Lett., 4, 82–84, 1997.

[6] *T. Saramaki, Y. Neuvo and S. K. Mitra, Design of computationally efficient interpolated FIR filters, IEEE Trans. Circuits & Syst., 35(1),70– 88, 1988.*

[7] .K. Ichige, M. Kamada and R. Ishii, A simple scheme of decomposing and reconstructing continuous-time signals by B-splines, IEICE Trans.Fundamentals, E81-A, 2391–2399, 1998.

[8] Y. Pati, R. Rezaiifar, P. Krishnaprasad, in Asilomar Conf. Recursive function approximation with application to wavelet decomposition", on Signals, Systems and Comput., 1993

[9] C.L.Lawson and R.J.Hanson,solvingLeast Squares Problems, SIAM, 1987.

P09

Study on Grinding Characteristics of Grinding Wheel Containing Conductive Rubber Balls
Application to Grinding Mold Materials

○Shimon HAGIWARA*,Nobuhide ITOH*, Takashi MATSUZAWA**, Hitoshi OHMORI***, Teruko KATO***, Hiroshi KASUGA***, Takeshi YOSHIMIYA****, Yuji HASEGAWA*****, Naoki MAEBAYASHI*
*Ibaraki University, **Ikegami Mold Co.,Ltd, ***RIKEN(The Institute of Physical and Chemical Research), ****Daiwa Kasei Co., Ltd, *****Ibaraki National Collage of Technology
E-Mail: *13nm431r@hcs.ibaraki.ac.jp, *itoh@mx.ibaraki.ac.jp

Keywords: ELID, Electro-Conductive rubber bonded wheel, Composite bond grinding wheel, Electrolytic dressing

1. Introduction

In recent years, advanced technological innovation in the areas of telecommunications, optics, and electronics has led to the emergence of high performance, highly functional, and lightweight products. In addition to sophisticated functions, added values such as aesthetic qualities are also sought, which requires the further improvement in the precision of the various optical parts making up these products. Generally, the finishing of such parts is often carried out by hand using loose abrasives. However, various problems are faced in this aspect such as lack of experienced technicians. To respond to such social needs, the authors have been developing ELID grinding techniques applying conductive rubber-bonded grinding wheels [1]. Results of investigations to date have confirmed that ELID grinding using conductive rubber-bonded grinding wheels improves ground surface roughness compared to the commonly used cast iron-bonded grinding wheel and metal resin-bonded grinding wheel. Effects of ELID for maintaining grinding performance seen in other grinding wheels have also been confirmed. However, conductive rubber-bonded grinding wheels have drawbacks such as poorer electrolytic dressing characteristics and stability during grinding compared to generally used ELID grinding wheels. In the aim to resolve these problems and put the conductive rubber-bonded grinding wheel to practical application, we are currently developing a grinding wheel containing conductive rubber balls. This report reviews the application of the developed grinding wheel to mold materials, and reports the results of investigations conducted on this.

2. Development of grinding wheel containing conductive rubber balls

The metal resin-bonded grinding wheel containing conductive rubber balls is a grinding wheel containing 0.5 to 1 mm conductive rubber balls filled with WA♯1200 abrasives, which are held together using metal resin bond. This grinding wheel is able to improve the ground surface roughness, which is a characteristic of rubber bond, and at the same time maintain the removal performance by ELID of the metal resin bond, in the aim to realize stable high quality ground surfaces. Figure 2 shows the external view of the developed conductive rubber ball and the surface composition. [2] It can be seen that the ball contains WA abrasives. Figure 3 shows the external view of the metal resin-bonded grinding wheel containing the conductive rubber balls. Observation of the composition confirmed that rubber ball grinding wheel and the metal resin bond (metal 7: resin 3) are adhered closely to each other. In this study, copper was used as the metal.

3. Experimental Method

In the experiments, an ELID rotary suraface grinder and the FUJI ELIDER 910 power supply were used. The grinding wheels employed were WA1200 metal resin-bonded grinding wheel and metal resin-bonded grinding wheel containing WA1200 conductive rubber balls (conductive rubber ball content rate of 20%，40%，55%）to investigate the effects of the conductive rubber balls and the content rate on the finish of the workpieces. Cup-shape grinding wheels with a diameter of φ143×width t3.5 were used. To determine the grinding characteristics for mold materials, SUS420J2 was used as the workpiece. The grinding conditions and ELID conditions set in grinding experiments were work axis rotational speed 300min-1, grinding wheel axis rotational speed 2000min-1, feed rate 1µm/min, depth of cut 20µm, non-load voltage 60V，peak current 5A，and pulse 0n/0ff 2/2µs. The experiments were carried out by first truing the grinding wheel used, then initial electrolytical dressing, followed by the investigation of the grinding characteristics. The grinding characteristics reviewed were changes in spindle load during grinding, surface roughness of the workpiece, and three-dimensional surface properties.
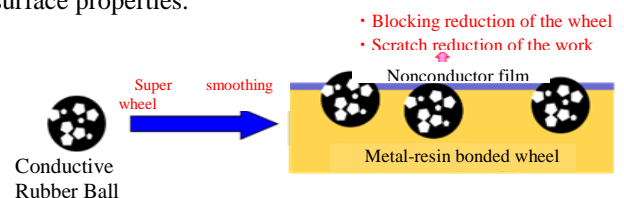

Fig.1 Image of the grinding in the grinding wheel containing Conductive rubber balls

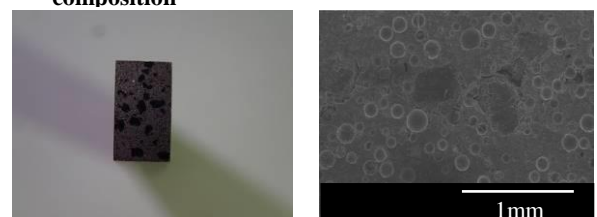**Fig.2 Developed conductive rubber ball and surface composition**

Fig.3 Developed grinding wheel containing Conductive rubber balls and surface composition

P09

4. Experimental Results

4.1. Initial Electrolytical Dressing Characteristics

Figure 4 shows the change in current with time during initial dressing. In all four grinding wheels used in the experiments, the actual current decreased with the elapse of the electrolytical dressing time. This confirms that the metal resin-bonded grinding wheel containing conductive rubber balls can be electrolytically dressed without problems.

4.2. Grinding Axial Load

Figure 5 shows the changes in the axial load during grinding. Although slight changes in the axial load were seen, it did not rise in all the grinding wheels, confirming that stable grinding is realized.

4.3. Grinding Characteristics of Mold Material

Figure 6 shows the results of measuring the surface roughness of the workpieces. It can be seen that when the surface roughness improves when the content rate of the conductive rubber balls is above 40%. With metal resin bonded grinding wheel containing conductive rubber balls, the metal part is etched by the dressing, causing the rubber bond to protrude out. In grinding wheels with rubber ball content rate of 20%, the low abrasive rate is thought to aggravate the surface roughness due to the bond material. Figure 7 shows the three-dimensional surface properties of the workpieces ground using the four grinding wheels. It can be seen that metal resin-bonded grinding wheels, containing 40%, 55% rubber balls produce smoother surfaces than normal metal resin-bonded grinding wheels. Figure 8 shows the surfaces of the workpieces after grinding.
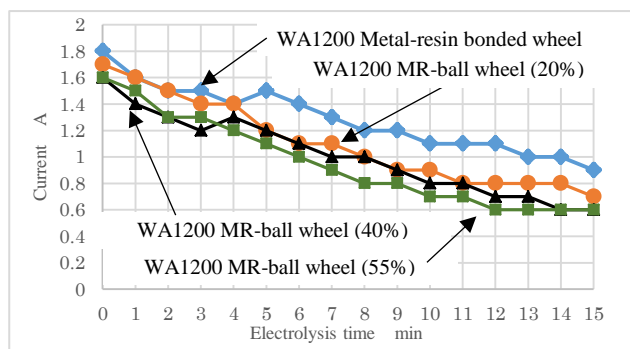

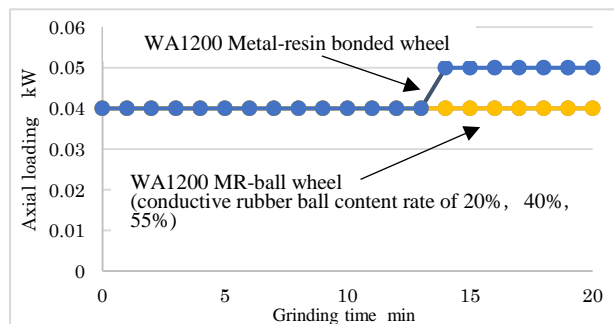
Fig.4 Change of the current in the initial electrolysis

Fig.5 Change in axial loading dug grinding

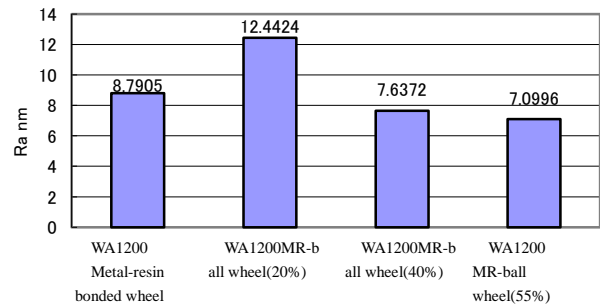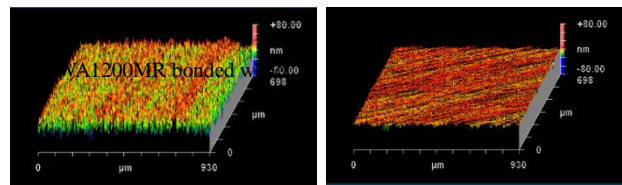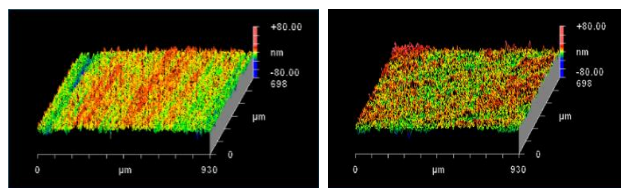**Fig.6 Effect of bonded material on surface roughness**

(b)WA1200 MR-ball wheel (20%)

(c)WA1200 MR-ball wheel (40%)   (d) WA1200 MR-ball wheel (55%)

Fig.7 Obtained surface roughness of SUS420J2

(a)WA1200
Metal-resin
bonded wheel

(b)WA1200
MR-ball wheel
(40%)

(c)WA1200
MR-ball
wheel

Fig.8 Photograph of work piece after grinding with Metal-resin bonded wheel and MR-ball wheel

5. Conclusion

A study was conducted on the grinding characteristics of a grinding wheel containing conductive rubber balls for mold materials, and the following results were obtained.

1) Metal-resin bonded grinding wheels containing conductive rubber balls could be electrolytically dressed without any problems.

2）Grinding wheels containing conductive rubber balls were able to stably grinding mold materials without increase in the axial load.

3) Better ground surfaces were obtained when ground with the grinding wheel containing conductive rubber balls compared to the metal-resin bonded grinding wheel..

References

[1]. Tsukakoshi, Itoh, Ohmori et al.(2008).”Development of Conductive Rubber-Bond Grinding Wheel for ELID Grinding and Grinding Characteristics-Report 2:ELID Mechanism of Conductive Rubber-Bond Grinding Wheel” Journal of the Japan society for Abrasive Technology, pp339-342.

[2]. Hagiwara, Itoh Ohmori et al.(2013). "Characteristic Investigation of Conductive Rubber Ball Containing Metal-Resin bonded wheel" Proceedings of the Japan society for Precision Engineering.

P10

A REFUGEE PREDICTION ABOUT UNIVERSITY AT THE CATASTROPHES ON THE BASIS OF THE ACTUAL REFUGE SITUATION ON THE EAST JAPAN GREAT EARTHQUAKE
-A CASE STUDY OF THE IBARAKI UNIVERSITY-

○Jing NING*, Toshiaki KIN **
* Major of Information and Systems Sciences, Ibaraki University
(4-12-1, Nakanarusawa, Hitachi, 316-8511, Japan),
** Department of Urban and Civil Engineering, Ibaraki University
(4-12-1, Nakanarusawa, Hitachi, 316-8511, Japan),
E-Mail: *12nd309n@vc.ibaraki.ac.jp, ** tkin@mx.ibaraki.ac.jp

1. Introduction

At 14:46 JST(Japan Standard Time)on Friday, 11 March 2011, a magnitude 9.0 (M_w) undersea mega thrust earthquake hit Japan and devastated northeastern region of the country, which is called the Great East Japan Earthquake. It is the worst disaster in the recorded history of Japan, causing 15,560 people dead, 5689 people injured, and 5329 people missing (as of July 13,according to the National Police of Agency) due to the quake and resultant tsunami [1].

In the Hitachi district, earthquake registered an intensity of 6 more on the Japanese scale, also the most powerful earthquake in this area. Electricity, gas and water were disconnected in many days. Roads, railways, airports, and other infrastructure were also severely damaged. In the first three days from 11 March to 13th March, over 13,000 people toke shelter in the 69 evacuation shelters every day. And there was a big lack of food, water, blanket and gasoline in those days.

2. Background of Study

Fortunately, the dead were not reported in Hitachi, but there were a lot of problems constantly arose such as stockpile shortage, dearth of information, confusion and environment deterioration in the shelters, etc. Such a catastrophic disaster was not consider to occur and it was not fully prepared to give the citizens a fair and sufficient support and protect them from a catastrophic disaster.[1]

The College of Engineering, Ibaraki University, which is a large-sized public educational establishment in Hitachi, has many students in the school when the earthquake occurred. Many of them could not back home or stay at home safely. Immediately after the earthquake, they went to the nearby shelter to take a short-term refuge. But actually, some of them could not get food to eat or get clothing to protect against the cold, even some of them were refused by being crowed. On the other hand, there was no maintenance of food and refuge space provided for students on the university side, and it can be said that the measure against refuge was insufficient.

3. Purpose of the study

A lot of problems about the refuge life and the measure against refuge were arisen on this earthquake. Then, in order to build a safe city to against catastrophic disasters, it is considered to be an important subject to take in the measure against refuge by grasping the refuge situation of the earthquake correctly and predicting the numbers of refugee and requirements for reserve.

In this research, situation in the College of Engineering of Ibaraki University in Hitachi was focused, where the reality of evacuation life about the students was tried to be grasped. The purpose of this study was to predict the numbers of refugee and requirements for reserve and provide scientific data for help to find the way to deal with the evacuation in university.

4. Investigation

In order to grasp the reality of evacuation life about the students, we pay attention to the three days from March 11 to the 13th immediately after the earthquake, when the lifeline could not be used at all.

Table. 1. The investigation to the college of Engineering, Ibaraki University.

Object of investigation	1901 students who were on the register in the College of Engineering, Ibaraki University, in case of the earthquake disaster
Time of investigation	June, 2011 ---November,2011
Recovery rate	62.2% (1182 votes were collected)
Method of investigation	Hearing investigation &Questionnaire (Questionnaire votes and the answer sheets for replying are distributed and collected.)
Survey content of investigation	・Individual basic information: (Belonging, sex distinction, means of transportation, resident status, etc.) ・The situation at the time of the earthquake(From the earthquake occurrence to the 13th: The refuge situation, The time and situation about Moving to an evacuation area, etc.) ・Evacuation behavior and refuge consciousness(What kind of place did you take refuge, The reason that you did not take refuge in a shelter, etc.) ・The situation of getting food and drinking water ・Trouble, opinion, proposal, request, etc.

P10

From June to November of 2011, a hearing investigation and a questionnaire research were performed to the students who were on the register of the College of Engineering, Ibaraki University, in case of the Great East Japan Earthquake (Table. 1.).

According the hearing investigation, we knew that there were only a refuge drill and a safety check as the measure against refuge of the College of Engineering, Ibaraki University, before the Great East Japan Earthquake. Maintenance of reserve, such as drinking water and food, or a short-term evacuation area was in the situation which is not carried out.

About the correspondence after the earthquake, a direction from the school side was issued immediately after the earthquake that all the students should evacuate to the ground. And after carrying out the safety check and checking all the members' safety, a going-home direction was issued.

According the questionnaire research, it was shown that 63% of students (741 in 1182 respondents) were in Hitachi at the time of the earthquake occurrence. For the three days (3.11-3.13), 404-447 persons had taken refuge in the house or the parents' home in Hitachi, who have accounted for the biggest rate. There were 180-207 persons who had taken refuge in a friend's house or a relative's house. At the night on March 11, the students who had taken refuge in the city appointed shelter were 93 persons, which was the most within for the three days. Also, there were 9 persons who had taken refuge in the College of Engineering, Ibaraki University.Among the persons who did not take refuge in a shelter, about twenty percent of people had the request to take refuge in a shelter. It can be guessed that refuge in a shelter was stopped owing to the ignorance of an evacuation area, crowded refuge space, and bad refuge environment.

5. Data analysis and Refuge prediction

In order to extract the factor which affected evacuation behavior and refuge consciousness, a simple totaling, cross tabulation analysis, and a chi-squared test were performed in consideration of sex distinction, place of residence, resident status, and means of transportation and so on.

As a consequence, a place of residence (In Hitachi or outside of Hitachi) and resident statuses (living alone or living with family) are considered to be the main factors.

So, in this research, refuge consciousness and evacuation behavior are performed using the method of a part stage focusing on "153 of the students who were living alone in Hitachi and in the campus of the College of Engineering, Ibaraki University at the time of the earthquake occurrence (Table. 2.) " . It is divided into three steps, "Group A", " Group B ", and " Group C",

As a result of analyzing the refuge actual condition, 18% of the students who were in the campus of the College of Engineering, Ibaraki University at the time of the earthquake occurrence had taken refuge in the shelter. When the students with the hope to take refuge in a shelter and the students refused by the shelter were taken into consideration, the students' short-term refugee rate will become to 31% -47%. It is divided into three steps, "Level1", "Level2", and "Level3", and the refugee rate by refuge request is displayed in Table. 3.

Table. 2. The view and result of refugee rate calculation by a part stage.

Refuge request / Evacuation area	no shelter refuge request	weak shelter refuge request	strong shelter refuge request
In the house or the parents' home	○		
In the car		Group C: 16%	Group B: 13%
In a friend's house or a relative's house	○		
In the city appointed shelter or the College of Engineering, Ibaraki University	Group A: 18%		

Table. 3. Calculation of each refugee rate of a part stage.

Level	Refugee	Rate
Level 1	Group A	18%
Level 2	Group A + Group B	18%＋13%＝31%
Level 3	Group A + Group B + Group C	18%＋13%＋16%＝47%

Maintenance of a stockpile is also divided into three steps: "basic maintenance", "strengthening maintenance", and "full maintenance" (Fig.1.).

Maintenance for corresponding to "Level1" was considered as "basic maintenance", maintenance for corresponding to "Level2"" was considered as "strengthening maintenance", and maintenance for corresponding to "Level3" was considered as "full maintenance."
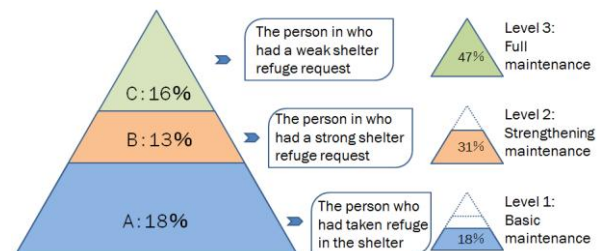

Fig. 1. Refugee prediction and maintenance prediction (three steps) .

6. Result

It showed that about 18-47% members need refuge for a three-day short-term. It means that 560～1460 of 3100 students in the College of Engineering, Ibaraki University need reserve for about three days, and requirements for reserve were about 1120～2920 people per day.

Using this result, several proposals can be suggested for the evacuation related to university and cooperation with the local community.

References

[1]. Hitachi. (2011.9). " Hitachi earthquake disaster recovery program~ relief and vitality to the future.", pp. 2,pp 19.
[2]. Hitachi formal homepage(2014.8):
http://www.city.hitachi.ibaraki.jp/index.html

Visualization of hydrogen in electrolytically charged cold-rolled austenitic stainless steels

○Yukimasa Ichimura*, Goroh Itoh**

Graduate Student, Graduate school of Science and Enginnering, Ibaraki University,
***Department of Mechanical Engineering, Ibaraki University**
E-Mail: *14nm410x@vc.ibaraki.ac.jp, **gitoh@mx.ibaraki.ac.jp

Keywords: stainless steel, hydrogen microprint technique, stress, hydrogen embrittlement, cathodic electrolytic charging, hydrogen diffusion, hydrogen invasion, hydrogen emission,

1. Introduction

In recently years, environmental problems such as global warming and exhaustion of fossil and air pollution have been growing into serious problems. This is caused by the fact that energy sources depended on fossil fuel such as the gasoline. Therefore, an energy source to become the substitute is necessary, and using hydrogen as clean energy has been paid attention to. And, the chance of metallic material such as stainless steels is used in hydrogen environment increase.

However, hydrogen energy using have a problem called the hydrogen embrittlement. Hydrogen embrittlement is a phenomenon to reduce strength and ductility because hydrogen invades it in materials. The materials used for a hydrogen-related apparatus for this phenomenon are limited. A6061 and sus316L with superior hydrogen properties-resistant are domestic safety levels, and use is accepted now. Of these, in SUS316L, the use in more extreme strong processing materials is hoped for the purpose of the light weighting of the apparatus and spacing-saving, reduction of the cost. However, as for the hydrogen behavior of processing materials, a lot of any questions do not yet lead to elucidation. Therefore a solution of the SUS316L steel performed hydrogen micro print technique (HMPT) and Thermal Desorption Spectrometry (TDS) about solution-treated materials and cold-rolled by 60% materials in this study and investigated visualization of the-releasing behavior of hydrogen and the hydrogen quantity in materials.

2. Specimens and Procedure
2-1. Cathodic electrolytic charging

Cathode places the specimen and anode places the platinum. The chemical reaction of each side was shown expression(1).

Anode(+) : $4OH^- \rightarrow 2H_2O + O_2 + 4e^-$

Cathode(-) : $4H^+ + 4e^- \rightarrow 2H_2$ (1)
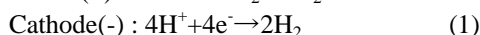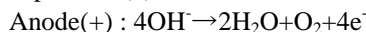
However, many of occurring atomic hydrogen causes the recombination reaction, and do not invade into a specimen. Then, by adding NH_4SCN called hydrogen recombination poison to an electrolysis solution, a recombination reaction can be inhibited and hydrogen invasion can be promoted remarkably.
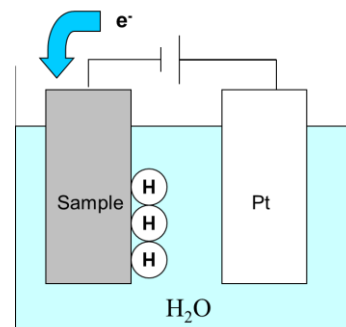

Fig.1   Schematic for cathodic electrolytic charging

2-2. Principle of HMPT

The principle of HMPT is schematically shown in Fig. 2. In HMPT, a hydrogen atom evolved at the specimen surface is visualized as a silver particle using photographic emulsion layer containing silver bromide. Following the oxidation-reduction reaction indicated in Eq. 2, the metallic silver atom will be produced by a strong reduction power of the hydrogen atom at the site where the hydrogen atom is emitted.

$Ag^+ + H \rightarrow Ag + H^+$ (2)
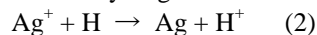
The silver bromide particles that have not been reacted with hydrogen will dissolve out into the fixer, and finally only the metallic silver particles will remain on the specimen surface in gelatin film of the emulsion. Hence, it is possible to visualize the emission site of hydrogen.
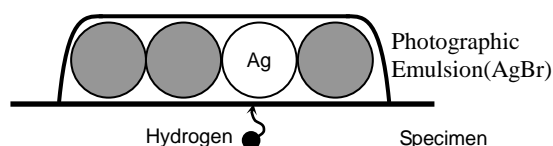

Fig. 2 Schematic drawing showing the principle of the hydrogen microprint technique (HMPT)

2-3. Specimens

Specimen used in this study is SUS316L. Table 1 shows their chemical composition. The specimen was cold-rolled by 60% into 0.2mm, and a part of specimen was solution-treated at 1050 °C for 1 hour. One side of the specimen surface was polished using #400 paper and electropolished to mirror-like finish.

Mirror like surface was electrolytic-etched in 10 mass% $H_2C_2O_4$ solution. Fig.3 shows their optical micrographs.

Table. 1 Compositions of the specimens in mass%.

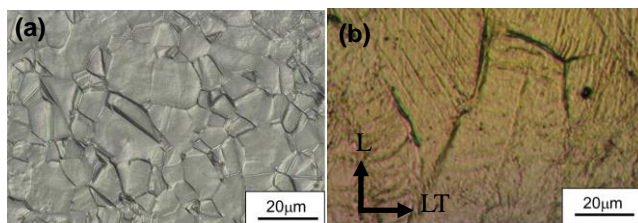| Specimen	C	Si	Mn	Cr	Ni	Mo	Cu	Nb	N	Fe
SUS316L	0.009	0.51	0.83	17.4	12.1	2.0	0.2	0.022	0.011	Bal.

P11

Fig. 3 Optical micrographs of the SUS316L
(a) solution-treated and (b) cold-rolled by 60%

2-3. Experimental Procedures

In this study, two kinds of specimens were prepared. One of specimens was cold- rolled by 60%, the other was solution-treated. Hydrogen was charged cathodically for mirror side of specimens in 0.1 mass% NH_4SCN solution (ph=2.5) consisting of H_2SO_4 at a current density of $0.01 A/cm^2$ for 3 hour from the backside of the one surface covered with the protective film. The protective film was removed and, specimens surface were covered with collodion. After this process, the specimen surfaces were covered with a photographic emulsion (Ilford L-4, diluted by pure water, 4 times) composed of gelatin and silver bromide crystals using a wire loop method. The emulsion layer was dried and at 24hour in the dark room and hydrogen was made to emit. Then, the specimens were dipped into formalin (35 mass% HCHO water solution) for 5 seconds to harden the gelatin layer, and immersed in a fixing solution (15 mass% $Na_2S_2O_3$ water solution) for 8 minutes to remove the remaining silver bromide particles that had not reacted with hydrogen. The specimens were washed with water for 15 minutes. Arrangement of the silver particles was observed with a scanning electron microscope (SEM) equipped with energy dispersive X-ray spectrometer (EDXS). The amount of hydrogen contained in the specimen after hydrogen charging was also measured by the thermal deposition Spectrometry (TDS) using gas chromatography with a heating rate of 10^oC min^{-1} until the temperature reached 600^oC.

3. Results and Discussion

HMPT/SEM images of the hydrogen-charged specimens solution-treated and cold-rolled by 60% were shown Fig. 3. A particle of the white was confirmed in solution-treated, both SEM images of cold-rolled. The white particles observed were identified as silver by an EDXS analysis. From this, it is thought that AgBr particle included in photographic emulsion became the silver particle by released hydrogen. In addition, a silver particle was confirmed in the solution-treated mainly on a grain boundary. On the other hand, a silver particle was confirmed in the cold-rolled from the processing structure. As a result of TDS was shown Table 2. As for the quantity of hydrogen, the charged solution-treated became big in order of the uncharged one, charged cold-rolled and the uncharged cold-rolled solution. In addition, the peak of the hydrogen release boiled around 200 ^{o}C with both specimens. When it compares the result between the uncharged specimens, it is confirmed solution-treated specimens that there is more quantity of immanence hydrogen cold-rolled specimens. In addition, solution-treated was 0.4molppm in 0.2molppm, rolling

specimens in cold-rolled specimens, and, as for the difference of the hydrogen total release quantity per unit of each uncharged specimens and charged one mass to 100°C to 600°C, as for the hydrogenation quantity by the cathodically charging, cold-rolled specimens were bigger. It is thought that increase of the transposition density by the processing increased a trap site of hydrogen as for this. Again a solution-treated in comparison with immanence hydrogen of the cold-rolled. It is thought that there was little influence on materials by the cathodically charging because the quantity of hydrogen charged cold-rolled was remarkably small, and it is thought that hydrogen was added in only materials surface around without being scattered enough by the specimens inside. Thus, it is thought that a position of a silver particle observed in Fig.1 is a trap site at the specimen surface or a-releasing course of hydrogen which scattered specimen surface around. Because hydrogen immanence quantity of the cold-rolled specimens grew big the solution-treated one than hydrogen added in processing materials by a cathode charge by this experiment, it is thought that it is necessary to perform HMPT in uncharged specimens of each sample in future.
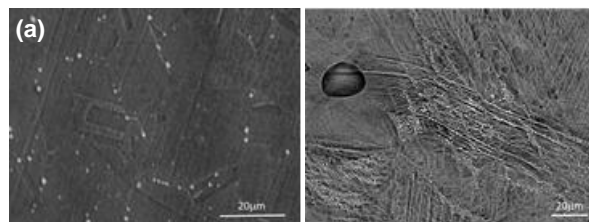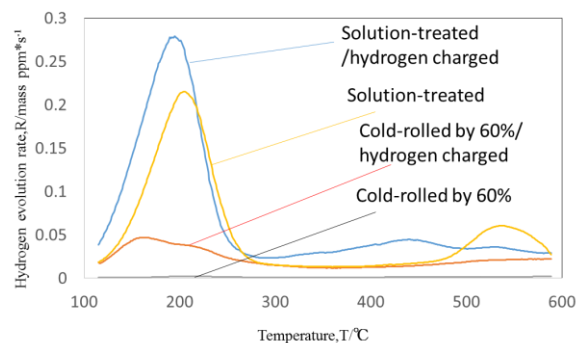

Fig.3 Fig.1 HMPT/SEM images of the hydrogen-charged SUS316L (a)solution-treated (b)cold-rolled by 60%

Table. 3 Hydrogen desorption profiles

4. Conclusion

Release of hydrogen was confirmed solution-treated and cold-rolled specimens. The old-rolled specimens had more immanence quantity of water than solution-treated, but the quantity of hydrogenation by the cathodically charged had a bigger cold-rolled specimens. In the hydrogen charged for 3 hours, hydrogen to the specimens inside cannot spread enough. The release of hydrogen was confirmed on processing structure in cold-rolled on a grain boundary in solution-treated.

P12

Development of ELID grinding wheel by PELID and 3D-printer

○Daiki Yamamoto*, Nobuhide Itoh*, Nozomu Yamada*, Hitoshi Ohmori**, Teruko Kato**, Shinjiro Umezu***,
Takashi Matuzawa****, Akihiko Nemoto*****, Yuji Hasegawa******,
*Ibaraki University, ** RIKEN, *** Waseda University, **** Ikegami Mold Engineering Co.Ltd,
***** Yamagata University, ****** Ibaraki National College of Technology,
E-Mail: * 14nm446f@vc.ibaraki.ac.jp
Keywords: Grinding, Grinding wheel, ELID, PELID

1. Introduction

In recent years, competition in the manufacturing industry is growing increasingly intense every year on a global-scale. For this reason, the reduction of manufacturing costs and shortening of manufacturing time are important challenges to companies. As one solution, the use of 3D printers is being reviewed. The authors are developing a technique for fabricating grinding wheels by combining the use of a 3D printer and liquid droplet ejection technique PELID[1] to cut manufacturing costs and shorten manufacturing time, aiming at an on-demand manufacturing approach which can fabricate only the required grinding wheel at the required time.

This report discusses the fabrication of a grinding wheel for ELID[2] using the hybrid system combining the 3D printer and PELID, and the results of fundamental grinding experiments conducted using the fabricated grinding wheel.

2. Principle
2.1. 3D printer

The 3D printer is a device which can fabricate three-dimensional objects based on 3DCG data created using 3D CAD. In this study, we used the 3D printer based on the fused deposition modeling method. (Fig.1.) shows the principle of the fused deposition modeling method. With this method, a filament-shaped resin is fed into the nozzle, then the resin is heated and melted, and then extruded and laminated to build the three-dimensional objects.

2.2. PELID technology

(Fig.2.) shows the principle of PELID. PELID stands for Patterning with Electrostatically Injected Droplet. By applying pressure to the liquid needle electrode whose nozzle is filled with liquid, liquid droplets are ejected out to the plane electrode by static electricity. As shown in (Fig.3.), the ejection method of the liquid droplets can broadly be divided into three types: Mode I where the droplets accumulate at the nozzle tip and are ejected, Mode II where the droplets are ejected continuously to form a line shape, and Mode III where the droplets are dispersed by static repulsion and sprayed out. The ejection method of the droplets can be varied according to the electrode distance, nozzle diameter, pressure applied, and properties of the liquid. (Fig.4.) shows the line drawn by the suspension of alumina abrasives and ethanol in Mode II, and (Fig.5.) shows the ejection method by spraying in Mode III. By dispersing abrasives in ethanol in this way and ejecting the abrasives by PELID, abrasive dispersion cab be controlled.[3]

2.3. Hybrid system for fabricating grinding wheel using 3D printer and PELID

(Fig.6.) shows the overview of the hybrid system combining a 3D printer and PELID for fabricating grinding wheels. The PELID liquid needle electrode is positioned at the same. Axis as the 3D printer nozzle, and a plane electrode is used for the stage.
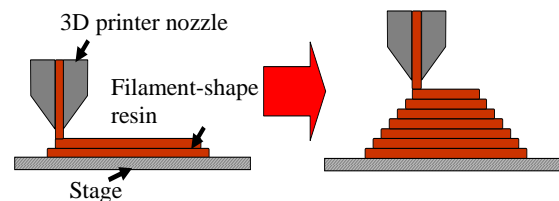

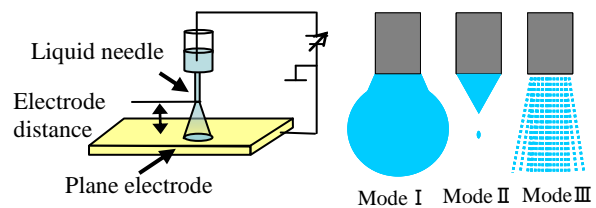**Fig.1. Principle of fused deposition modeling method using 3D printer.**
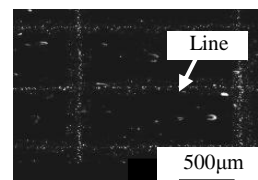

Fig.2. PELID principle.　　**Fig.3. Ejection of liquid droplet**
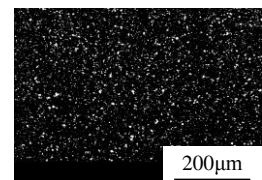

Fig.4. Drawing of line　　**Fig.5. Spray ejection**
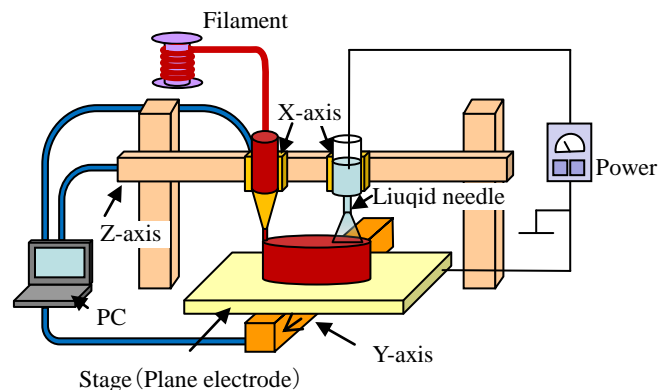**(Mode II)**　　　　　　　**(Mode III)**

Fig.6. Overview of grinding wheel fabrication system

3. Fabrication of grinding wheel using hybrid system

In this experiment, electrically-conductive ABS resin (with resistance of about 3kΩ), which is the bond material of the grinding wheel, was laminated using the 3D printer. Next, a suspension of alumina abrasives (WA#3000) and ethanol was sprayed by PELID to disperse the abrasives while fabricating the grinding wheel. Electrically -conductive ABS resin was used as the electro-conductive material of the 3D printer's filament so that the product made by the 3D printer can serve as an electrode in PELID. Another reason is to enable the product to be ground by ELID. With PELID, alumina abrasives are suspended in ethanol to enable the abrasives to be sprayed. After spraying the ethanol, only the volatilized abrasives can be dispersed. (Table.1.) shows the conditions for fabricating the grinding wheel. (Fig.7.) shows the fabrication state. The fabrication time of the grinding wheel under these conditions is about 40 minutes.

(Fig.8.) shows the external view of the fabricated grinding wheel. The wheel made using the hybrid system is given a metal shaft. The X-X in (Fig.8.) was cut to check the state of the abrasives. (Fig.9.)(a) shows the SEM observation images while (b) shows the distributed state of the abrasives obtained by EDX analysis. It can be confirmed that white alumina abrasives (WA#3000) of about 5µm are held in place between the electrically -conductive ABS resin (black part) of the parent material. The abrasive layer is held in place as if sandwiched by the resin. This demonstrates that grinding wheels can successfully be fabricated using the developed hybrid system.

Table.1. Grinding wheel fabrication conditions

| Grinding wheel	Shape	Axis with cylindrical
	Outer diameter	7mm
	Length	16mm
3D printer	Use material	Electrically -conductive ABS resin
	Laminate thickness	0.1mm
	Lamination width	0.4mm
	Nozzle moving speed	5mm/s
	Nozzle temperature	523K
PELID	Use liquid	Ethanol+WA#3000 (Mass ratio10：1)
	Applied voltage	4.4kV
	Distance between electrodes	40mm
	Inner diameter of the nozzle	0.41mm
	Discharge form	Mode III
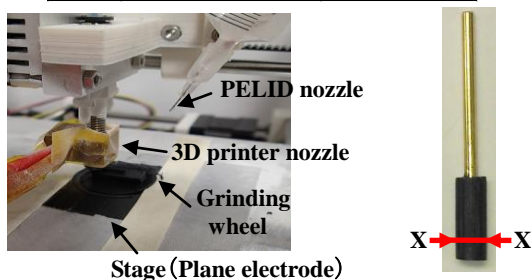
Fig.7. Fabrication of grinding wheel using hybrid system

Fig.8. Appearance of grinding wheel

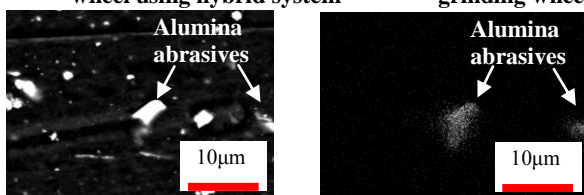
(a) SEM observation images   (b) EDX analysis

Fig.9. Results of observing cross-sectional (X-X) structure

4. Grinding experiments

Using the mounted grinding wheel fabricated using the hybrid system combining the 3D printer and PELID. The work piece used for grinding was the COP resin (ZEONEX) whose surface has been ground with a #400 grinding wheel. (Fig.10.) shows the photo of the hybrid grinding system and the grinding state. (Fig.11.) (a) and (b) show the optical microscope image of the work surface before and after the ion shot dressing. (Fig.12.) shows the surface roughness of the work before and after the dressing. It can be seen in (Fig.11.) that there are large grinding marks before the dressing, which disappear after the dressing. In (Fig.12.), given that the surface roughness has improved after the dressing, this confirms that the mounted grinding wheel made using the hybrid system combining the 3D printer and PELID has good removal capability.
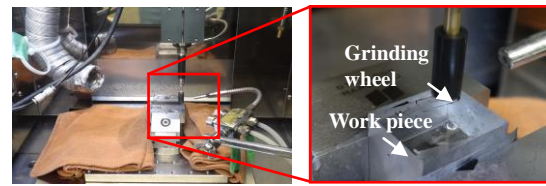

(a) Overview of machining   (b) Enlarged view

Fig.10. Grinding of COP resin
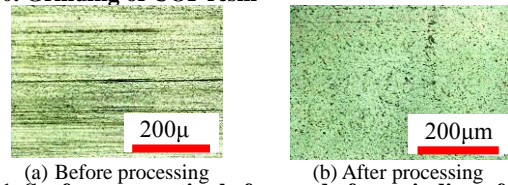

(a) Before processing   (b) After processing

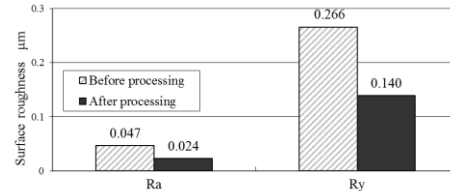**Fig.11. Surface properties before and after grinding of COP resin**

Fig.12. Difference in surface roughness before and after COP resin grinding

5. Conclusion

This report discusses the attempts by the authors to fabricate a hybrid system combining a 3D printer and PELID in the aim to realize on-demand manufacturing, then fabricate a grinding wheel using this system, and conduct grinding experiments using the fabricated grinding wheel. We succeeded in fabricating the grinding wheel by forming the bond material using the 3D printer and scattering the abrasives by PELID. In the grinding experiments using the grinding wheel, improved surface roughness of the workpieces was confirmed. These results demonstrate that the developed system is able to fabricate grinding wheels.

References

[1]. Suzuki, Umezu, Koizumi, and Kawamoto: Injection of Micro Water Droplets in Static Injection Phenomenon , IIPThe Japan Society of Mechanical Engineers Information/Intelligent/Precision Equipment Seminar Proceedings (2004) pp.254-257

[2]. Hitoshi Ohmori: ELID Grinding Technique, Japanese Industrial Standards Committee (2000)ISBN4-7693-2151-1 C3053 pp.139-164

[3]. Watabiki, Itoh, Hasegawa, Umezu, Matsuzawa, and Yamamoto: Efforts in Fabricating Grinding Wheel for ELID Grinding using 3D Printer，The Japan Society for Precision Engineering (2014)Author2, (Date). "Book Title" *Publisher*.

Executive Committee

- **General Chair**

  Anjeza ALAJ   *Graduate School of Science and Engineering*

- **Vice Chairs**

  Jing NING   *Graduate School of Science and Engineering*

  G. Anne NISHA   *Graduate School of Science and Engineering*

- **Members**

  Yoshihiro ITO   *Graduate School of Science and Engineering*

  Liying XIAO   *Graduate School of Science and Engineering*

  Wenzhe LI   *Graduate School of Science and Engineering*

  Tomonori WATANABE   *Graduate School of Science and Engineering*

  Ryodai SUZUKI   *Graduate School of Science and Engineering*

  Kunimitsu TAKAHASHI   *Graduate School of Science and Engineering*

  Kai WANG   *Graduate School of Science and Engineering*

  Atsushi KATO   *Graduate School of Science and Engineering*

  Erjing ZHOU   *Graduate School of Science and Engineering*

  Yuji FUJISHIMA   *Graduate School of Science and Engineering*

  Xuan MA   *Graduate School of Science and Engineering*

  Kosuke KURIHARA   *Graduate School of Science and Engineering*

  Takuya WADA   *Graduate School of Science and Engineering*

  Sachin RAI   *Graduate School of Science and Engineering*

  Thai TRAN VAN   *Graduate School of Science and Engineering*

  Kun HAN   *Collage of Engineering*

- **Advisers**

  Zhishen WU   *Faculty of Engineering*

  Tatsuya NUMAO   *Faculty of Engineering*

  Masaru KAMADA   *Faculty of Engineering*

  Yuji KUWAHARA   *Faculty of Engineering*

  Hideyuki TONOOKA   *Faculty of Engineering*

  Atsushi MINATO   *Faculty of Engineering*

  Makoto TAMURA   *Institute for Global Change Adaptation Science*